SPECTRAL SERIES EMISSION AND ATOMIC POPULATIONS IN SOLAR ASTROPHYSICAL AND LABORATORY FUSION PLASMAS

A THESIS SUBMITTED TO
THE DEPARTMENT OF PHYSICS AND APPLIED PHYSICS
OF THE UNIVERSITY OF STRATHCLYDE
FOR THE DEGREE OF
DOCTOR OF PHILOSOPHY

By
Stuart David Loch
April 2001

Abstract

This thesis seeks to provide spectroscopic diagnostic tools through the advancement of atomic modelling techniques. Issues of opacity (and its consistent treatment from bound to free states), excited state population modelling and spectral feature generation are dealt with. The escape factor technique is used to account for opacity in emergent flux and atomic population calculations. A thorough treatment of low series member opacity is given in the code ADAS 214, which modifies adf04 files for subsequent population processing via ADAS collisional-radiative routines. The escape factor expressions are analytically extended from bound to free states, allowing opacity to be dealt with smoothly across the ionisation threshold. The continuity approach of this thesis is contrasted with the usual technique of introducing an ionising plasma microfield which gradually 'dissolves' the highly excited quantum shells into the continuum. A comprehensive plan is outlined which will allow collisional-radiative modelling of arbitrary heavy species. This scheme works in a new coupling picture, for which new Gaunt factors have been developed. The bundled-$(J_p)nl$ and bundled-$(J_p)n$ block primitives of this model have been developed, as has a test module for a single n-shell of the bundled-$(J_p)nlj$ block primitive. A scheme for automatic determination of bundling cut-offs has also been demonstrated. The new model is designed in a modular manner to allow future developments to be performed in testable steps and to take advantage of modern high performance computers. The population, opacity and continuity modelling are then brought together in the generation of a synthetic spectrum for series limit wavelengths of hydrogenic systems. A specific code is written to allow JET divertor Balmer series limit observations to be analysed, returning diagnostic information on plasma electron density, temperature and recombination state. The code is shown to provide good fits to typical divertor spectra and will be developed into an ADAS spectral fitting procedure. The future directions for application of the work are outlined.

Acknowledgements

I have been fortunate during the course of this thesis to have the help and support of many people. It is with pleasure that I thank my supervisor Prof. Hugh Summers for the enthusiasm, attention to detail, patience and wealth of ideas which he showed at every stage of the PhD. I would also like to thank my joint supervisor from RAL, Dr. Richard Harrison for his support and encouragement. Thanks also to Dr. Nigel Badnell for the advice that he has given and for his valuable help in running Autostructure. I am grateful to Prof. Kurt Behringer for allowing me access to his opacity code and for the help and advice that he gave me during its conversion to ADAS 214. I am indebted to Dr. Jim Lang who ensured that all interactions with RAL ran smoothly and who has taken an interest in this work from the beginning. I would also like to thank Dr. Peter McWhirter for the useful discussions at various stages of this work. Thanks also to the Rutherford Appleton Laboratory for the generous provision of a case award during the course of my studies.

My collegues in the group have also been a source of encouragement throughout the work. I would like to thank Gordon for his friendship, honesty and the many insightful comments that he has made. I am grateful to Dr. Connor Ballance for the use of some of his numerical routines and for allowing me to take out any physics related agression on a squash ball instead of on my computer. Thanks also for introducing me to skiing. Thanks to Kathleen for reading through much of this thesis, any remaining spelling mistakes are my responsibility. Thanks to Dr. Harvey Anderson for all the hard work that he did on ADAS 311 - it made the development of the code in chapter 4 a possibility. I would also like to thanks Dr. Martin O'Mullane for helping me at various stages despite being so busy with his own work. Thanks also to Allan for his friendship and for all the computer advice he has given.

To the folk at tea (David, Gail, Hendy, Gordon, Allan and John), thanks for the laughs and for not giving me a red card. Special thanks to my 'fellow olympians' Marcao, Hendy and Sean. In particular thanks to Hendy for all the games of squash, visits to the weights room and for the new words that you taught me.

To my friends from Church (Jim, David D, Philip, David M, Steve Y, Stephen, Dawn, Steve G, Denise, Les, Kathleen) thanks for all the great times we have had, and for

not asking me to stop talking when I went on about my thesis. Also, thanks to Avril for the all the encouraging emails that she sent and to Karen, Carly, Fiona and Tom for their help over the last few years.

My family have been a source of encouragement and support throughout all my life, not just the last few years for this thesis. So special thanks go to my mother, father and brothers, Fraser and Iain. Thanks also to Larinda and Nathanael for the blessing that they have been. I would like to thank my Uncle David for encouraging me to stay on for the PhD. Thanks are due to my Gran Munro for her faithful support and concern and I am indebted to my Papa Loch for the example of his life and all his words of wisdom.

Contents

List of Figures

List of Tables

Chapter 1

Introduction

1.1 Aims and objectives

This thesis is focused on atomic modelling for diagnostic analysis of plasmas through observation of their spectra. It is recognised that spectroscopy of high temperature plasmas provides probably the most sensitive and revealing type of measurement which can be made on atoms. Such studies are applicable whether the plasma is remote as in astrophysics or nearby in the laboratory. The emitting atoms are in many circumstances revealing of the environment in which they lie and it is these situations which provide the diagnostic opportunities. Consider the solar chromospheric/coronal plasma and the laboratory fusion plasma. They have marked similarities from the point of view of spectral emission, although their energy input mechanisms are quite different. Both are high temperature plasmas with the solar upper atmosphere electron temperature ranging from $\sim 2 \times 10^4 K$ to $\sim 2 \times 10^6 K$ in the quiet sun and up to $\sim 1 \times 10^7 K$ in flares. The modern fusion plasma, such as the Joint European Torus (JET) tokamak, is of somewhat higher temperature at $\sim 3 \times 10^7 K$ to $\sim 2 \times 10^8 K$ ($3keV$ to $20keV$) in the core, but with temperatures in the key divertor plasma very similar to the solar case. The core fusion plasma has electron densities of $\sim 3 \times 10^{13} - 1 \times 10^{14} cm^{-3}$ while the solar coronal plasma is of lower density at $\sim 1 \times 10^8 cm^{-3}$ but rising steadily as one moves down through the chromosphere. Both types of plasma display marked gradients in temperature and density (compare

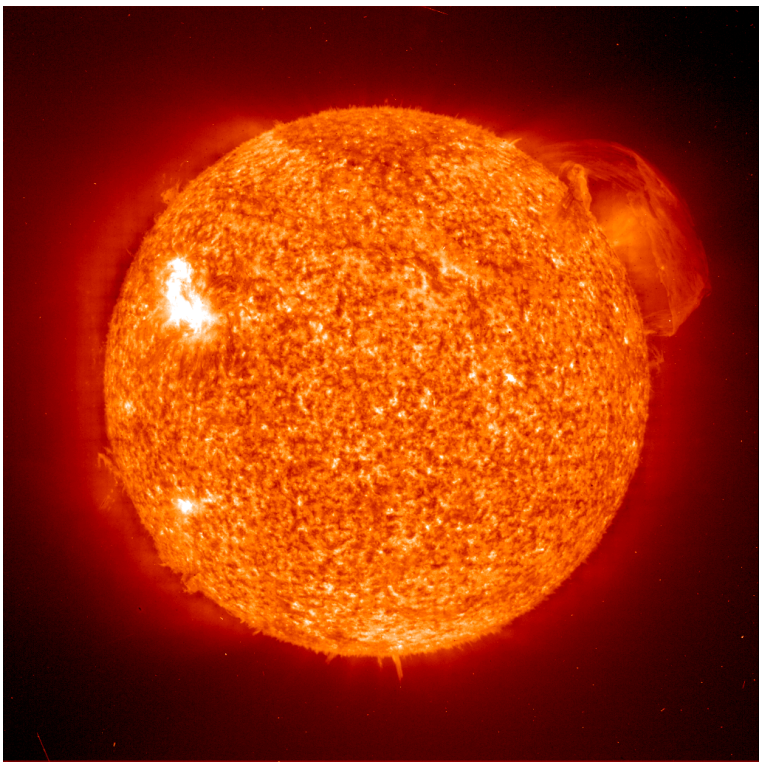

Figure 1.1: He 304 Å observation of the solar chromosphere at $T_e \sim 40,000K$, taken using the EIT instrument onboard the SOHO spacecraft.

the solar transition region and high shear layers and H-mode pedestals in the fusion case) quite apart from local disturbances and instabilities. These temperatures ensure that the plasma is highly ionised and the relatively low densities mean that the ion environment is far from local thermodynamic equilibrium. Also, the dimensions of the plasmas ensure that one has in general easy escape, that is optical thinness, of the emitted radiation. For these reasons, the spectral analysis for these two types of plasma has developed similarly in a modelling picture which even in the fusion case is often called 'coronal'.

With the development of X-ray telescopes and new satellites and spacecraft with scientific payloads (e.g. the Hubble Space Telescope, SOHO, TRACE, CHANDRA) there are few spectral regions left that cannot be measured. This means that the spectra resulting from almost any possible atomic transition can be observed and diagnostic information obtained.

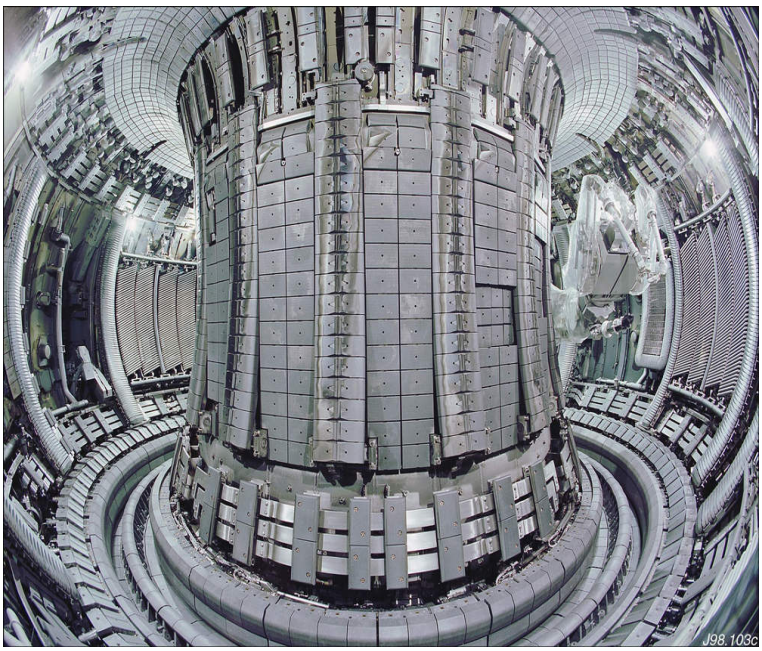

Figure 1.2: An image of the inside of the JET tokamak.

Spectroscopy can be divided into the broad categories of 'wavelength' and 'intensity' based spectroscopy. Wavelength spectroscopy takes wavelength information such as line centroids and line widths and returns information on the local plasma conditions such as flow velocities, ion temperatures and in certain circumstances ion and electron densities. It does this primarily via knowledge of the plasma distribution functions and relates the wavelength information to the appropriate plasma parameters, for example relating the shift in a line centroid to a doppler shift in the emitting atoms. In general it is not necessary to know detailed information on the atomic populations for such techniques. This is mostly, but not always, the case. For example, diagnosing plasma electron densities from observed collisionally broadened line widths requires information on the populations for the line broadening calculations. However, broadly speaking, these techniques are independent of the population distribution within the emitting atoms. The observations of such spectra developed alongside the models which use wavelength spectroscopy for their interpretation.

This thesis focuses largely on using intensity spectroscopy as a means of interpreting observational data. In intensity spectroscopy information such as line heights or line

ratios are used. The height of spectral lines is strongly dependent on the atomic population structure of the emitting atoms, thus models designed as tools for intensity spectroscopy are firmly grounded in atomic population modelling. Again the diagnostic models have tracked the development of observations and the increasing resolution to which spectra can be observed.

Initially it was mainly the strong resonance lines which could be resolved and intensity spectroscopy was used to relate the intensities of such lines to the population structure, which could then be related to the plasma emitter or electron densities and temperatures if information was available on all of the dominant atomic processes which determine the system's population distribution. The resonance lines of interest tended to come from plasmas of the coronal type, and as such could be modelled relatively simply. There were no optical thickness effects and the dominant atomic processes that had to be considered were largely the strong dipole-allowed collisional and spontaneous rates which determined the populations of the principal quantum shells. With the breadth in the wavelength range of spectrometers, observations could be made of most regions of interest and so most of the main resonance lines could be observed. Note that the general method in developing the diagnostic technique was to construct the atomic model, with all the appropriate transition rates, to then follow this through to a synthetic spectrum, or at least a theoretical intensity. A synthetic spectrum generated for intensity spectroscopy analysis is referred to as a 'spectral feature'. The optimisation of a fit of this feature to an observed spectrum returns a diagnostic of plasma parameters such as temperature, density, etc.

As plasmas of greater density (or sometimes of greater dimensions in the astrophysical case) were observed, optical thickness effects became significant. For example investigations into solar prominences led to the conclusion not only that they were extremely optical thick in the Lyman series (Hirayama, 1963), but that absorption of the Lyman continuum was one of the main sources for prominence energy gain (Poland and Anzer, 1971). The need to interpret optically thick spectra led to the development of various techniques to deal with opacity adjustments to populations, line shapes and emergent fluxes. These techniques can be broadly categorised into 'radiative transfer' and 'escape factor' methods and will be discussed later in this

chapter, and in chapter 2.

As spectroscopic techniques advanced it became possible to resolve finely split multiplets of known atomic systems. This allowed the redistributive rates between these finely split levels to be examined and atomic models were developed to account for such transition rates. The effects of re-distributive electron and ion collisions were included in the atomic modelling such that non-statistical, resolved populations could be evaluated. These models could then be employed to interpret the intensity of the observed spectral multiplet in terms of the dominant plasma parameters involved in the re-distributive transitions (such as the ion and electron densities). In this way more detailed plasma information than was possible using resonance lines alone could be diagnosed.

As more exotic plasmas were generated on earth and spectral observations of astrophysical objects improved, it became possible to observe the comparatively weak spectral lines originating from high quantum shells. These observed high series lines are often blended with neighbouring members and are typically observed from low temperature, high density plasmas. These spectra were first of all interpreted using wavelength spectroscopy (the wavelength of the last observable discrete line was used to determine the plasma electron density, see Inglis & Teller, 1939). Techniques were then developed such that intensity spectroscopy could be performed on series limit observations (Pigarov et al., 1998). Interpreting these spectra requires knowledge of the atomic processes to and from the high quantum shells, with a need to account properly for the transitions from high series blended lines and the smooth merging of such high n-shell bound populations through to free states. Account must also be taken of plasma microfield effects on the high lying populations and associated transitions consistently within the collisional-radiative framework. Such models can reap a further level of diagnostic information than was possible from resonance line or multiplet analysis alone. The work of this thesis is part of the development of this latest spectroscopic technique and seeks to match absolute intensities of high series observations with a fitted theoretical spectrum. Again the basic principle has been used where the construction of an atomic model leads to a predicted spectrum, allowing a fitting of this synthetic feature to the observations to be made and plasma

parameters diagnosed.

The next observational stage in fusion tokamaks is to look at the spectra produced by heavy species introduced to the plasma. This is as a result of the plans to layer heavy species into certain wall-tiles of the ITER reactor. There is a dual purpose in this, firstly these heavy species are more temperature resistant that the carbon based tiles that are used in existing reactors. Secondly these heavy species layers will provide a means of detecting how eroded the walls are at any point. The idea is that when the fusion plasma exposes the heavy species layers, they will be ejected into the reactor. These species will then emit characteristic spectra which will be used to alert the operators of the device to the progress of the wall erosion. Light species could not be used for this because they would be fully ionised in the core and would emit no spectral lines. In the build up to the ITER reactor there will be preparatory observations of heavy species high series limits as well as the extremely detailed grass-like spectra observed from the complex set of energy levels possible in such systems. For meaningful intensity spectroscopy to be performed on these new observations, it is necessary to develop a new atomic model. The later work presented in this thesis seeks to do this. The high series hydrogenic population work developed here can be used to account for the high lying populations in the heavy species and the basic plans are laid out which will allow the lower levels to be dealt with consistently. The basic methodology of intensity spectroscopy is adhered to, that is the atomic model developed will be carried through to a final spectrum which can be compared with observations to return diagnostic information on the heavy species emitters. Both the high series and heavy atom modelling introduce some difficulties which need to be dealt with. However, there is a corresponding return in the certainty and variety of diagnosed plasma parameters using these new models.

There were a variety of physical processes that required attention in this thesis. These included opacity, continuity of rates and populations from bound to free states, obtaining high quality line profiles for transitions near the series limit and dealing with the rate expressions for high quantum shell populations to greater resolution than has been done before. Before proceeding with a description of the basic theory used

throughout this thesis it is worthwhile stopping to overview each of these difficulties that must be overcome, describing in broad terms the physical nature of each problem.

Opacity refers to the process where photons travelling through a plasma do not escape, but are re-absorbed within the plasma volume. This has the dual effect of altering the emergent flux and adjusting the population distribution within the absorbing atoms. Although the emergent flux is usually reduced, it is possible for opacity to increase the flux in a given line if photo-absorptions in another line indirectly increase the population density of the upper level of the transition in question. If the photons escape without re-absorption occurring the plasma is said to be 'optically thin' in that transition. If such re-absorptions do occur it is referred to as being 'optically thick'. Opacity in principle couples every point in the plasma together and we have a non-linear and non-local problem to solve. The main approaches that have been developed to model opacity are 'radiative transfer' and 'escape factor' techniques. The technique of radiative transfer is a heavily computational approach to solving the coupled equations of radiative transfer and statistical balance. It has been used to deal with the effects of opacity on population structure, line profiles and emergent fluxes for various plasmas such as stellar atmospheres (Carlson, 1986) and solar prominences (Gouttebroze et al., 1993). The escape factor approach is a moderate optical depth method where it is appropriate to treat the equation of radiative transfer in a linear approximation. This approach has the advantage that it is easily integrated into other models, and has been used to diagnose optical depths in the solar atmosphere (Doyle & McWhirter, 1980, Brooks et al., 2000), to infer information on the structure of the solar atmosphere (Fischbacher, et al., 2000) and to diagnose plasma densities in fusion divertors (Behringer, 1998). See Irons (1979) for an overview of the basic escape factor expressions and derivations.

In this thesis opacity is accounted for using the escape factor approach. As will be seen, the approach is easily integrated into collisional-radiative models and emergent flux calculations. Escape factors are usually applied to discrete, low series member spectral lines (though not always, see Drawin (1970) for an example of escape factors used to account for continuum opacity). This thesis extends this low level approach

to model opacity through high series members into the continuum. We show that the effects of opacity continue smoothly from bound to free states in a similar manner to Gaunt factors and Saha-Boltzmann deviation factors (b-factors). This allows the usual low series member escape factor techniques to be extended to smoothly account for opacity in high series members through to the continuum.

In order to correctly predict the high series spectrum we also need to accurately model all the possible transition rates that can influence the high quantum shell populations. That is, one must account for all the possible transition rates (i.e. spontaneous, stimulated and collisional rates) that have an influence on the high lying atomic states. The modelling of atomic population distributions has a long history and is now at an advanced stage. The most successful technique in dealing with population distributions has been that of collisional-radiative theory (Bates et al., 1962) (see section 1.2.6 for a more complete description of the collisional-radiative approach). In this thesis the advancements to existing collisional-radiative models are performed within the framework of the Atomic Data and Analysis Structure (ADAS) suite of computer codes (Summers, 2001). ADAS consists of an interconnected set of computer codes and atomic data. The data represents the highest quality available, covering most types of data needed for existing astrophysical and fusion calculations. Standard ADAS data formats (referred to as 'adf' datafiles) are designed such that the codes are general purpose and applicable to a wide range of atomic and ionic systems. The codes are split into eight series with each series consisting of a set of codes. For example, series three contains the codes for charge exchange modelling. ADAS 311 then represents code eleven of series three. The codes are used to model the radiative properties for wide range of plasma conditions. The routines are designed such that they can solve for the populations in a number of 'pictures', whether in a b-factor, b-factor with exponential term included or c-factor form. This eliminates likely numerical inaccuracies and the computational techniques have been proven to be both stable and fast. The codes are also able to interpret spectral measurements and, within the series six set of codes, to generate synthetic spectra (referred to as 'special features'). We find it convenient to define a heirarchy of spectral features closely linked to population structure. If a set of lines in the special feature are

connected via pure branching line ratios they are referred to as 'feature primitives'; if the connection is via excited level population balance they are called 'features'; if the connection is via ionisation balance they are called 'superfeatures'. It is shown later how similar heirarchical ideas (section 4.1.1) in population structure lead to coherent organisation of complex atom modelling.

The ADAS codes are accessed through an IDL graphical user interface. This allows the user to specify which atomic system is to be investigated, what atomic data to use, what plasma parameters the code has to be run for and what format the output data and graphs are to be given in. This allows the user to immediately see the results of the calculation, making it possible to explore the parameter space for the given system. If there is no atomic data present for a given calculation it is possible to generate the necessary data (often to a lower quality) using various ADAS routines. For example ADAS 701 runs the autostructure code (Badnell, 1986), developed from the superstructure code (Eissner et al., 1974); ADAS 801 runs the Cowan structure code (Cowan, 1981) tailored to produce files of ADAS data format by O'Mullane; ADAS 211 generates radiative recombination data using the Gaunt factors developed in (Burgess & Summers, 1987). ADAS also contains a library of key subroutines that can be called from the user's own codes to assist in specific calculations.

This thesis contains a complete description of a model in progress that will form part of the ADAS suite of codes. This model will accurately predict the population structure of arbitrary heavy species and can be run in its present state to model high level hydrogenic populations. A module of this code is used to predict the high quantum shell populations needed for the spectral feature work of chapter 5.

The other main issue addressed in this thesis is the accurate modelling of high series line profiles. Historically, line profiles have been used to provide a wide range of plasma diagnostic information. Any broadened spectral line contains information on the physical process that contributed to the broadening. For example, doppler half-widths can be used to diagnose a plasma ion temperature and profile shapes can be used to infer the nature of the collisional broadening that produced the lineshape (i.e. whether electron or ion broadening dominates). The calculation of line profiles, in particular collisionally broadened line profiles, is a non-trivial problem with many

physical processes potentially contributing to the broadening of such lines. The situation is further complicated for high series lines due to the relatively small amount of high series observational data upon which to test the line profile calculations. Nevertheless, high quality line profile codes such as the PPP code (Talin et al., 1995), have been developed and have proven themselves to be reliable and valid for a wide range of plasma conditions.

Once all of these issues have been dealt with it is possible to combine the high series line profiles which continue smoothly through to continuum wavelengths with high level population results to generate a complete synthetic spectral feature at series limit wavelengths for a wide range of plasma conditions.

The rest of this chapter consists of a brief step back from this final picture and reviews the history of our approach to considering high series spectral prediction. It is hoped that this will provide a useful overview of all the physical effects and theoretical issues that have to be accounted for as well as showing the observations that led to the construction of the final model. Thus the next section provides some of the background theory that will be required, some of the theory is then developed in section 1.3 in the context of various spectral obsevations, from solar through to fusion plasmas.

Chapter 2 then goes into detail on the discrete low series spectral line opacity theory and the code known as ADAS 214 that is used to evaluate opacity modifications to both the emergent flux and atomic population structure of optically thick plasmas. Chapter 3 describes the extension of this theory to high series and continuum frequencies. Chapter 4 goes into the details of the high n-shell population model and our future plans for this collisional-radiative work. Chapter 5 then brings this all together and demonstrates the generation of an arbitrary high series spectral feature. Finally chapter 6 summarises our main conclusions and outlines the future direction of this work.

1.2 Background theory

1.2.1 Escape factor basic definitions

It is first useful to introduce some basic theory which can then be used as the building blocks for the developments presented in later chapters. The terminology of Fischbacher et al. (2000), and the notation of Irons (1979) are used throughout this thesis. Thus the following definitions hold:

- Transmission factor [T] - The average probability that a photon within the line profile will propagate from one given point to another.
- Escape Probability [Θ] - Defined identically to the transmission factor except that the second point lies outside the plasma. That is, Θ is the average probability of a photon emitted within the line profile escaping from the plasma along a particular line of sight.
- Escape Factor - The mean probability that a line photon emitted somewhere in the plasma will escape from the plasma along any line of sight. The phrase 'escape factor technique' is also used in this thesis to describe the general technique of linearising the equation of radiative transfer for the evaluation of the expressions defined here.
- Absorption factor [Λ] - one minus the probability that a net absorption of a photon will occur at a particular point in a plasma. This is sometimes referred to as the 'Biberman-Holstein coefficient' or 'net radiative bracket'.

Note that the only difference between these definitions and those of Irons is that he defines the escape probability to be the mean probability of a photon emitted at a point in a plasma escaping along any line of sight. This is the same as the escape probability defined as above averaged over solid angle. It is felt that defining the escape probability along one given line of sight is an expression more directly applicable to actual observations.

1.2.2 Escape probability and emergent flux

Considering the observed flux escaping from a plasma then the equation of radiative transfer is used to model the variation of the radiation intensity (I) along a given line of sight, denoted by the points along l.

$$\frac{dI(\nu,l)}{dl} = \varepsilon(\nu,l) - \alpha(\nu,l)I(\nu,l) \tag{1.1}$$

where

- $\varepsilon(\nu,l)$ is the emission coefficient defined as the number of photons emitted at frequency ν per unit time, per unit volume, per unit solid angle at position l.
- $\alpha(\nu,l)$ is the absorption coefficient, defined such that $\alpha(\nu,l)I(\nu,l)$ is the number of photons absorbed at frequency ν per unit time, per unit volume, per unit solid angle at position l.
- $I(\nu,l)$ is the intensity of the radiation field at the point of interest (l), defined as the number of photons crossing a unit area, per unit time, per unit solid angle, per unit frequency.

Also define the optical depth (τ) of the plasma to be the absorption coefficient integrated along the line of sight. Thus the optical depth is given by the following expression, with the simplified result for a constant absorption coefficient also shown.

$$\begin{aligned} \tau(\nu) &= \int_0^b \alpha(\nu,l)dl \\ &= \alpha(\nu)b \end{aligned} \tag{1.2}$$

This gives an indication of how far one can 'see' into the plasma. It should be noted that equation (1.1) is non-linear because the emission coefficient (ε) at point l depends upon the upper level population density of the transition in question. This in turn depends upon the number of photo-absorptions that can excite an electron into this level, which depends upon the radiation field I at point l, thus making ε in principle a function of I and thus equation (1.1) non-linear. Note that the emission coefficient

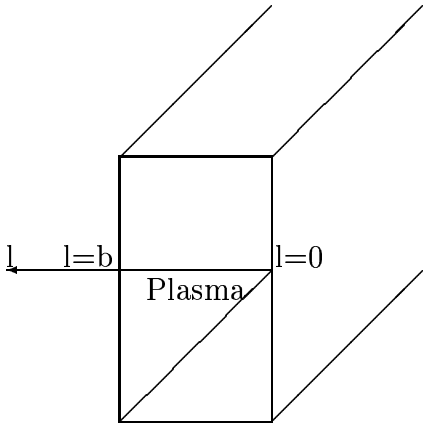

Figure 1.3: Diagram of the line of sight used in the escape probability formalism.

at l in principle depends upon ε at all the other points in the plasma (due to the dependence of the populations at l upon the local radiation field and hence upon the emission from elsewhere in the plasma) making the equation non-local as well. The method employed throughout this thesis is to solve the equation of radiative transfer by assuming that the emission coefficient is independent of the intensity term, thus making equation (1.1) linear and allowing it to be solved using an integrating factor approach. This assumption of linearity will be reasonable for plasmas which are not significantly optically thick and thus do not have a large degree of spatial coupling. Consider a line of sight through a plasma with the origin at the back face as in figure 1.3. Consider first of all a purely absorbing plasma with a constant absorption coefficient and with incident intensity $I(\nu, 0)$, the intensity observed at b will be given by

$$I(\nu, b) = I(\nu, 0)e^{-\int_0^b \alpha(\nu) dl} \tag{1.3}$$

If α is allowed to vary with respect to l and the plasma can also emit along the line of sight the emergent intensity will be

$$I(\nu, b) = \int_0^b \varepsilon(\nu, l)e^{-\int_l^b \alpha(\nu, l')l' dl'} dl + I(\nu, 0)e^{-\int_0^b \alpha(\nu, l) dl} \tag{1.4}$$

The emission and absorption coefficients are given by

$$\varepsilon(\nu, l) = \frac{1}{4\pi} A_{n' \to n} N_{n'}(l) \theta(\nu, l) \tag{1.5}$$

and

$$\begin{aligned} \alpha(\nu, l) &= B_{n \to n'} N_n(l) \theta(\nu, l) \\ &= N_n(l) \frac{c^2}{8\pi} \left(\frac{n'}{n} \right)^2 \frac{1}{\nu^2_{n' \to n}} A_{n' \to n} \theta(\nu, l) \end{aligned} \tag{1.6}$$

with

- $A_{n' \to n}$ = the Einstein-A value for the spontaneous emission $n' \to n$ $[s^{-1}]$
- $N_{n'}$ = Atomic population of level n' $[cm^{-3}]$
- N_n = Atomic population of level n $[cm^{-3}]$
- $\theta(\nu)$ = emission profile which is assumed equal to the absorption profile [s]
- $B_{n \to n'}$ = Einstein-B value for photo-absorption $n \to n'$ $[cm^2 s^{-1} sr^{-1}]$

To see the definition of the escape probability the line integrated emergent flux at b is written as follows:

$$\begin{aligned} I(b) &= \int_{line} \left[\int_0^b \varepsilon(\nu, l) e^{-\int_l^b \alpha(\nu, l') dl'} dl + I(\nu, 0) e^{-\int_0^b \alpha(\nu, l) dl} \right] d\nu \\ &= \frac{\int_{line} \int_0^b \varepsilon(\nu, l) e^{-\int_l^b \alpha(\nu, l') dl'} dl d\nu + \int_{line} I(\nu, 0) e^{-\int_0^b \alpha(\nu, l) dl} d\nu}{\int_{line} \int_0^b \varepsilon(\nu) dl + I(\nu, 0) d\nu} \\ &\quad \times \int_{line} \int_0^b \varepsilon(\nu) dl + I(\nu, 0) d\nu \\ &= \Theta_{n \to n'} \int_{line} \left[\int_0^b \varepsilon(\nu) dl + I(\nu, 0) \right] d\nu \\ &= \Theta_{n \to n'} \left[\frac{1}{4\pi} A_{n' \to n} \int_0^b N_{n'}(l) dl + \int_{line} I(\nu, 0) d\nu \right] \end{aligned} \tag{1.7}$$

Thus the escape probability, Θ, is defined as the ratio of the opacity modified escaping flux to the optically thin escaping flux, with both fluxes evaluated as line integrated values. That is,

$$\Theta_{n\to n'} = \frac{\int_{line}\int_0^b \varepsilon(\nu,l)e^{-\int_l^b \alpha(\nu,l')dl'}dld\nu + \int_{line} I(\nu,0)e^{-\int_0^b \alpha(\nu,l)dl}d\nu}{\int_{line}\int_0^b \varepsilon(\nu)dl + I(\nu,0)d\nu} \tag{1.8}$$

This is our general escape probability expression from which we derive all further results. In chapter 2 this expression is developed and evaluated for various plasma geometries and line profiles and in chapter 3 it is extended to include continuum frequencies.

The escape probability can be used as a parametric adjustment on the spontaneous emission coefficient allowing the line integrated emergent flux of a discrete spectral line transition, $n \to n'$, to be written as

$$I = \frac{1}{4\pi}\Theta_{n\to n'}\left[A_{n'\to n}\int_0^b N_{n'}(l)dl + \int_{line} I(\nu,0)d\nu\right] \tag{1.9}$$

1.2.3 Absorption factor and populations

Consider now the opacity effects from the perspective of atomic population modification. Writing out the spontaneous emission rate from level n' to n, and photo-absorptions to n' from n we get the following expression for the net photo-emission rate contribution to the statistical balance equations

$$\int_\Omega\int_{line}\varepsilon_{n'\to n}(\nu,l)d\nu d\Omega - \int_\Omega\int_{line}\alpha_{n\to n'}(\nu,l)u(\nu,l)d\nu d\Omega \tag{1.10}$$

where one considers emission from a volume element and photo-absorption to this element, neglecting stimulated emission, and $u(\nu,l)$ is the radiation density at l. Assuming that the emission from the volume element is uniform in all directions and integrating over the normalised emission profile, the net spontaneous emission rate is

$$\int_\Omega\int_{line}\varepsilon_{n'\to n}(\nu,l)d\nu d\Omega - \int_\Omega\int_{line}\alpha_{n\to n'}(\nu,l)u(\nu,l)d\nu d\Omega \tag{1.11}$$

$$= \int_\Omega \int_{line} \varepsilon_{n'\to n}(\nu,l)d\nu d\Omega \left[1 - \frac{\int_\Omega \int_{line} \alpha_{n\to n'}(\nu,l)u(\nu,l)d\nu d\Omega}{\int_\Omega \int_{line} \varepsilon_{n'\to n}(\nu,l)d\nu d\Omega}\right] \quad (1.12)$$

$$= \Lambda_{n\to n'}(l) \int_\Omega \int_{line} \varepsilon_{n'\to n}(\nu,l)d\nu d\Omega \quad (1.13)$$

That is

$$\Lambda_{n\to n'}(l) = 1 - \frac{\int_\Omega \int_{line} \alpha_{n\to n'}(\nu,l)u(\nu,l)d\nu d\Omega}{\int_\Omega \int_{line} \varepsilon_{n'\to n}(\nu,l)d\nu d\Omega} \quad (1.14)$$

$\Lambda_{n\to n'}$ is referred to as the absorption factor, following the terminology of Fischbacher et al. (2000). It can be seen that $\Lambda_{n\to n'}$ is one minus the total number of photo-absorptions at $\underline{r}$ divided by the total number of spontaneous emissions at $\underline{r}$. That is $\Lambda_{n\to n'}(l)$ represents the probability of a photon not being absorbed at position l in the plasma.

It is interesting to consider the limiting case of a black body. In this case the radiation density $u(\nu)$ is given by the source function equivalent to $\varepsilon(\nu,l)/\alpha(\nu,l)$. Also, if the plasma is a black body throughout its volume then $\alpha(\nu,l)$ and $\varepsilon(\nu,l)$ are independent of position. That is

$$\begin{aligned} \Lambda_{n\to n'}(l) &= 1 - \frac{\int_\Omega \int_{line} \alpha_{n\to n'}(\nu)\frac{\varepsilon(\nu)}{\alpha(\nu)}d\nu d\Omega}{\int_\Omega \int_{line} \varepsilon_{n'\to n}(\nu)d\nu d\Omega} \\ &= 0 \end{aligned} \quad (1.15)$$

Thus we have complete re-absorption of all emitted photons at any point l as expected from detailed balance under thermodynamic equilibrium conditions.

Note that for the absorption factor argument here we are considering absorption and emission at a point in the plasma. It is no longer the escaping flux that is of interest but the population modification at the point l. The photo-absorption transition rate can be absorbed into the spontaneous emission rate by including the absorption factor as a parametric adjustment. That is, photo-absorptions are included as negative spontaneous emissions. In our collisional-radiative calculations this is evaluated by multiplying the Einstein A-value for each transition by its corresponding absorption factor. Hence when one solves the statistical balance equations including these absorption factors the opacity modified population structure is produced.

The absorption factor expression of (1.14) is our starting expression for the opacity modifications to population structure. It is developed in chapter 2 for various geometries and line profiles. Chapter 3 then provides the extension of this expression to continuum frequencies.

Thus we have two basic expressions, (1.8) and (1.14), which can be used to account for the effects of opacity in an optically thick plasma.

1.2.4 Continuum opacity

There is of course a continuum equivalent to the discrete line opacity that we have looked at. Here we consider photo-ionisations and recombinations rather than photo-absorptions and spontaneous emissions. See Drawin (1970) for an example of continuum absorption factors derived and used in practice (in his case to evaluate plasma relaxation timescales). The continuum escape probability, which will also be referred to as the bound-free escape probability, is derived below. Note the similarities with the bound-bound expression.

The continuum integrated flux at b is written as

$$\begin{aligned} I(b) &= \int_{contm} \left[\int_0^b \varepsilon_{bf}(\nu,l) e^{-\int_l^b \alpha_{bf}(\nu,l')dl'} dl + I(\nu,0) e^{-\int_0^b \alpha_{bf}(\nu,l)ldl} \right] d\nu \\ &= \frac{\int_{contm} \int_0^b \varepsilon_{bf}(\nu,l) e^{-\int_l^b \alpha_{bf}(\nu,l')dl'} dl d\nu + \int_{contm} I(\nu,0) e^{-\int_0^b \alpha_{bf}(\nu,l)ldl} d\nu}{\int_{contm} \int_0^b \varepsilon_{bf}(\nu) dl + I(\nu,0) d\nu} \\ &\quad \times \int_{contm} \int_0^b \varepsilon_{bf}(\nu) dl + I(\nu,0) d\nu \\ &= \Theta_n \int_{contm} \int_0^b \varepsilon_{bf}(\nu) dl + I(\nu,0) d\nu \\ &= \Theta_n \left[\frac{1}{4\pi} A_{\kappa \to n} \int_0^b N_\kappa(l) dl + \int_{contm} I(\nu,0) d\nu \right] \end{aligned} \tag{1.16}$$

Note that κ represents the extension of bound states, n', into the continuum via the transformation $n' \to i\kappa$. The bound-free emission and absorption coefficients are taken from Menzel & Pekeris (1935). That is

$$\begin{aligned} \varepsilon_{bf}(\nu)d\nu &= \frac{1}{4\pi}\left[N_i f(v) b_\kappa dv\right]\left[N_e v \sigma_{\kappa n}\right] \\ \Rightarrow \varepsilon_{bf}(\nu) &= \frac{1}{4\pi}\left[N_i f(v) b_\kappa dv\right]\left[N_e v \sigma_{\kappa n}\frac{1}{d\kappa}\right]\frac{d\kappa}{d\nu} \end{aligned} \tag{1.17}$$

and

$$\alpha_{bf}(\nu) = N_n \frac{\pi e^2}{mc} f'_{n\kappa}\frac{d\kappa}{d\nu} g^{II}_{n\kappa} \tag{1.18}$$

where $f(v)$ is the Maxwellian velocity distribution for free electrons, $\sigma_{\kappa n}$ is the target area for free electron capture given by

$$\sigma_{\kappa n} = \frac{2^4}{3\sqrt{3}}\frac{e^2 h}{m^2 c^3}\frac{1}{\left[\frac{1}{n^2}+\frac{1}{\kappa^2}\right]}\frac{\kappa^2}{n^3} g^{II}_{\kappa n} \tag{1.19}$$

$f'_{n\kappa}$ is the bound-free oscillator strength and $g^{II}_{n\kappa}$ is the bound-free Gaunt factor.
Thus the escape probability Θ_n is defined as the ratio of the opacity modified escaping flux to the optically thin escaping flux, with both fluxes evaluated as continuum integrated fluxes. It follows that

$$\Theta_n = \frac{\int_{contm}\int_0^b \varepsilon_{bf}(\nu,l) e^{-\int_l^b \alpha_{bf}(\nu,l')dl'} dl d\nu + \int_{contm} I(\nu,0) e^{-\int_0^b \alpha_{bf}(\nu,l)dl} d\nu}{\int_0^b \int_{contm} \varepsilon_{bf}(\nu) d\nu + I(\nu,0) dl} \tag{1.20}$$

Note that there is no subscript κ on Θ_n in the definition shown here. This is because the escape probability is integrated over the whole set of continuum states κ, thus Θ_n represents the probability of a recombination photon, produced from an electron anywhere in the continuum recombining to the state n, escaping along the chosen line of sight. A more general expression that is not integrated over the whole continuum is presented in chapter 3.
In a similar manner the absorption factor for bound-free transitions may be written in its general form. The net ionisation rate is given by

$$\int_\Omega \int_{contm} \varepsilon_{\kappa\to n}(\nu,l) d\nu d\Omega - \int_\Omega \int_{contm} \alpha_{n\to\kappa}(\nu,l) u(\nu,l) d\nu d\Omega \tag{1.21}$$

$$= \int_{\Omega}\int_{contm} \varepsilon_{\kappa\to n}(\nu,l)d\nu d\Omega \left[1 - \frac{\int_{\Omega}\int_{contm} \alpha_{n\to\kappa}(\nu,l)u(\nu,l)d\nu d\Omega}{\int_{\Omega}\int_{contm} \varepsilon_{\kappa\to n}(\nu,l)d\nu d\Omega}\right] \quad (1.22)$$

$$= \Lambda_{n\to\kappa}(l)\int_{\Omega}\int_{contm} \varepsilon_{\kappa\to n}(\nu,l)d\nu d\Omega \quad (1.23)$$

where the absorption and emission coefficients have the same definitions as in the bound-free escape factor case. That is, the absorption factor for bound-free photo-absorption is given by

$$\Lambda_{n\to\kappa}(l) = 1 - \frac{\int_{\Omega}\int_{contm} \alpha_{n\to\kappa}(\nu,l)u(\nu,l)d\nu d\Omega}{\int_{\Omega}\int_{contm} \varepsilon_{\kappa\to n}(\nu,l)d\nu d\Omega} \quad (1.24)$$

The similarity between equations (1.20), (1.24) and the bound-bound counterparts (1.8), (1.14) is clear. This similarity is shown formally in chapter 3 where the bound-bound expressions are shown to analytically continue into the bound-free ones upon application of the transformation $n' \to i\kappa$.

1.2.5 Line broadening

In practice it is found that the escape probability and absorption factor expressions can be highly sensitive to the emitting and absorbing line profiles, see for example the illustrations in Behringer (1998). For this reason, and in order to accurately compare any theoretical spectrum (whether optically thin or thick) with that observed it is necessary to model emission and absorption line profiles with a high degree of precision. This is especially true for the high series work presented in chapter 5 where the theoretical electron broadened line widths are used as a density diagnostic. There are many standard textbooks which give an overview of the basic theory behind line broadening (see Griem, 1974, Griem, 1997, Sobelman et al., 1981 and chapter 13 of Bates, 1964). Most work in this area concentrates on the evaluation of pressure broadening as it is the most complex and often the most important line broadening mechanism. The next few sections will give a brief overview of the main broadening expressions, concentrating on a description of the physical processes behind each mechanism. The following sections will lay out the background theory necessary to put the line profile calculations of chapters 2, 3, 4 and 5 into context. There exists a

wide range of broadening mechanisms including Doppler broadening, natural broadening, pressure broadening as well as instrumental effects which alter the observed profile. The basic line profile expressions for each of these mechanisms are presented along with any approximate expressions that are used in the later chapters.
In practice one usually assumes that the emission and absorption profiles are identical. That is, in the time from photo-absorption to subsequent re-emission, there have been sufficient collisions such that the direction of the emitted photon is not related to that from which it was absorbed. Thus the emitted photon has been thermalised and the resultant emission profile is governed by the same plasma properties that lead to the absorption profile. This assumption is often referred to as complete frequency redistribution (CRD) and is made throughout the rest of the thesis with the possibility of different emission and absorption profiles being included at a future date if necessary.

Temperature effects

The broadening due to the inherent thermal motion of the emitting or absorbing atoms, provided their velocity distribution is Maxwellian with characteristic temperature T, results in a line profile given by the normalised Doppler expression

$$\theta(\nu) = \frac{1}{\sqrt{\pi}\Delta\nu_D} e^{-\left(\frac{\nu-\nu_0}{\Delta\nu_D}\right)^2} \tag{1.25}$$

where

$$\Delta\nu_D = \frac{1}{\nu_0}\sqrt{\frac{2kT}{m}} \tag{1.26}$$

is the Doppler half width of the gaussian line profile.

Natural broadening

There exists a mechanism usually referred to as natural broadening, resulting from the finite lifetime of the emitting atom in its excited state (as predicted by the Heisenberg uncertainty principle, $\Delta E \Delta t \approx h/2\pi$).

Natural broadening exists independently of any external influences on the emitting atom. It results in a profile known as Lorentzian with a width characterised by $\Delta\nu_L = A_{n'\to n}/2\pi$.
The profile expression is of the form

$$\theta(\nu) = \frac{(\Delta\nu_L)^2}{(\nu - \nu_0)^2 + 4(\Delta\nu_L)^2} \tag{1.27}$$

This broadening mechanism is negligible when compared to pressure and doppler broadening for the cases that are usually encountered in fusion and astrophysical plasmas.

Density effects

For dense plasma conditions it is likely that both natural broadening and doppler broadening will be negligible compared with the collisional broadening induced by the charged particles of the plasma, interacting through the Stark effect. Neutral broadening and the long range Van der Waals broadening will be neglected with only broadening due to electrons and ions being considered in this work. The most general expression for a Stark broadened line profile is

$$\theta(\omega) = \frac{1}{\pi} Re \left\{ \int_0^\infty exp(i\omega s) C(s) ds \right\} \tag{1.28}$$

where $C(s)$ is referred to as the autocorrelation function of the light amplitude and is evaluated from quantum mechanical knowledge of the perturber and emitter. The complete treatment of such broadening is complicated by the fact that slow moving perturbers interact with the emitter in a different way to the faster perturbers. Usually one of two limiting approximations is used to account for the broadening effects of the charged perturbers. If the perturber is fast all the broadening collisions will be statistically independent from each other and can be individually accounted for. This is known as the 'impact approximation' (Lorentz, 1906) and leads to a Lorentzian profile. If the perturber is very slow then it can be considered to be stationary from the emitter's point of view and the broadening effects of the resultant field due to all

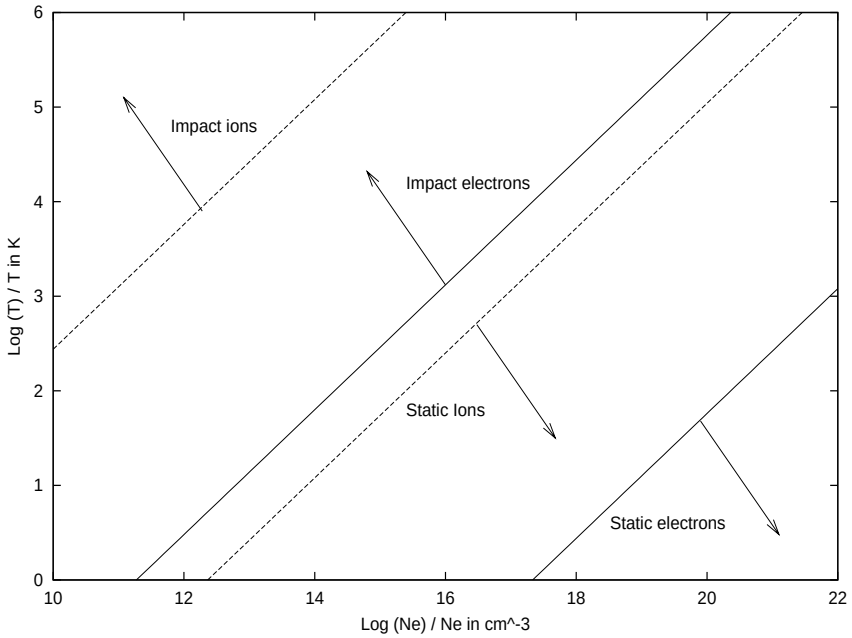

Figure 1.4: Range of validity of broadening approximations for $H\alpha$, taken from Stamm et al. (1998).

the 'stationary' perturbers estimated; this is referred to as the 'quasi-static approximation' (Holtsmark, 1919).

Both ions and electrons broaden the lines through the Coulomb interaction between themselves and the electrons in the emitting atom. Thus the only difference between the broadening effects of the ions and electrons comes from their differing speed, with the electrons typically having a much higher average thermal velocity than the ions. Thus typically the electrons are treated in the impact and the ions in the quasi-static approximation. It should be noted that reality does not always fall into either of these two limiting approximations, but in the intermediate regime between the two. In figure 1.4 an illustration of the boundaries of these two approximations for ions and electrons is shown for some plasma conditions likely to occur in practice. The arrows indicate the regimes for which the impact and quasi-static approximations are valid. Note that the graph is only valid for $H\alpha$, but could in principle be evaluated for any line.

The impact approximation

As stated previously, the impact approximation assumes that collisions are statistically independent and thus the total broadening effect of the collisions can be evaluated from the sum of each broadening collision.

In practice the impact approximation is usually valid for the treatment of electron collisional broadening due to their fast thermal motion and thus the short timescale of their collisions with the emitting atom. This broadening in isolation produces a Lorentzian profile with characteristic half widths which are primarily functions of the perturber density. Griem (1960) derives a simplified expression for a transition from $n' \rightarrow n$ with an electron broadened half width given by

$$\gamma = 5.6 \times 10^{-6} N^{1/3} Z^{-1} T^{-1/2} \left[log_{10} \left(\frac{4 \times 10^6 TZ}{n' N^{1/2}} \right) - 0.125 \right] \frac{n'^5 + n^5}{n'^2 - n^2} \qquad (1.29)$$

Note that if Doppler broadening is also significant then the resultant profile would be a convolution of a Lorentzian and Gaussian profile which is referred to as a Voigt profile. Such profiles are often available as tables, e.g. Allen (1991).

The Quasi-static approximation

At the other extreme, it may be the case that the charged perturbers have negligible motion during the lifetime of the emitting upper level. Under these circumstances the effects of the perturbers can be best modelled as a field broadening the line. The quasi-static approximation is usually applied as follows. The perturbers are assumed to be stationary and one calculates the effect of the consequent static electric field on the lines via the Stark effect. One then accounts for the statistical distribution of the field by evaluating the probability distribution of the electric field. The Stark profiles are then averaged over this distribution.

The probability distribution of the ion electric field is usually denoted by $W(F)$ with $F = E/E_0$ and $E_0 = e/r_0^2$, where r_0 is the mean distance between particles in the plasma. This represents the probability that a certain electric field (E), due to the presence of surrounding ions, will be experienced by the emitting atom and is usually referred to as the 'statistical microfield distribution function'. These have

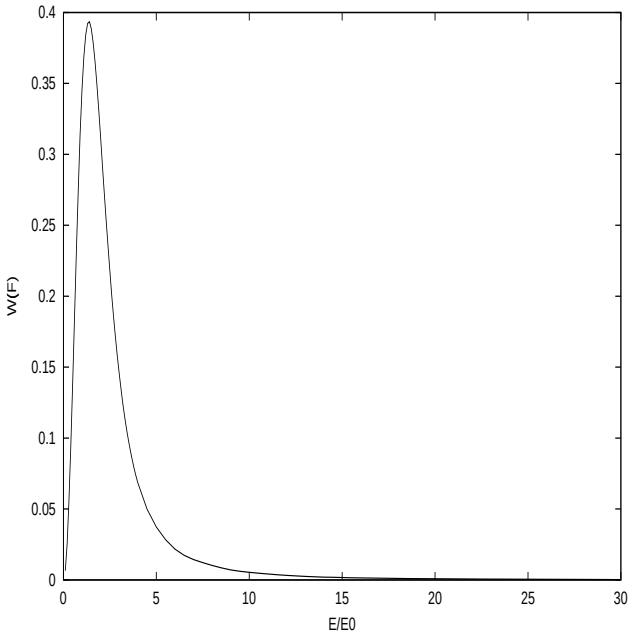

Figure 1.5: Ion-microfield plotted for plasma parameters as described in the text.

been widely evaluated in work such as that of Hooper (1966) and Hooper (1968). In the ideal gas limit they reduce to the Holtsmark field (Holtsmark, 1919). Figure 1.5 shows a microfield distribution function for a plasma consisting of 99% D^+ and 1% D^0 at an electron temperature of $1eV$ and an electron density of $1 \times 10^{14} cm^{-3}$. The APEX code (Iglesias, Lebowitz & McGowan, 1983) is used throughout this thesis in any microfield calculations. This routine is regarded as being highly accurate and is widely used; see chapter 3 of Griem (1997) for more details on the use of this code.
It is not normally appropriate to model the effects of the electrons using this technique. The ion collisions on the other hand are often modelled in this approximation. Their slower velocities means that they often fall into the regime where their interactions with the emitting atom are over long periods of time. In general a reasonable guide in determining the balance between the two approaches is that that the quasi-static approximation is valid if the linewidth is large compared with the inverse of a typical collision time, and the impact approximation is valid if this value is small when compared to the inverse of a typical collision time.
Note that in practice, one does not have only one broadening mechanism influencing

the line profile. In dense plasmas one is likely to get influences from both the electrons and the ions which must be simultaneously accounted for.

Accounting for both ion and electron collisional broadening

In practice it is common to take the following approach. The emitting atom is assumed to lie in a constant electric field produced by the 'stationary' ions which produces a Stark broadened set of lines. These lines are then further broadened by electron collisions within the impact approximation. Finally the statistical distribution of the ionic field is accounted for by averaging the broadened set of lines with the probability distribution function of the ion field. Thus the electrons are accounted for using the impact approximation and the ions via the quasi-static approximation. The quantum mechanical form of this is shown below. One would then convolve the resulting profile with the Doppler profile and instrumental function if appropriate.

This process is evaluated numerically in the Pim Pam Poum (PPP) code (Talin et al., 1995, Talin et al., 1997). This code is well tested and provides an accurate evaluation of Stark broadened profiles due to ion and electron perturbers. The code takes in atomic data containing energy level information and spontaneous emission values as well as the set of plasma parameters for which the profile is to be evaluated and returns the emission coefficient for the transition of interest (i.e. $\frac{1}{4\pi}A_{n'\rightarrow n}N_{n'}\theta(\nu)$). The profile can be either normalised or not and the population density can be set to the Saha-Boltzmann values or a pre-calculated population density distribution used. Thus the PPP code, coupled with the ADAS collisional-radiative codes can provide accurate line profiles with absolute intensities for a wide range of plasma conditions. An example of a profile evaluated using the PPP code is shown in figure 1.6. The $9-2$ Balmer series line is shown for the case where only the electron broadening and then the ion plus electron broadening is considered. It can be seen that for these plasma conditions, the electron broadening dominates the line shape, although the ion broadening is still significant.

In the thesis work presented here a more approximate method which captures the main behaviour of all the broadening mechanisms is also used. This fast, approximate method is of use particularly in chapter 5 where a large number of hydrogen series

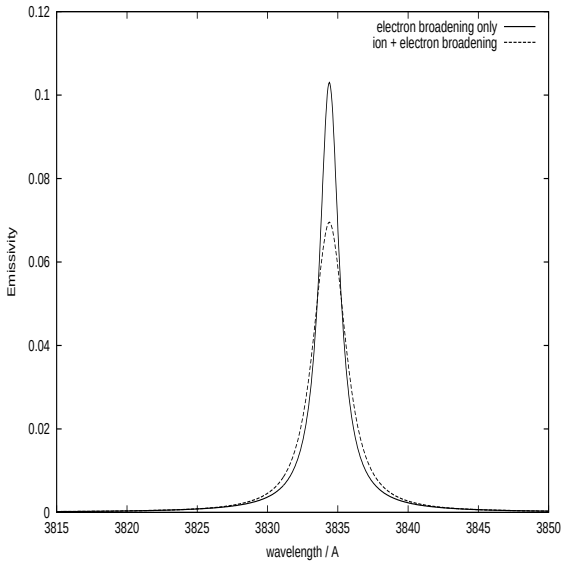

Figure 1.6: Example of the hydrogen 9-2 Balmer series spectral line profile as evaluated by the PPP code for an electron density of $1 \times 10^{14} cm^{-3}$ and an electron temperature of $1 \times 10^4 K$.

profiles need to be evaluated and the accuracy of the very high series member is not of primary importance. Griem (1960) derives a simplified algebraic expression for evaluating ion and electron broadened profiles for hydrogen, with the ions treated in the quasi-static and the electrons in the impact approximation. The same basic expression is also given in Sobelman et al. (1981). The expressions are designed to be quick to apply, using look-up tables which cover a reasonable range of electron and ion broadening half widths. The basic expression used is

$$I = \frac{1}{F_0} \frac{1}{K_{nn'}} T(\beta, \gamma) \tag{1.30}$$

$T(\beta, \gamma)$ is found from the look-up tables, γ (the half width due to electron broadening) is evaluated from equation (1.29), $F_0 = 2.61 e N^{\frac{2}{3}}$ is the Holtsmark normal field strength, $K_{nn'} = 5.5 \times 10^{-5} Z^{-5} \frac{(nn')^4}{n'^2 - n^2}$, $\beta = a / K_{nn'}$ with $a = \Delta\lambda / F_0$.
In evaluating this approximate expression an extension was made to make it more robust. As one progresses up a given series, electron broadening dominates, and the profiles tend towards Lorentzian profiles with their half-widths determined purely

by the electron broadening expression. Thus for values of β that fall outside Griem's table, it was assumed that electron broadening dominated and a Lorentzian expression was used with a half-width given by γ. This is not always a valid approximation. For example if the ion broadening is still significant then the calculated line will not be as broad as it would in reality. As is shown in chapter 5, Griem's expression prove to be valid for many of the plasma conditions that are investigated in this thesis; see section 5.2.3 for more details.

Thus the preferred method for profile calculation in this thesis has been as follows. For simplified conditions, where Doppler or simple Lorentzian profiles are valid, no complex profile calculations are done. For conditions where significant Stark broadening occurs in both the ions and electrons, the PPP code is used, especially for lines that are to be used for diagnostic purposes. In chapter 5 very high hydrogen series member profiles must be evaluated. The approximate expression is used under such circumstances to supplement the PPP results for the low series member lines.

Optical thickness effects

It is also possible for opacity to modify a given observed line profile. On travelling through a plasma it is more likely that line centre photons will be absorbed as compared to those in the line wings. This can be seen from equation (1.8) for the absorption factor, where α is significantly higher at line centre as compared with the line wings. Thus the profile that finally emerges from the body of the plasma could have reduced intensity at the line centre, leading either to a line flattening or even a line inversion. See figure 1.7 for examples of this evaluated using ADAS 214 for the case of a parabolic density distribution within a cylindrical plasma.

1.2.6 Population modelling

The simplifying assumptions commonly made when modelling plasma atomic populations can best be understood upon consideration of the various atomic and plasma lifetimes. These lifetimes allow one to calculate an 'equilibrium time constant' describing the time taken for each plasma constituent to relax to its equilibrium state.

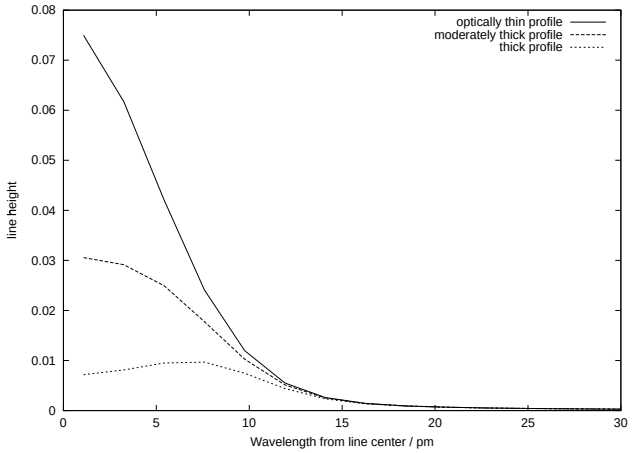

Figure 1.7: Examples of opacity modified line profiles evaluated using ADAS 214. The top profile is the optically thin one. The next lower one is the moderately thick case, note that its top is flattened. The lowest case is the optically thick case, note that its centre is inverted.

The relative values of these time constants determines the optimal atomic modelling approach. Define τ_{plasma} such that it describes the dynamical timescale of the plasma, that is the timescale upon which the typical plasma parameters vary (or often in the case of laboratory plasmas, the timescales for which the plasma exists). τ_{plasma} also describes the typical timescale for plasma particles to cross temperature and density scale lengths. Comparing the time constant for each plasma process with τ_{plasma} gives an indication of whether that process has time to equilibriate before the plasma conditions vary. Due to typical plasma confinement times τ_{plasma} is of the order of one second for the core plasma of a fusion tokamak and as low as $10\,ms$ for the divertor plasma. One can also define certain 'extrinsic' time constants, such as τ_{e-e}, giving the time for electron-electron collisions to thermalise the free electrons, τ_{i-i} describing the equivalent ion-ion equipartition and τ_{i-e} for ion-electron equilibration (i.e. the time for the electron and ion distributions to reach the same characteristic temperature). Define τ_{ion} such that it describes the ionisation relaxation timescale for the plasma. There also exist certain 'intrinsic' time constants describing states within the atomic system under consideration. τ_m gives the relaxation time for the metastable states, τ_o for the ordinary excited states and τ_a for the auto-ionising states.

Before looking at typical values for each of these time constants, consider the case

where all of the intrinsic and extrinsic time constants are much less that τ_{plasma}, the plasma is in isolation and there is no escaping radiation field. In this case the plasma is said to be in 'thermodynamic equilibrium' (TE) and each process is balanced by its inverse (referred to as the 'principle of detailed balance'). Under such conditions, the free plasma particles (electrons, ions etc) have Maxwellian velocity distributions characterised by the same temperature, described by

$$f(\mathbf{v}) = 4\pi \left(\frac{m}{2\pi kT}\right)^{\frac{3}{2}} e^{-(m\mathbf{v}^2)/(2kT)}\mathbf{v}^2 \tag{1.31}$$

The plasma internal radiation field is that of a black body and given by the Planck function:

$$u(\nu) = \frac{8\pi h\nu}{c^3}\left(e^{h\nu/kT} - 1\right) \tag{1.32}$$

and the bound states of the atoms and ions have Boltzmann distributions, such that the ratio of population densities of bound states i and j is given by

$$\frac{N_i}{N_j} = \frac{\omega_i}{\omega_j} e^{(I_i - I_j)/(kT)} \tag{1.33}$$

where ω_i and ω_j are the statistical weight of levels i and j. The absolute populations of level i are given by the Saha-Boltzmann equation

$$N_i = N_+ N_e \left(\frac{h^2}{2\pi mkT}\right)^{\frac{3}{2}} \frac{\omega_i}{2\omega_+} e^{(I_i)/(kT)} \tag{1.34}$$

where ω_+ and N_+ are the parent statistical weights and populations densities of the parent system. The TE assumption enabled some degree of analysis to be performed on certain plasmas. For instance the fact that the sun's photosphere is approximately black body and emits a characteristic Planckian spectrum was used to determine that the photosphere has a temperature of $\sim 6,000K$.

Most plasmas have an escaping radiation field which acts to move the plasma away from conditions of TE. If all intrinsic and extrinsic time constants are much less that τ_{plasma} the collisions are efficient enough to overcome the population losses due to radiative decay, this is referred to as 'local thermodynamic equilibrium' (LTE). In

this case the TE equations hold for the free and bound particles, but the radiation field is that of a diluted black body. All systems will have a critical density above which collisions dominate over spontaneous emission losses. Spontaneous emission coefficients typically scale as $\sim 1/n'^5$ (n' being the upper quantum shell), while electron collisional cross section scale as $\sim 1/n'^2$. Thus as one moves to higher quantum shells, LTE conditions becomes more valid.

If collisions are not able to compensate for radiation lossed the plasma is in 'non-local thermodynamic equilibrium' (NLTE). For most plasmas $\tau_{e-e} \ll \tau_o \ll \tau_m$ and for many plasma conditions (including fusion tokamaks) $\tau_{plasma} \sim \tau_{ion} \sim \tau_m$. In these conditions the free electrons have time to collisionally thermalise and form a Maxwellian velocity distribution. The excited states vary on a much quicker timescale that the metastables and can be considered to be in quasi-static equilibrium with them. The metastables thermalise on similar timescales to the plasma dynamics, as does the ionisation balance. So both the metastables and ionisation balance must be solved for dynamically within the context of plasma transport and ionisation balance codes. The excited state populations can then be evaluated with respect to the metastable populations. In solving for the excited state populations one must account for all the possible transitions between excited states as well as transitions to the metastables of the same and adjacent ionisation stages. This is referred to as the 'principle of statistical balance'. All the rates can be assembled into a system of equations describing the ways in which each atomic state can be populated and depoulated. This approach is referred to as the 'collisional-radiative' (C-R) approach, developed by Bates et al. (1962) and generalised by Summers & Hooper (1983) to account for metastables.

Consider an atomic energy level i and assemble all the collisional, radiative and induced rates that can populate or depopulate it. The sum of all these rates equals the rate of change of the population density in that level. The general form of the statistical balance equations is as follows

$$\sum_{i'>i} \left[A_{i'\to i} + \int_{line} u(\nu) B_{i'\to i} d\nu + N_e q^{(e)}_{i'\to i} + N_e q^{(p)}_{i'\to i} \right] N_{i'}$$

$$
\begin{aligned}
&+ \sum_{i''<i} \left[\int_{line} u(\nu) B_{i''\to i} d\nu + N_e q^{(e)}_{i''\to i} + N_e q^{(p)}_{i''\to i} \right] N_{i''} \\
&+ N_e N_+ \alpha^{(r)}_i + N_e^2 N_+ \alpha^{(3)}_i + N_e N_+ \int u(\nu) B_{\kappa\to i} d\kappa \\
&= \left[\sum_{i'>i} \left[\int_{line} u(\nu) B_{i\to i'} d\nu + N_e q^{(e)}_{i\to i'} + N_e q^{(p)}_{i\to i'} \right] \right. \\
&+ \sum_{i''<i} \left[A_{i\to i''} + \int_{line} u(\nu) B_{i\to i''} d\nu + N_e q^{(e)}_{i\to i''} + N_e q^{(p)}_{i\to i''} \right] \\
&+ \left. \int u(\nu) B_{i\to\kappa} d\kappa + N_e q^{(e)}_{i\to\varepsilon} + N_e q^{(p)}_{i\to\varepsilon} \right] N_i + \frac{dN_i}{dt}
\end{aligned}
\tag{1.35}
$$

Where .....

- $A_{i'\to i}$ - spontaneous emission from $i' \to i$
- $u(\nu) B_{i'\to i}$ - stimulated emission from $i' \to i$
- $u(\nu) B_{i\to i'}$ - photo-absorption from $i' \to i$
- $N_e q^{(e)}_{i'\to i}$ - electron collisonal de-excitation from $i' \to i$
- $N_e q^{(p)}_{i'\to i}$ - proton collisonal de-excitation from $i' \to i$
- $N_e q^{(e)}_{i\to i'}$ - electron collisional excitation from $i \to i'$
- $N_e q^{(p)}_{i\to i'}$ - proton collisional excitation from $i \to i'$
- $\int u(\nu) B_{i\to\kappa} d\kappa$ - photo-ionisation from i
- $N_e q^{(e)}_{i\to\varepsilon}$ - electron collisional ionisation from i
- $N_e q^{(p)}_{i\to\varepsilon}$ - proton collisional ionisation from i
- $N_e N_+ \alpha^{(r)}_i$ - radiative recombination to i
- $N_e^2 N_+ \alpha^{(3)}_i$ - three body recombination to i
- $N_e N_+ \int u(\nu) B_{\kappa\to i} d\kappa$ - stimulated recombination to i

A set of such equations can be assembled with one equation for each atomic energy level, i, that exists. It is the simultaneous solution of this set of equations that produces the atomic population structure. Because the excited state population values are in equilibrium with the metastable populations their dN_i/dt terms can be set to zero.

One can write this set of equations in matrix notation indexed by i and j. Matrix elements such as C_{ij} are made up from equation (1.35) and describe all the processes by which level i can be populated from level j, written formally as

$$C_{ji} = A_{i\to j} + N_e q^{(e)}_{i\to j} + N_p q^{(p)}_{i\to j} + \ .... \tag{1.36}$$

The diagonal elements, such as C_{ii}, are the total loss rates from level i, given by

$$-C_{ii} = \sum_{j\neq i} C_{ji} + N_e q^{(e)}_{i\to\varepsilon} \tag{1.37}$$

Denoting metastable levels with greek subscripts, using the usual summation notation one has the following rate equation for level ρ of ionisation stage (z)

$$\frac{dN^{(z)}_\rho}{dt} = C_{\rho\sigma}N^{(z)}_\sigma + C_{\rho j}N^{(z)}_j + C_{\rho\sigma_+}N^{(z+1)}_{\sigma_+} + C_{\rho\sigma_-}N^{(z-1)}_{\sigma_-} \tag{1.38}$$

and for excited state i one has

$$0 = C_{i\sigma}N^{(z)}_\sigma + C_{ij}N^{(z)}_j + C_{i\sigma_+}N^{(z+1)}_{\sigma_+} + C_{i\sigma_-}N^{(z-1)}_{\sigma_-} \tag{1.39}$$

where σ_- and σ_+ denote metastables of adjacent ionisation stages. The resulting set of equations are assembled into the collisional-radiative matrix and solved by matrix inversion for the excited state populations with respect to the metastables (which are assumed known from dynamical ionisation balance). For computational simplification the C-R matrix equation is conventionally solved using scaled temperatures and densities

$$t_e = \frac{kT_e}{I_H}\frac{1}{z_0^2} \tag{1.40}$$

$$t_r = \frac{kT_r}{I_H}\frac{1}{z_0^2} \tag{1.41}$$

$$\rho_e = 2^5\sqrt{\frac{\pi}{3}}\frac{\pi a_0^3}{\alpha^3}\frac{N_e}{z_0^7} \tag{1.42}$$

with similar definitions for the ion temperatures and densities. The population solution is expressed as deviation factors (referred to as 'b-factors') from Saha-Boltzmann values, defined via

$$N_i = N_+ N_e \left(\frac{h^2}{2\pi mkT}\right)^{\frac{3}{2}} \frac{\omega_i}{2\omega_+} e^{I_i/kT} b_i \tag{1.43}$$

Solving the equations for the b-factors provides a solution that is more easily interpreted (i.e. in 'LTE-space') and leads to cancellations which make the system numerically more stable. The equations can also be solved for c-factors ($= b - 1$), or $e^{I_i/kT_e} b_i$ factors. The choice of the 'picture' of the solution is determined by that which provides the most numerically stable solution. For example for very low T_e the b_i values can be very close to zero for the excited states and lead to numerical errors, whereas a solution in terms of $e^{I_i/kT_e} b_i$ is much more stable.

Coupling schemes

In this work, a general population approach is developed which is valid for all ions, that is, of both light and heavy species in arbitrarily highly ionised systems. Thus energy level structures have to be dealt with which range from L-S terms (Russell-Saunders coupling) for light and near neutral systems to intermediate coupled levels for medium weight and fairly ionised systems ($z < 40$) to j-j coupled heavy, very highly ionised systems.

Although the existing light element coupling scheme, where a bundled-nS or bundled-nlSL electron sits on top of an L-S coupled core, provides the necessary precision for spectroscopic analysis of typical light element spectra, it encounters problems when extended to the sytems that are dealt with in this thesis. For heavy species the relativistic splitting of terms into fine structure levels becomes significant and the

resulting breakdown in L-S coupling, along with significant configuration interaction, means that the fine structure low lying level populations can no longer be assumed to be statistical and must be treated individually. This is reflected spectroscopically, where a J-resolved energy level picture is usually used for analysis of medium/heavy species. Also, the picture of a bundled-nS electron built on top of a metastable parent can no longer be sustained for highly excited populations. For such electrons, relativistic interaction dominates over electrostatic leading to spin system breakdown and it is more appropriate to model a weakly coupled nl electron built on a L-S coupled or intermediate coupling J core. This system is sometimes referred to as 'j-l coupled'. It should also be recognised that there is normally a change of the most appropriate coupling scheme as one passes from low levels to highly excited levels. Thus for the model presented in chapter 4 the following bundling regimes are defined, with each merging smoothly into the next as the levels become statistically populated and can be bundled over.

$$\begin{aligned} n < n_0 &: N_{(\gamma\pi J)} \\ n_0 < n \leq n_1 &: N_{(\gamma_p\pi_p J_p)nljJ} \\ n_1 < n \leq n_2 &: N_{(\gamma_p\pi_p J_p)nlj} \\ n_2 < n \leq n_3 &: N_{(\gamma_p\pi_p J_p)nl} \\ n_3 < n \leq n_4 &: N_{(\gamma_p\pi_p J_p)n} \end{aligned} \tag{1.44}$$

For $n < n_0$, the valence electron is in the core configuration and the multielectron states are in the form $\gamma\pi J$, where γ is the configuration, π the parity and J the total angular momentum. For the rest of the bundling regimes one has an nl electron built upon a J-coupled parent state $(\gamma_p\pi_p J_p)$ (henceforth referred to as the 'bundle-$(J_p)nl$' model). For $n_0 < n \leq n_1$ the J levels are treated individually, at n_1 they are effectively degenerate and statistically populated relative to each other and can be bundled together. Similarly at n_2 the j-states are effectively degenerate and statistically relatively populated and can be bundled over and at n_3 the l-states can be bundled over. Determining the point at which the collisional redistributive rates overcome the radiative decay rates allows the bundling cut-offs (i.e. $n_0 \rightarrow n_4$) to be evaluated. Work is presented in chapter 4 outlining a scheme by which these cut-offs can be detected automatically and used in the assembly of the appropriate collisional-radiative matrix - note that the increase in size of the working matrices necessary for this scheme is still within the capacity of modern workstations. The set of coupled models shown here marks a significant improvement over the existing scheme for light elements.

With the range of coupling schemes used in this new model it is necessary to define appropriate transformations between systems. Thus rates must be evaluated for cross-coupling transitions as well as for transitions within the new bundle-$(J_p)nl$ model. As most rate expressions contain their angular components within Gaunt factors, this leads to a need to derive Gaunt factors which deal with all the possible initial and final states of this new scheme. This has been done and the results summarised in table 4.1, with the details given in appendix A.

A progression of coupling schemes is used throughout this thesis. Chapters 1 and 2 examine opacity in light elements (C II in section 1.3.1 then generic light elements for the opacity work of chapter 2) using the existing ADAS light element coupling scheme. With the extension of the opacity work to high lying hydrogenic populations in chapters 3 and 5, a coupling scheme where an nl electron sits on a bare nucleus is used. This leads on to the high level heavy species work of chapter 4 where the full bundle-$(J_p)nl$ model is used. Note that the code developed in chapter 4 is not the final heavy species one, but the hydrogenic module which will form the high quantum shell component of the final code. The concept of an excited hydrogenic electron coupled to a J-resolved core is a valid approximation for the highly excited states of heavy species, and provides a module that we can test against existing hydrogenic light element codes.

1.3 Examples of opacity and spectral series in astrophysical and laboratory plasmas

1.3.1 The solar atmosphere : branching line ratios as a diagnostic for deducing optical depth

Escape probabilities have often been used to diagnose optical depths (Jordan, 1967; Doyle & McWhirter, 1980; Keenan & Kingston, 1986; Kastner, 1999). As a demonstration of this technique consider an example taken from the study of Brooks et al. (2000). Observations were carried out on September 7th, 1996 using the SUMER (Wilhelm et al., 1995) instrument onboard the SOHO (SOlar and Heliospheric Observatory) spacecraft. The observations consisted of 18 cross-limb scans (in 1.9 arc sec steps) of the wavelength region surrounding various multiplets. We present the results for the C II $2s^2 2p\ ^2P$ - $2s2p^2\ ^2S$ (1036 Å) multiplet, see figure 1.8. The objective was to diagnose opacities from branching line ratio observations from the solar limb. This follows on from Doyle & McWhirter (1980) who performed a similar study on the C III $2s2p\ ^3P$ - $2p^2\ ^3P$ ($1175\mathring{A}$) multiplet.

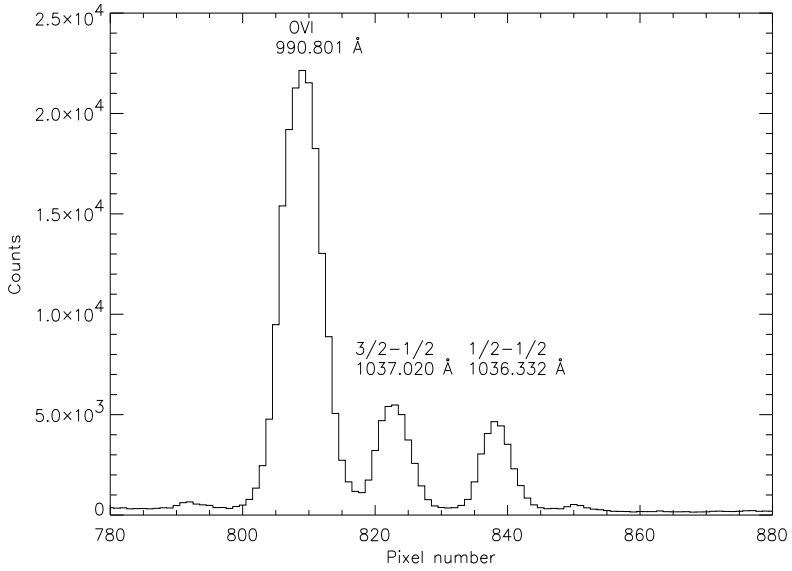

Figure 1.8: Spectrum of the CII multiplet used in the branching ratio study. The large line on the left hand side is a strong Oxygen line

In scanning across the limb of the sun, the geometrical thickness of the line of sight increases. Opacity effects in thick lines means that their fluxes will vary differently from those of the thin lines. The ratio of such lines allows the effects of opacity to be isolated.

Using equation (1.9) we see that the ratio of two spectral line intensities can be written as

$$\frac{I_{n_2' \to n_2}}{I_{n_1' \to n_1}} = \frac{\Theta_{n_2' \to n_2}}{\Theta_{n_1' \to n_1}} \frac{A_{n_2' \to n_2}}{A_{n_1' \to n_1}} \frac{\int_0^b N_{n_2'} dl}{\int_0^b N_{n_1'} dl} \tag{1.45}$$

where n_1 and n_1' represent the lower and upper level indices respectively of line 1. Similarly n_2 and n_2' represent the lower and upper level indices respectively of line 2. If the lines originate from the same upper level then $n_1' = n_2' = n'$ thus $N_{n_1'} = N_{n_2'} = N_{n'}$. That is,

$$\frac{I_{n_2' \to n_2}}{I_{n_1' \to n_1}} = \frac{\Theta_{n' \to n_2}}{\Theta_{n' \to n_1}} \frac{A_{n' \to n_2}}{A_{n' \to n_1}} \tag{1.46}$$

Thus observations of the ratio of two lines emitted from a common upper level,

C II $2s2p^2\ ^2S_{\frac{1}{2}}$ in our case, eliminates the dependence on the upper level population densities and isolates the opacity influence on the line ratio. Since the A-values are known, an observation of the intensity ratio leads to a deduced escape probability ratio, which in turn leads to an optical depth determination. The optical depth at line centre, taken from Mitchell & Zemansky (1961), is given by

$$\begin{aligned} \tau_0 &= \alpha(\nu_0)b \\ &= 1.16 \times 10^{-6}\sqrt{\frac{M}{T_i}}\lambda_0 f_{n'\to n} N_n b \end{aligned} \tag{1.47}$$

where
T_i is the ion temperature [K].
M is the atomic mass number of the absorbing atoms [a.m.u.].
ν_0 is the central frequency of the transition of interest [Hz].
λ_0 is the central wavelength of the transition of interest [cm].
N_n is the number density of the lower level of the transition [cm^{-3}].
$f_{n'\to n}$ is the absorption oscillator strength [dimensionless].
b is the physical thickness of the plasma along the line of sight [cm].

Thus the ratio of two optical depths corresponding to lines which arise from the same upper level, n', is given by

$$\frac{\tau_{0,n_1\to n'}}{\tau_{0,n_2\to n'}} = \frac{\lambda_{0,n_1\to n'}}{\lambda_{0,n_2\to n'}}\frac{f_{0,n_1\to n'}}{f_{0,n_2\to n'}}\frac{N_{n_1}}{N_{n_2}} \tag{1.48}$$

As the C II lines are close together, the ratio of the central wavelengths is close to unity and the τ ratio is controlled by the ratio of the two oscillator strengths and lower level populations, which are statistically populated. An optically thin population calculation using ADAS was done to verify this. It was found that the lower ground term relative populations were very close to statistical and insensitive to plasma conditions or finite optical depths. The following layer averaged escape probability expression (referred to as '$\bar{g}(\tau_0)$') was developed for an infinite plane parallel slab of homogeneous density

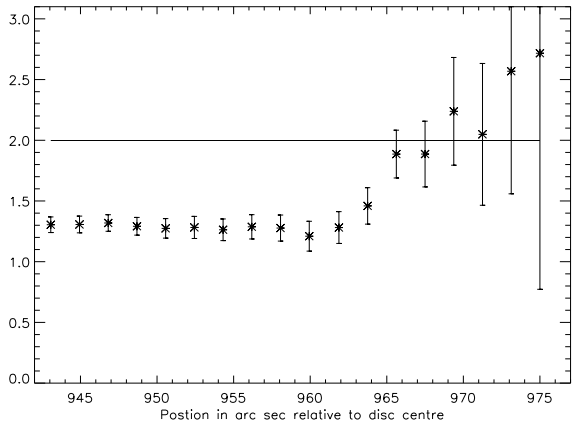

Figure 1.9: Plot of the C II $I(\frac{3}{2}-\frac{1}{2})/I(\frac{1}{2}-\frac{1}{2})$ line ratio . The solid line shows the optically thin flux ratio. The error bars reflect the uncertainty in the fitting of the two fluxes.

$$\bar{g}(\tau_0) = \frac{1}{\sqrt{\pi}} \int_{-\infty}^{\infty} \left[\frac{1 - e^{-\alpha_0 \Delta x e^{-u^2}}}{\alpha_0 \Delta x} \right] du \tag{1.49}$$

Thus the method of analysis was as follows: Using equation (1.46) the ratio of the two escape probabilities was deduced from the intensity ratio observation. Then using expression (1.49) the corresponding optical depth ($\alpha_0 \Delta x$) in one of the transitions was evaluated numerically. Equation (1.48) was then used to deduce the optical depth in the other line and this was extrapolated to infer the optical depths of all other C II transitions.

In order to measure the line integrated spectral flux in each of the C II lines we used the fitting procedure ADAS 602 (Summers, 2001). This fitting routine performs a maximum likelihood fit of Gaussian profiles to an observed spectrum and produces integrated fluxes, central wavelength positions with associated error estimates. The resultant flux ratio plot is shown in figure 1.9 - note that the straight line in this figure shows the theoretical optically thin ratio, given by the ratio of the two A-values. The displayed errors are given by the square root of the sum of the squares in the errors in the fluxes for each line.

The ratio $I(\frac{3}{2}-\frac{1}{2})/I(\frac{1}{2}-\frac{1}{2})$ deviates significantly from its optically thin value on disc and at the limb ($\approx$ 959 arc sec), returning to its thin value above the limb. Neither

Pos.(")	$\bar{g}_{3/2-1/2}$	$\tau_{0,3/2-1/2}$	Pos.(")	$\bar{g}_{3/2-1/2}$	$\tau_{0,3/2-1/2}$
943.06	0.31	5.30	959.94	0.18	10.2
944.94	0.31	5.25	961.88	0.28	6.00
946.81	0.32	4.95	963.75	0.46	2.82
948.69	0.29	5.70	965.63	0.88	0.36
950.56	0.27	6.23	967.50	0.88	0.36
952.44	0.28	6.00	969.38	-	-
954.31	0.26	6.70	971.25	-	-
956.19	0.29	5.80	973.13	-	-
958.06	0.27	6.20	975.00	-	-

Table 1.1: Summary of the data for the C II $2s^2 2p\ ^2P_{3/2} - 2s2p^2\ ^2S_{1/2}$ transition for each raster scan position.

line shows much limb brightening, indicating that they are both optically thick on disc. The $(3/2 - 1/2)$ line is expected to be more sensitive to changes in opacity as it has a greater oscillator strength and statistical weight and therefore an increased optical depth. On disc and at the limb this line experiences a bigger reduction in intensity and the intensity ratio is lower than its optically thin value. Above the limb the density of the plasma falls off and the fluxes (and hence the line ratios) should return to their optically thin values. This appears to be the case here, but further study indicates that scattered light, or unresolved fine structures beyond the limb, modifies this simple conclusion (Fischbacher, 2001). Using the method described above the optical depths in the $(3/2 - 1/2)$ line were evaluated at each scan position and are shown in table 1.1. In Brooks et al. (2000) the optical depths are extrapolated to classify the transitions in different C II lines and a similar study is also performed on other carbon multiplets.

This technique of determining the optical depths in all the lines of one ion from a single branching line ratio has provided us with a powerful characterisation of lines which are optically thin, and hence suitable for Differential Emission Measure (DEM) analysis. Alternatively, escape probabilities can be used to adjust observed intensities of optically thick lines, allowing them to be used in such a study. Thus it is possible

to diagnose optical depths in a moderately optically thick plasma from branching line ratio observations using escape probability techniques.

1.3.2 Low hydrogen series member opacity : Fusion divertor plasma

Consider next the case of hydrogen opacity in the fusion tokamak divertor region. The divertor (see figure 1.10) is situated below a null point in the tokamak poloidal magnetic field such that plasma impurities entering the scrape-off layer flow unimpeded to the target plates and are filtered out from the main body of the plasma. The plasma impurities and spent fuel experience collisions and possibly radiative cooling upon entry into the divertor reducing their energies and momenta. Thus when they encounter the divertor target plate strike points they are less effective in sputtering material back into the plasma core. The reverse flow in the divertor assists in constraining any ejected material and returning it towards the divertor, allowing it to be extracted by the cryopump. The divertor region is a low temperature ($\approx 1 \times 10^4 K$), high density ($\approx 1 \times 10^{13} cm^{-3}$) plasma where the electrons and ions may recombine and a high concentration of neutrals are present. The neutral presence is maintained by the recycling of hydrogen on the walls and by direct gas puffing into the divertor. Under these conditions and effective plasma dimensions, one might expect the lowest hydrogen Lyman lines to become optically thick, although the Balmer lines would certainly remain thin. Opacity in the L_β line has been observed in ASDEX-upgrade (Behringer, 1997) and in the JET divertor (Lachin, 1997). In JET it was found that there was significant line absorption in L_α but that it did not affect the ionisation balance or power loss. Wan et al (1995) used an escape factor approach to predict the effects of L_α absorption in projected ITER conditions, finding that opacity will have to be included in ionisation balance and power loss calculations.

The optically thin branching line ratio of L_β/H_α from equation (1.46) is 0.79. Observations taken from Behringer (1998) on the ASDEX-upgrade measured it to be about 4.0, indicating L_β opacity. An escape probability and absorption factor code has been developed by Behringer and translated into the ADAS code, ADAS 214. See

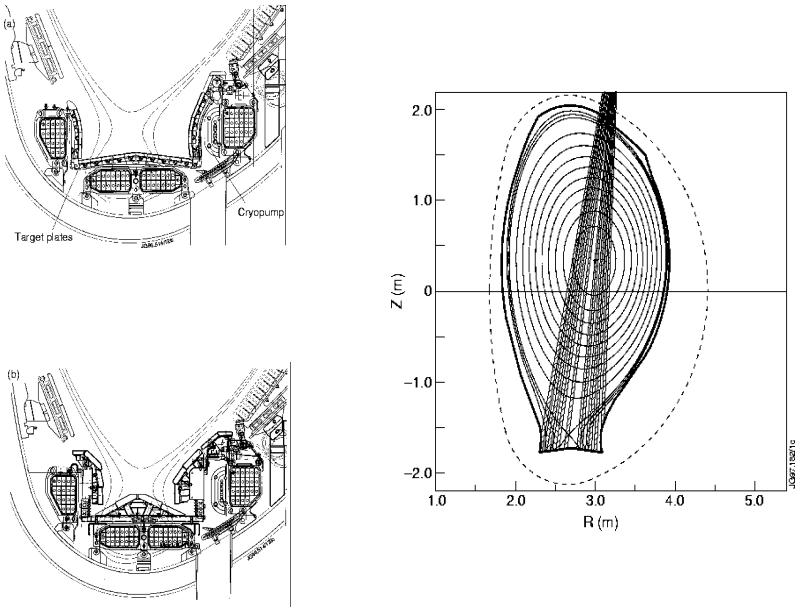

Figure 1.10: Schematic of JET tokamak divertor region showing the target plates and cryopump.

the code and theory description as given in Behringer (1998) and the description in chapter 2. The following example is taken from the Behringer's report and provides a useful illustration of the generic (i.e. scalable) application of absorption factors to account for opacity modifications to atomic population structure. The code was run for hydrogen emission in the divertor region with the following options: a voigt line profile was chosen with the Lorentz half width being 0.14 times the doppler half width (see Behringer (1998) for justification of this choice). A gas temperature of 23,010 K and an electron temperature of 11,605 K were selected. A cylindrical plasma geometry was chosen with an aspect ratio of 5. The effective length of the plasma was chosen to be 7.5 cm and the column density (=length $\times$ plasma density) varied from 2×10^{14} cm^{-2} to 1.2×10^{15} cm^{-2}. A parabolic decrease in the upper level density distribution was selected and the line ratios predicted. The results of the code are shown in figures 1.11 and 1.12.

In figure 1.11 the absorption factors evaluated at a column density of 1×10^{14} cm^{-2} are shown. The y-axis gives the absorption factor value while the x-axis shows the optical depth calculated for the various transitions. Note that the absorption factor

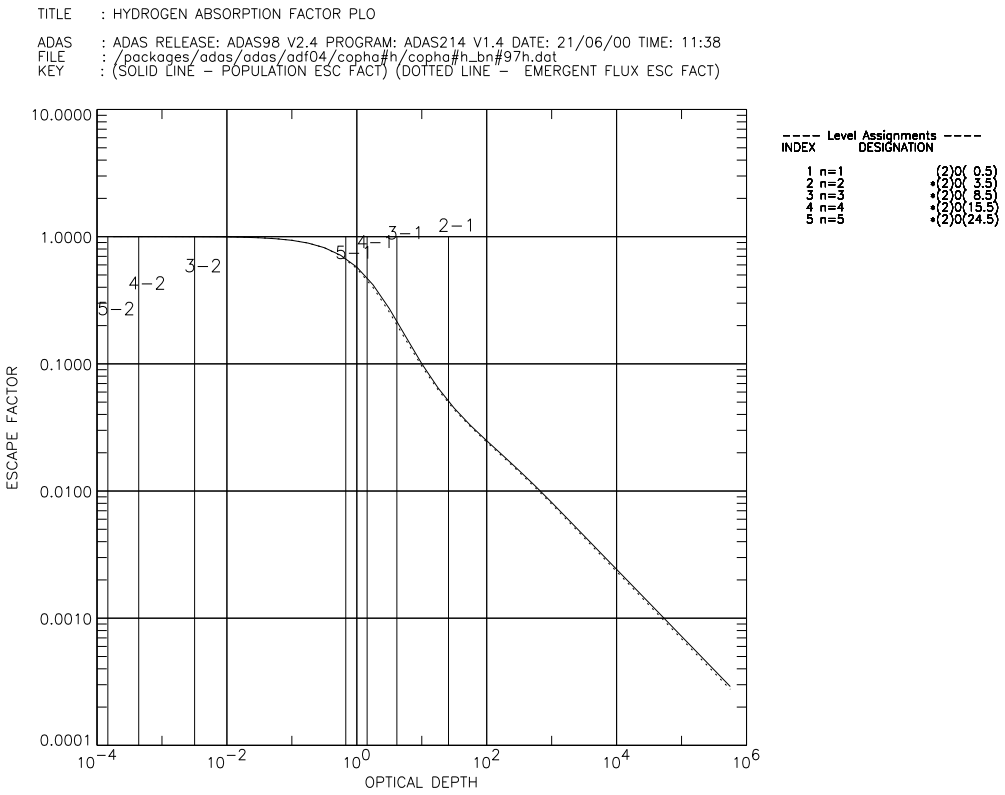

Figure 1.11: Absorption factor results for hydrogen from Behringer (1998) reproduced using ADAS 214. The index numbers labelling the vertical lines correspond to the principal quantum shell of the upper and lower states.

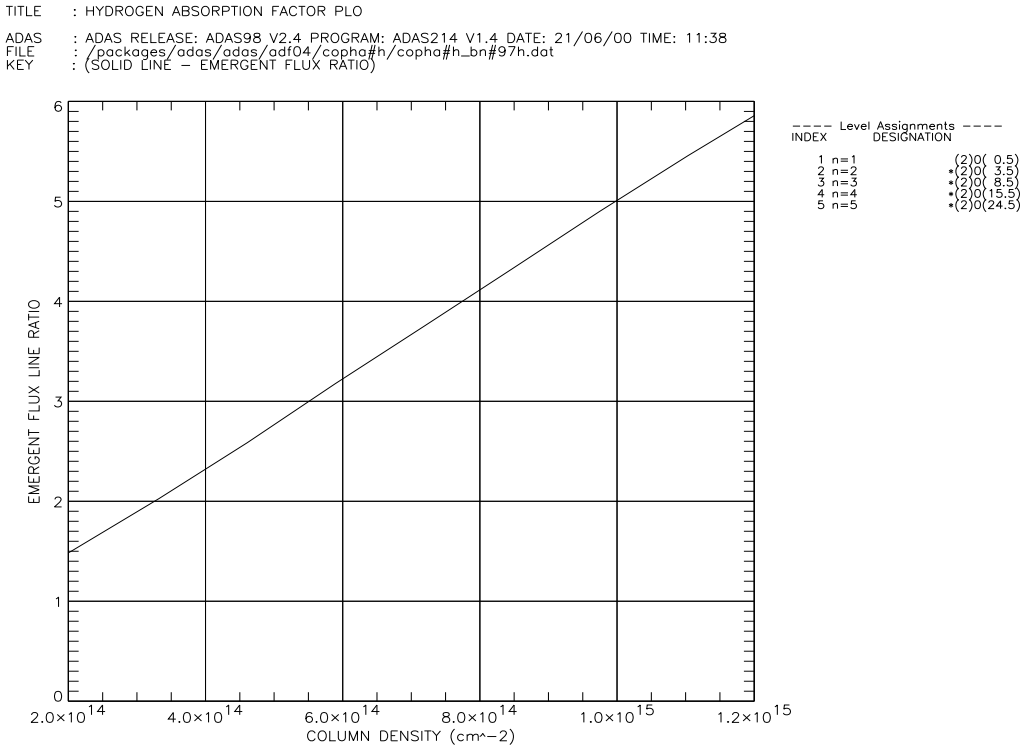

Figure 1.12: Opacity modified line ratio results from ADAS 214 for divertor conditions.

curve is represented by the solid line and the escape probability curve by the dotted line. A vertical line is drawn for the first few Lyman and Balmer transitions, and where these lines cut the absorption factor curve one can read off the absorption factor for that transition. All the Balmer lines have negligible absorption factors and escape probabilities, while the Lyman lines are moderately thick.

Figure 1.12 shows the predicted intensity line ratio of L_β/H_α as a function of column density. Optically thick population densities are used in this calculation by modifying the spontaneous emission coefficients in the collisional-radiative subroutine of ADAS 214 by the appropriate absorption factors. The escaping flux for each line is then modified by that line's escape probability and the optically thick line ratio found. It can be seen that the column density corresponding to the observed L_β/H_α line ratio of 4.0 is approximately $7.5 \times 10^{14}\ cm^{-2}$, which implies a neutral hydrogen density of $1.0 \times 10^{14}\ cm^{-3}$, broadly consistent with divertor conditions.

Using absorption factor techniques such as the one outlined here, opacity adjustments to moderately optically thick plasma population densities can be found.

1.3.3 High hydrogen series member opacity: Solar prominence Lyman lines, Lyman continuum and Balmer line radiation

Spectral observations of solar prominences show that they are optically thick in all Lyman lines through to the Lyman continuum. Figure 1.13 gives an $H\alpha$ image of a prominence and figure 1.14 an example of an optically thick Lyman series limit spectrum.

Solar prominences are large, dense, cool structures in the solar atmosphere, immersed in a background radiation field from the solar photosphere and chromosphere. Reviews can be found in Hirayama (1985), Zirker (1988), Preist (1989) and Tandberg-Hanssen (1995). See table 1.2 for typical physical values. They are stable on a timescale of weeks until they often erupt from the solar atmosphere. They are sometimes associated with Coronal Mass Ejections (CME's), though the nature of the association is unclear. There is much interest in solar prominences at the moment,

Figure 1.13: Solar prominence $H\alpha$ observation taken by the janitor of the Big Bear Solar observatory in 1970. Note the various characteristic prominence components, i.e. a large body of plasma suspended in the corona with a few footpoints rooted in the photosphere. On close inspection the vertical fillamentary internal structure of the prominence can be seen.

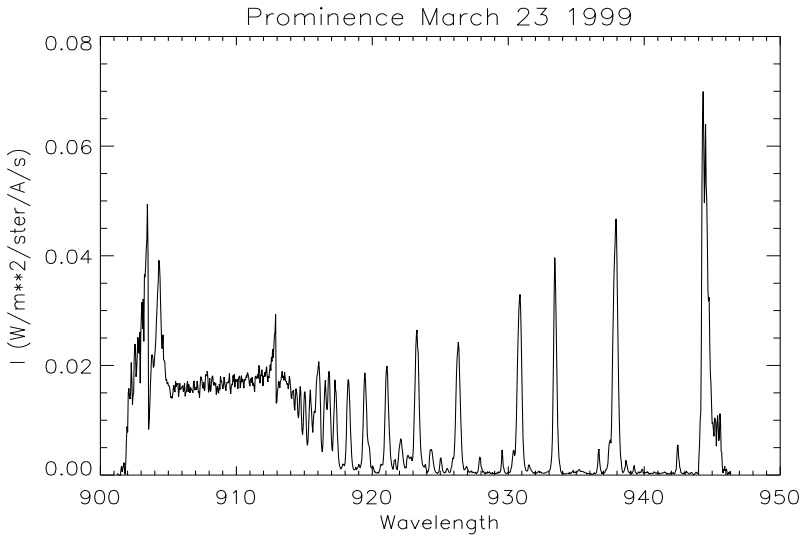

Figure 1.14: Lyman series limit observation of a solar prominence, taken from the data in Schmieder et al. (1999b). Note the merging of the high series lines into the continuum. Compare the heights of the last few observable lines with the gain in line heights as one progresses down the series. The small increase indicates that the lines are not reflecting optically thin conditions with Boltzmann upper level densities, but are being significantly reabsorbed.

Quantity	typical values
Electron density	$5 \times 10^{10} - 1 \times 10^{11} cm^{-3}$
Electron pressure	$0.1\ dyn\ cm^{-2}$
Temperature	$7,000K$
Gas pressure	$3 - 6\ dyn\ cm^{-2}$
Hydrogen density	$3 \times 10^{11}\ cm^{-3}$
Size	$100,000 - 600,000km$ long $5,000 - 10,000km$ thick $50,000km$ high
Ionisation degree of hydrogen	0.07

Table 1.2: Summary table of typical prominence physical properties.

in particular in explaining their support mechanism in the solar atmosphere and the trigger for their abrupt eruption, see Schmieder et al. (1998), Schmieder et al. (1999a), Schmieder et al. (1999b), Schmieder et al. (2000), Stellmacher & Wiehr (1994).

The optical thickness of the Lyman series is easily seen from an estimate of photon mean free paths (given by the reciprocal of the absorption coefficient), compare the mean free paths of table 1.3 with typical prominence dimensions. The Lyman series photons are heavily absorbed, with a mean free path of less than a centimeter, while the Balmer series photons have mean free paths of the same order as the dimension of the prominence. A consequence of this heavy absorption is the unusual energy balance for prominences, first found by Poland and Anzer (1971). It is likely that the main energy gain is due to Lyman continuum absorption, and that the main losses are due to Hα emission. Photo-absorption of Lyman lines is the dominant process in populating the excited states of the prominence hydrogen atoms. Similarly absorption of the Lyman continuum drives the ionisation balance of both hydrogen and helium atoms in the plasma.

The presence of opacity in all Lyman lines through to and including the continuum led to the development of the analytically continuous escape probability and absorption factor expressions shown in chapter 3. These expressions allow opacity to be dealt with as series limit lines merge together and blend into the continuum, thus providing

Transition	mean free path (m)
2-1	$1.41 \times 10^{-2} m$
3-1	$8.82 \times 10^{-2} m$
4-1	$0.25 \times 10^{0} m$
5-1	$0.54 \times 10^{0} m$
3-2	$9.42 \times 10^{4} m$
4-2	$6.84 \times 10^{5} m$
5-2	$2.04 \times 10^{6} m$
4-3	$2.56 \times 10^{5} m$
5-3	$2.09 \times 10^{6} m$
5-4	$1.62 \times 10^{5} m$

Table 1.3: Summary table of typical mean free paths of hydrogen photons in a solar prominence.

a means of analysing spectra such as the one shown in figure 1.14. However, the large optical depths of prominences puts them into a regime where a radiative transfer approach is more appropriate. There already exist low series member prominence radiative transfer codes (Heasley & Mihalas, 1976 and Gouttebroze et al., 1993). It has been demonstrated that a radiative transfer approach which allows for partial frequency redistribution (PRD) is necessary to match the observed low series member line profiles and to properly account for population modification (Gouttebroze et al., 1993). It may be possible to construct a valid high series escape factor code, as the higher populations will be close to Boltzmann values so the coupling of the equations (1.1) and (1.35) is not an issue. Also, partial frequency redistribution, which must be accounted for in the low series members, becomes less significant as one progresses up a series and complete frequency redistribution (CRD) can be assumed. It was decided that no diagnostic advantage would be achieved from developing such a code and that the code of chapter 3 should be retained for plasmas with more moderate optical depths.

The prominence observations raise one final issue. That is, there are plasmas for which the influence of a background radiation field on our escape and absorption factor expressions should be included. Normally the background radiation field term

in equation (1.8) and the background radiation field contribution to $u(\nu)$ in equation (1.14) are set to zero. It proves fairly straightforward to include such a background field in the theory development for the escape probability and absorption factor expressions. This was done and the initial steps in developing a corresponding code were performed, see section 2.10.

1.3.4 High series observations : Fusion divertor plasma

Although series limit prominence observations could not be modelled, there existed a need to interpret similar fusion divertor spectra. These types of series limit spectra were first analysed by Inglis & Teller (1939), where the smooth merging of high series lines into the continuum was shown and the point at which the merging occurred used as a density diagnostic. Recently more advanced models have been developed allowing series limits to be included in solar atmosphere codes (Dappen, et al., 1987), in atomic calculations for the IRON project (Seaton, 1990) and to interpret tokamak divertor spectra (Pigarov et al., 1998). Figure 1.15 shows an example of a Balmer series limit observed on the JET reactor, taken from Meigs et al. (1998).

As one progresses up a series, the spectral lines blend together and assignment of a photon to a particular upper level becomes ambiguous. The merged lines smoothly extend into the continuum, and it becomes difficult to define a sharp continuum edge. This adds uncertainty to electron temperature and density diagnostics which depend upon the continuum edge (such as those described in chapters 10 and 11 of Griem (1997)). A code was developed to predict a synthetic spectrum, referred to as a 'spectral feature', of sufficient quality that the fitting of this feature to JET divertor spectra could be used to diagnose plasma electron temperature, density and recombination state.

Comprehensive modelling of this region requires high quality line profiles for the high series members, the population modelling must be appropriate for high quantum shells and the smooth merging of high series lines into the continuum has to be accounted for. The conventional method of dealing with the series merging is to introduce a statistical microfield which progressively shifts the high quantum shells into the

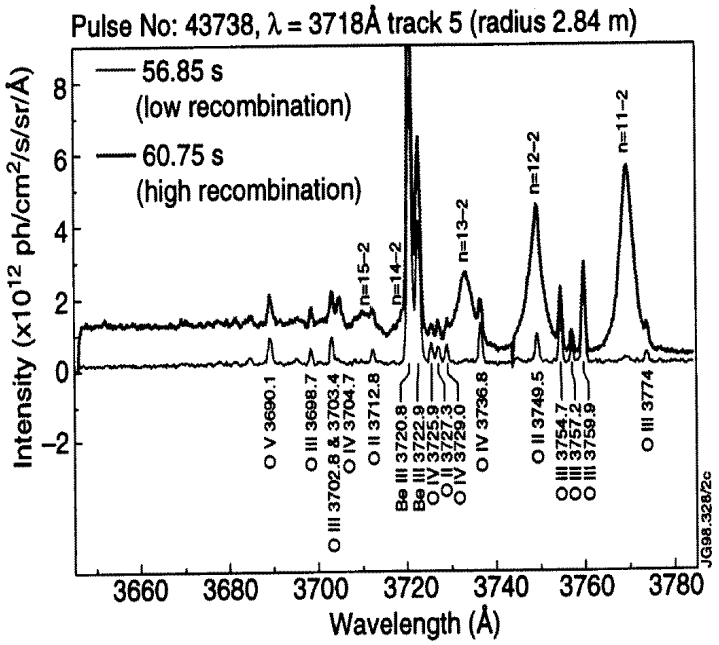

Figure 1.15: Balmer series limit observation of the JET divertor region, taken from Meigs et al. (1998).

continuum through field ionisation. That is, it is assumed that once an electron reaches a certain n-shell it is automatically ionised and thus behaves as if it is in the continuum. See Pigarov et al. (1998) for an example of this method used in practice to deal with series merging in the divertor of the Alcator C-Mod tokamak. This thesis takes an alternative approach, proving that bound-bound photo-rates continue analytically into the free states, with no need to 'dissolve' high quantum shells into the continuum. The microfield effects are accounted for in the line broadening calculations and it is intended that they will be included (as an extra rate, not as an ionising field) in future collisional-radiative work . The details of this alternative approach are presented in chapter 3 and a contrast with the conventional method given in section 3.3. It will be shown in section 5.3.3 that the JET divertor code can indeed fit observational data and diagnose local plasma parameters.

Chapter 2

Opacity modelling of low series members for population and emergent flux calculations : The escape probability and absorption factor approach

2.1 Introduction

This chapter describes the theory for modelling opacity in low series members using the escape factor approach, and its application as the code ADAS 214. Two quantities are evaluated, the escape probability (Θ) for emergent flux adjustments and the absorption factor (Λ) for population modifications, see equations (1.8) and (1.14) of chapter 1.

ADAS 214 is derivative of the work of Behringer who developed a code for the practical evaluation of (1.8) and (1.14). This chapter outlines the theory behind the new ADAS code, highlighting the various approximations which are made. The original Behringer code was used in the study of an air-like plasma jet (Jentschke, 1995), then amended and extended with a later version being used to account for opacity in low temperature

divertor plasmas (Behringer, 1997). The original code was written in BASIC for DOS, and later translated to Visual Basic for WINDOWS 95 by Behringer. The code was converted to run as an ADAS code, referred to as ADAS 214 (see Summers, 2001 and the original report of Behringer, 1998). ADAS 214 consists of an IDL graphical interface which spawns a fortran 77 code to evaluate the Λ and Θ expressions. Figure 2.1 shows the processing options screen where the plasma parameters are entered. The code also requires an input 'adf04' file containing all the A-values, collisional rates etc for the ion under consideration.
The code outputs an opacity modified version of this file, with the A-values adjusted by the appropriate absorption factors. This file can be used in collisional-radiative calculations to produce an optically thick population distribution. ADAS 214 has two main graphical outputs, it shows the generic Λ and Θ curves with selected transitions marked (as in figure 1.11) as well as plotting line ratios verses column density (as in figure 1.12).

2.2 Basic Theory

In the evaluation of Θ and Λ expressions, considerable simplification is possible with the assumption of certain geometries and spatial distribution of the emission coefficient. The geometries considered by the code are:

- Isotropic sphere of radius b.
- Plane parallel disk of thickness $2b$.
- Cylinder with radius b and length $2a$.

See figures 2.2 and 2.3 for the details of these geometries. The escape probability is evaluated on a line of sight through the centre of the sphere, along the central axis of the disk and perpendicular to the central axis of the cylinder. The absorption factor is evaluated at the centre of the sphere and at the midpoint of the central axis of both the disk and the cylinder (note that the absorption factor evaluated in the code is only valid at this point).

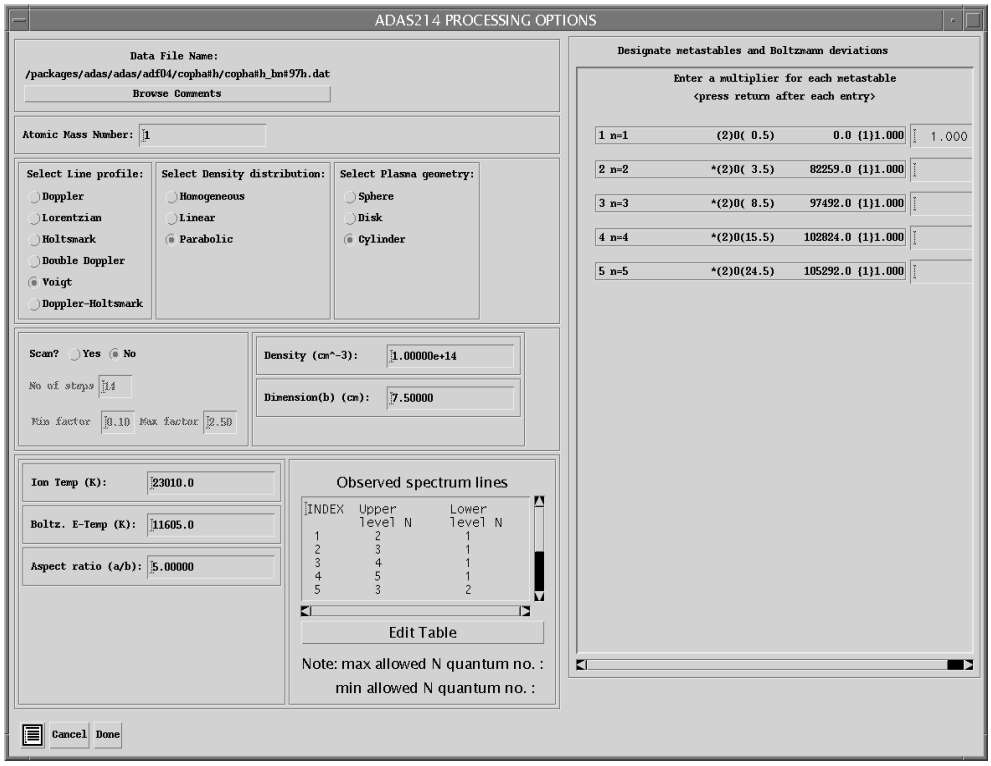

Figure 2.1: Example of the processing options screen in ADAS 214. Note the range of plasma parameters which need to be entered, in particular the Boltzmann deviation factor that it used in the initial population estimation.

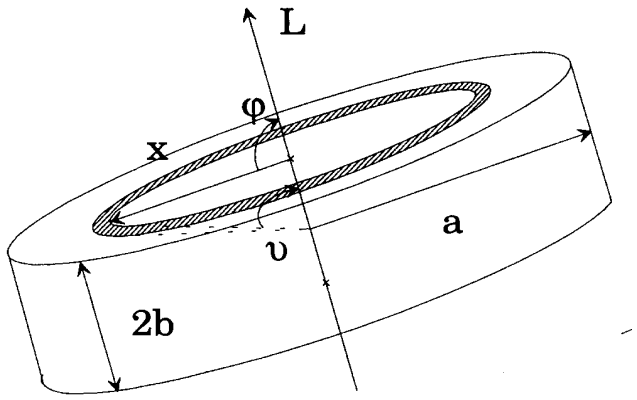

Figure 2.2: Schematics of the disk geometry considered by ADAS 214, taken from the report of Behringer (1998).

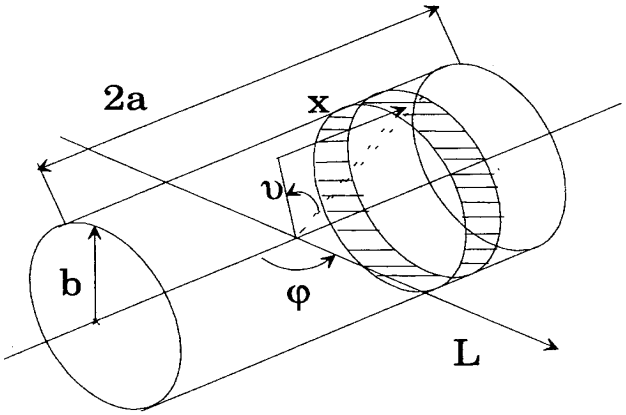

Figure 2.3: Schematics of the cylindrical geometry considered by ADAS 214, taken from the report of Behringer (1998).

Consider first the escape probability expression from chapter one:

$$\Theta = \frac{\int_{line}\int_0^{2b}\varepsilon(\nu,l)e^{-\int_l^{2b}\alpha(\nu,l')dl'}dld\nu + \int_{line}I(\nu,0)e^{-\int_0^{2b}\alpha(\nu,l)ldl}d\nu}{\int_{line}\int_0^{2b}\varepsilon(\nu,l)dld\nu} \tag{2.1}$$

Assume that there is no background radiation field ($I(\nu,0)=0$) and that α is independent of spatial position within the plasma and equal to $\bar{\alpha}(\nu)$. The assumption of constant absorption coefficient represents the main approximation in the code, equivalent to assuming a constant lower level population density throughout the plasma volume. This should be a reasonable approximation for fusion divertor conditions and for many low temperature plasmas. Opacity effects are commonly investigated in transitions with either the ground or metastables as their lower level. Because of the large populations of these levels it should be valid to assume that they are spatially invariant. The escape probability is then given by

$$\begin{aligned}\Theta &= \frac{\int_{line}\int_0^{2b}\varepsilon(\nu,l)e^{-\int_l^{2b}\bar{\alpha}(\nu)dl'}dld\nu}{\int_{line}\int_0^{2b}\varepsilon(\nu,l)dld\nu} \\ &= \frac{\int_{line}\int_0^{2b}\varepsilon(\nu,l)e^{(l-2b)\bar{\alpha}(\nu)}dld\nu}{\int_{line}\int_0^{2b}\varepsilon(\nu,l)dld\nu}\end{aligned} \tag{2.2}$$

Define $\varepsilon_L(l)$ such that emission coefficient can be written as

$$\begin{aligned} \varepsilon(\nu, l) &= \frac{1}{4\pi} A_{n' \to n} N_{n'}(l) \theta(\nu) \\ &= \varepsilon_L(l) \theta(\nu) \end{aligned} \tag{2.3}$$

and $\bar{\alpha_L}$ such that

$$\begin{aligned} \bar{\alpha}(\nu) &= N_n \frac{c^2}{8\pi} \left(\frac{n'}{n} \right)^2 \frac{1}{\nu^2_{n' \to n}} A_{n' \to n} \theta(\nu) \\ &= \bar{\alpha}_L \theta(\nu) \end{aligned} \tag{2.4}$$

Assuming that the emission and absorption line profiles are independent of position, the escape probability can be written as

$$\Theta = \frac{\int_0^{2b} \varepsilon_L(l) \int_{line} \theta(\nu) e^{(l-2b)\bar{\alpha_L}\theta(\nu)} d\nu dl}{\int_0^{2b} \varepsilon_L dl} \tag{2.5}$$

Consider next the absorption factor expression, starting with equation (1.14).

$$\Lambda(l) = 1 - \frac{\int_\Omega \int_{line} \alpha(\nu, l) u(\nu, l) d\nu d\Omega}{\int_\Omega \int_{line} \varepsilon(\nu, l) d\nu d\Omega} \tag{2.6}$$

Again, one assumes that the absorption coefficient is independent of l. For the purposes of the code Λ is evaluated at the centre of our plasma geometry, denoted by l=b. It is assumed that emission from this point is uniform in all directions (i.e. $\int_\Omega \int_{line} \varepsilon(\nu, l) d\nu d\Omega = 4\pi\varepsilon_L$. Thus

$$\Lambda(b) = 1 - \frac{\bar{\alpha_L} \int_\Omega \int_{line} \theta(\nu) u(\nu, b) d\nu d\Omega}{4\pi\varepsilon_L} \tag{2.7}$$

The radiation field term is given by

$$u(\nu) = \int_{h(\Omega)}^{b} \varepsilon_L(l) \theta(\nu) e^{(l-b)\bar{\alpha_L}\theta(\nu)} dl \tag{2.8}$$

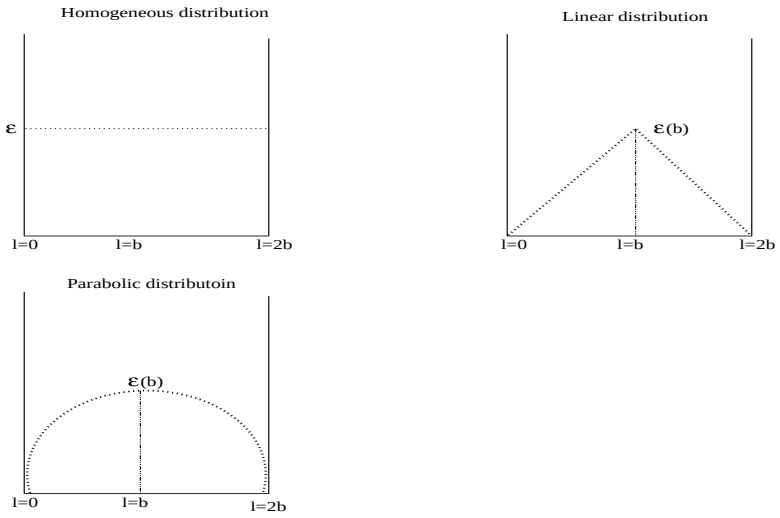

Figure 2.4: Diagrams of the spatial distribution of the emission coefficient as considered by ADAS 214.

with $h(\Omega)$ describing a point on the plasma surface. Thus the radiation field is the resultant radiation, incident from all possible lines of sight into the centre, accounting for attenuation along each line of sight.

Note that equation (2.8) is similar to the numerator of the equation (2.5), allowing one to significantly simplify the numerics of the calculation. As will be seen in the next section, the emergent flux along a given line of sight can be expressed purely as a function of optical depth. Thus $u(\nu)$ can be evaluated for a range of optical depths, used immediately to evaluate Θ and called repeatedly in the solid angle integration for Λ. Thus it is only necessary to work out the generic $u(\nu)$ vs τ curve once and the rest of the calculations can be performed from interpolation of these results.

2.3 Spatial variation in the emission coefficient

The code allows for various distributions in the emission coefficient within the volume of the plasma. These options are

- homogeneous distribution throughout the plasma.
- linear decrease from plasma centre to edge.
- parabolic decrease from plasma centre to edge.

Writing out the intensity expression and repeatedly integrating by parts results in

$$\begin{aligned} I(\nu,b) &= \int_0^b \varepsilon(\nu,l)e^{(l-b)\bar{\alpha}(\nu)}dl \\ &= \frac{\varepsilon(\nu,b)}{\bar{\alpha}(\nu)} - \frac{\varepsilon'(\nu,b)}{\bar{\alpha}(\nu)^2} + \frac{\varepsilon''(\nu,b)}{\bar{\alpha}(\nu)^3} - .... \\ &\quad -e^{-\bar{\alpha}(\nu)b}\left[\frac{\varepsilon(\nu,0)}{\bar{\alpha}(\nu)} - \frac{\varepsilon'(\nu,0)}{\bar{\alpha}(\nu)^2} + \frac{\varepsilon''(\nu,0)}{\bar{\alpha}(\nu)^3} - ....\right] \end{aligned} \tag{2.9}$$

The variation in the allowed emission coefficient distributions is at most second order making this technique an efficient way of evaluating the line of sight integration. When this expression is evaluated for each emission coefficient distribution, the following expressions are achieved (results with the integration extending from $0 \rightarrow 2b$ and from $0 \rightarrow b$ are shown since they are used in the calculation of Θ and Λ respectively): For the homogeneous distribution one has

$$\begin{aligned} \int_0^b \varepsilon(\nu,l)e^{(l-b)\bar{\alpha}(\nu)}dl &= \frac{\varepsilon(\nu)}{\bar{\alpha}(\nu)}\left[1-e^{\bar{\alpha}(\nu)b}\right] \\ \int_0^{2b} \varepsilon(\nu,l)e^{(l-2b)\bar{\alpha}(\nu)}dl &= \frac{\varepsilon(\nu)}{\bar{\alpha}(\nu)}\left[1-e^{2\bar{\alpha}(\nu)b}\right] \end{aligned} \tag{2.10}$$

For the linear distribution these become

$$\begin{aligned} \int_0^b \varepsilon(\nu,l)e^{(l-b)\bar{\alpha}(\nu)}dl &= \frac{\varepsilon(\nu,b)}{\bar{\alpha}(\nu)}\left[1-\frac{1}{\bar{\alpha}(\nu)b}+\frac{1}{\bar{\alpha}(\nu)b}e^{-\bar{\alpha}(\nu)b}\right] \\ \int_0^{2b} \varepsilon(\nu,l)e^{(l-2b)\bar{\alpha}(\nu)}dl &= \frac{\varepsilon(\nu,b)}{\bar{\alpha}(\nu)}\frac{1}{\bar{\alpha}(\nu)b}\left[1-2e^{-\bar{\alpha}(\nu)b}+e^{-2\bar{\alpha}(\nu)b}\right] \end{aligned} \tag{2.11}$$

and

$$\begin{aligned}\int_0^b \varepsilon(\nu,l)e^{(l-b)\bar{\alpha}(\nu)}dl &= \frac{\varepsilon(\nu,b)}{\bar{\alpha}(\nu)}\left[1-\frac{2}{\bar{\alpha}(\nu)^2b^2}+\left(\frac{2}{\bar{\alpha}(\nu)b}+\frac{2}{\bar{\alpha}(\nu)^2b^2}\right)e^{-\bar{\alpha}(\nu)b}\right]\\ \int_0^{2b} \varepsilon(\nu,l)e^{(l-2b)\bar{\alpha}(\nu)}dl &= \frac{\varepsilon(\nu,b)}{\bar{\alpha}(\nu)}\frac{1}{\bar{\alpha}(\nu)b}\left[2-\frac{2}{\bar{\alpha}(\nu)b}+\left(2+\frac{2}{\bar{\alpha}(\nu)b}\right)e^{-2\bar{\alpha}(\nu)b}\right] \quad (2.12)\end{aligned}$$

for the parabolic distribution. This results in escape and absorption factor expressions of

$$\begin{aligned}\Theta &= \int_{line}\frac{\theta(\nu)[1-e^{-2\bar{\alpha}(\nu)b}]}{2\bar{\alpha}(\nu)b}d\nu\\ &= \int_{line}\frac{\theta(\nu)[1-e^{-2\tau(\nu)}]}{2\tau(\nu)}d\nu\\ \Lambda(b) &= \frac{1}{4\pi}\int_\Omega\int_{line}\theta(\nu)e^{-\bar{\alpha}(\nu)b(\Omega)}d\nu d\Omega\\ &= \frac{1}{4\pi}\int_\Omega\int_{line}\theta(\nu)e^{-\tau(\nu,\Omega)}d\nu d\Omega \quad (2.13)\end{aligned}$$

for the homogeneous distribution.

$$\begin{aligned}\Theta &= 2\int_{line}\frac{1}{\bar{\alpha}(\nu)b}\theta(\nu)\frac{1}{\bar{\alpha}(\nu)b}\left[1-2e^{-\bar{\alpha}(\nu)b}+e^{-2\bar{\alpha}(\nu)b}\right]d\nu\\ &= 2\int_{line}\frac{1}{\tau(\nu)}\theta(\nu)\frac{1}{\tau(\nu)}\left[1-2e^{-\tau(\nu)}+e^{-2\tau(\nu)}\right]d\nu\\ \Lambda(b) &= \frac{1}{4\pi}\int_\Omega\int_{line}\left[\frac{1}{\bar{\alpha_L}b(\Omega)}-\frac{1}{\bar{\alpha_L}b(\Omega)}e^{-\bar{\alpha}(\nu)b(\Omega)}\right]d\nu d\Omega\\ &= \frac{1}{4\pi}\int_\Omega\int_{line}\left[\frac{\theta(\nu)}{\tau(\nu,\Omega)}-\frac{\theta(\nu)}{\tau(\nu,\Omega)}e^{-\tau(\nu,\Omega)}\right]d\nu d\Omega \quad (2.14)\end{aligned}$$

for the linear distribution and

$$\Theta = \frac{3}{4}\int_{line}\left[\frac{1}{\bar{\alpha}(\nu)b}\theta(\nu)\frac{1}{\bar{\alpha}(\nu)b}\left[2-\frac{2}{\bar{\alpha}(\nu)b}+\left[2+\frac{2}{\bar{\alpha}(\nu)b}\right]e^{-2\bar{\alpha}(\nu)b}\right]\right]d\nu$$

$$= \frac{3}{4}\int_{line}\left[\frac{1}{\tau(\nu)}\theta(\nu)\frac{1}{\tau(\nu)}\left[2-\frac{2}{\tau(\nu)}+\left[2+\frac{2}{\tau(\nu)}\right]e^{-2\tau(\nu)}\right]\right]d\nu$$

$$\Lambda(b) = \frac{1}{2\pi}\int_{\Omega}\int_{line}\left[\frac{2}{(\bar{\alpha}(\nu)b(\Omega))(\bar{\alpha}b(\Omega))}-\left[\frac{2}{\bar{\alpha_L}b(\Omega)}+\frac{2}{(\bar{\alpha}(\nu)b(\Omega))(\bar{\alpha_L}b)(\Omega)}\right]e^{-\bar{\alpha}(\nu)b(\Omega)}\right]d\nu d\Omega$$

$$= \frac{1}{2\pi}\int_{\Omega}\int_{line}\left[\frac{2\theta(\nu)}{(\tau(\nu,\Omega))^2}-\left[\frac{2\theta(\nu,\Omega)}{\tau(\nu,\Omega)}+\frac{2\theta(\nu)}{(\tau(\nu,\Omega))^2}\right]e^{-\tau(\nu,\Omega)}\right]d\nu d\Omega \quad (2.15)$$

for the parabolic distribution. Each of these expressions are functions of optical depth ($\bar{\alpha}_L b$) and line profile, allowing generic Θ and Λ vs τ curves to be evaluated, see figure 2.5.

2.4 Proof that generic $\Lambda(b)$ and Θ vs optical depth curves are valid

The code evaluates the escape and absorption factor expression as generic curves that are only functions of optical depth. The optical depth for each possible transition is then worked out and its corresponding escape and absorption factor found by interpolation of the generic curve. Thus the generic curve is assumed to be valid for every possible transition within the one ion. It is not immediately obvious that this approach is valid. There are two issues to be dealt with, firstly can the expression always be written in terms of optical depth and secondly how does one account for the fact that different transitions can have different line profiles?

To show that the expressions can always be written in terms of optical depth consider the following argument: By inspection from equations (2.10) - (2.15) it can be seen that Θ and Λ can be written in terms of optical depth and line profile. It can be shown that this is generally the case if one writes the emission coefficient with the spatial variation extracted, that is $\varepsilon(\nu,l) = \varepsilon(\nu,b)f(l)$ where $f(l)$ defines the variation of ε along l. It has been shown in equations (2.10) - (2.15) that the line integrated flux can be written as $\frac{\varepsilon(\nu,b)}{\bar{\alpha}(\nu)}g(\tau(\nu),\theta(\nu))$ where g is the appropriate function from these equations. The escape and absorption factors can then be written.

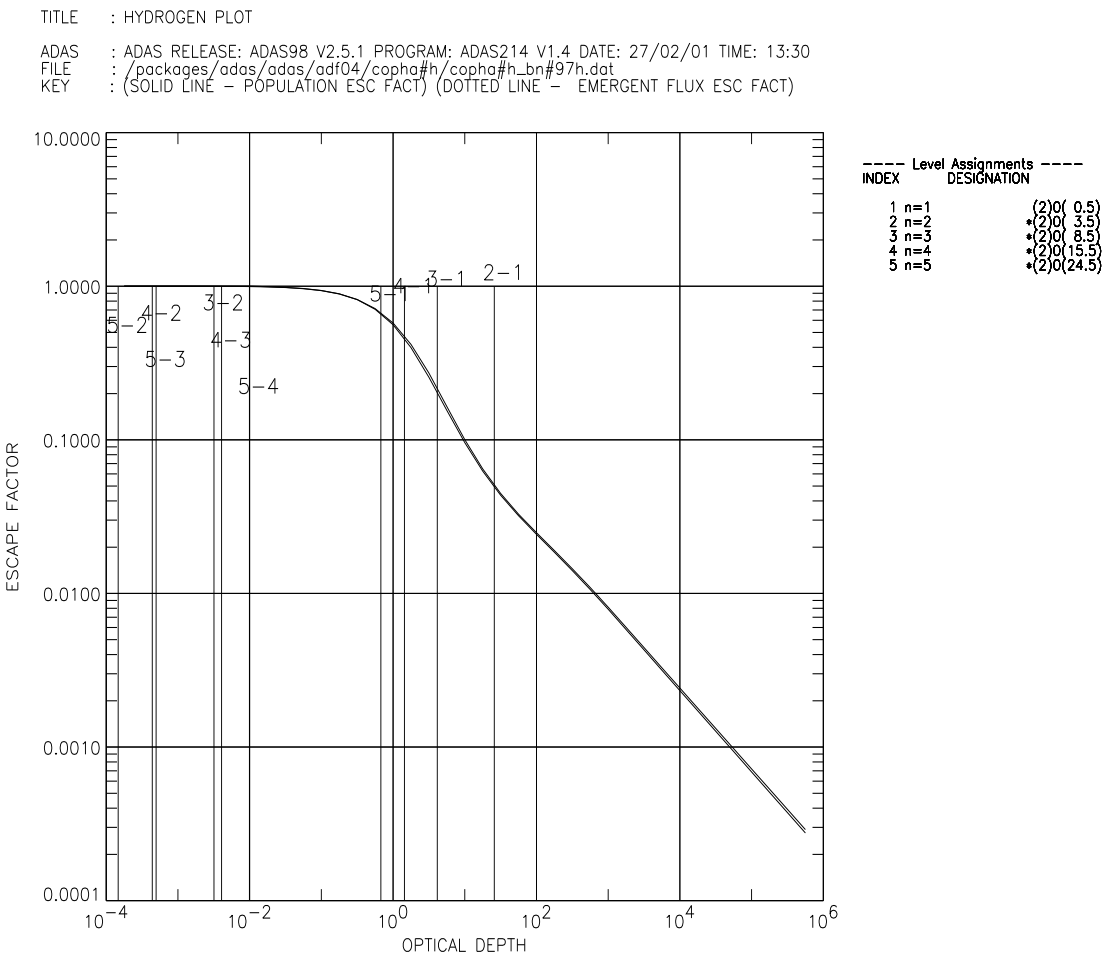

Figure 2.5: Example of the generic Θ and Λ curves produced by ADAS 214. Note that as one progresses up a given series the Θ and Λ values increase. The Θ and Λ values also increase from one series to the next

$$
\begin{aligned}
\Theta &= \frac{\int_0^b \int_{line} \varepsilon(\nu,l) e^{(l-b)\alpha(\bar{\nu})} d\nu dl}{\int_0^b \int_{line} \varepsilon(\nu,l) d\nu dl} \\
&= \frac{\int_0^b f(l) \int_{line} \varepsilon(\nu,b) e^{(l-b)\alpha(\bar{\nu})} d\nu dl}{\int_0^b f(l) dl \int_{line} \varepsilon(\nu,b) d\nu dl} \\
&= \frac{\int_0^b f(l) \int_{line} \frac{\varepsilon(\nu,b)}{\bar{\alpha}(\nu)} g(\tau(\nu),\theta(\nu)) d\nu dl}{\int_0^b f(l) dl \int_{line} \varepsilon_L(b)\theta(\nu) d\nu dl} \\
&= \frac{\varepsilon_L(b) \int_0^b f(l) \int_{line} \frac{\theta(\nu)}{\bar{\alpha}(\nu)} g(\tau(\nu),\theta(\nu)) d\nu dl}{\varepsilon_L(b) \int_0^b f(l) dl \int_{line} \theta(\nu) d\nu dl} \\
&= \frac{\int_0^b f(l) \int_{line} \frac{1}{\bar{\alpha_L}} g(\tau(\nu),\theta(\nu)) d\nu dl}{\int_0^b f(l) dl} \qquad (2.16)
\end{aligned}
$$

$$
\begin{aligned}
\Lambda(b) &= 1 - \frac{\int_\Omega \int_{line} \bar{\alpha}(\nu) u(\nu,b) d\nu d\Omega}{\int_\Omega \int_{line} \varepsilon(\nu,b) d\nu d\Omega} \\
&= 1 - \frac{\int_\Omega \int_{line} \bar{\alpha}(\nu) \frac{\varepsilon(\nu,b)}{\bar{\alpha}(\nu)} g(\tau(\nu,\Omega),\theta(\nu)) d\nu d\Omega}{\int_\Omega \int_{line} \varepsilon_L(b)\theta(\nu) d\nu d\Omega} \\
&= 1 - \frac{\varepsilon_L(b) \int_\Omega \int_{line} \theta(\nu) g(\tau(\nu,\Omega),\theta(\nu)) d\nu d\Omega}{\varepsilon_L(b) 4\pi} \\
&= \frac{\int_\Omega \int_{line} \theta(\nu) g(\tau(\nu,\Omega),\theta(\nu)) d\nu d\Omega}{4\pi} \qquad (2.17)
\end{aligned}
$$

Thus, for a given line profile, one can generate generic Θ and Λ vs optical depth curves. It should be noted that for both Θ and Λ a normalised line profile is used with the actual line height contained in the ε_L term. Provided that the same normalised profile holds for all transitions, the generic Θ and Λ vs τ curve will hold for each transition. This is likely to be the case as it is mainly adjacent series members with either the ground or a metastable as the lower level that are optically thick. The same broadening mechanisms are likely to apply to such lines giving them similar profiles. The higher series transitions, which are more likely to have different profiles,

are often optically thin, but even if they are not thin they have little effect on the population results of the code.

2.5 Profile Theory

Dealing next with the various line profile options, there are three basic profiles, and three convolved profiles allowed for in the code, namely

- Doppler
- Lorentzian
- Holtsmark
- Voigt
- Doppler-Holtsmark
- Double Doppler

Normalised profiles are generated numerically in the code from expressions such as those in section 1.2.5. The Doppler half-widths are determined from expression (1.26), the Lorentzian and Holtsmark widths are set to half the Doppler width and for the convolved profiles, the non-Doppler width is entered by the user.
The integration over the wavelength is performed numerically, at this point the escape probability can be found from expression (2.5).

2.6 Evaluation of Λ

To evaluate the absorption factor, it is necessary to integrate over solid angle, so knowledge of the plasma geometry is required. This integration is performed numerically. For the spherical geometry Λ can be returned immediately with the solid angle integration introducing a factor of 4π. For the cylinder and disk geometries the

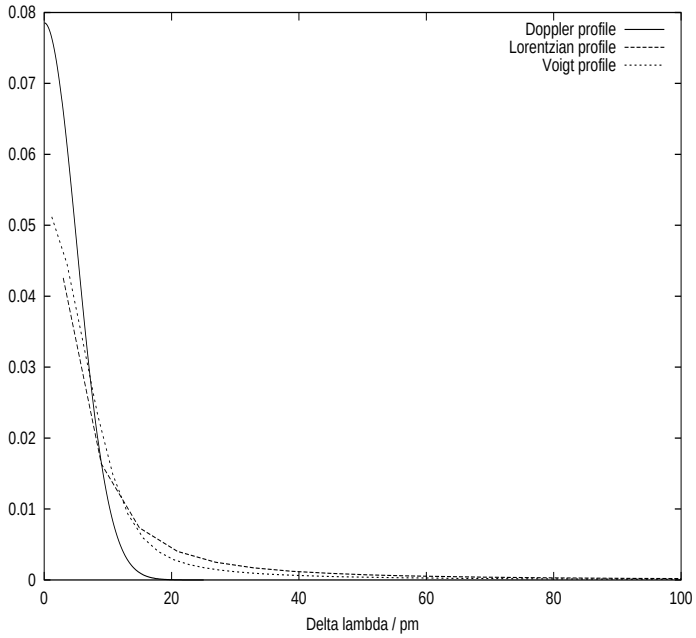

Figure 2.6: Example of various hydrogen profiles as calculated by ADAS 214. Note that all profiles are normalised and evaluated for the same set of plasma parameters. The Lorentzian width is set to half the doppler width as is the Lorentzian component of the voigt profile.

symmetry of the problem is exploited in that it is only necessary to evaluate the contribution from one strip. An element of surface area is considered along a given strip and its contribution to the radiation field at b evaluated. The contribution from each element along the strip is then worked out, with an end correction used to account for the flat ends of both geometries.

2.7 Computation of populations using absorption factors

The main purpose of the code is to allow opacity modified population distributions to be evaluated within ADAS collisional-radiative codes. These codes assemble all the collisional, radiative and spontaneous rates between atomic levels, and then solve the system to predict a population structure. The individual rates are either evaluated from algebraic expressions or taken from the best available observational/calculated

data. One type of input datafile is known as an adf04 file, these optically thin datafiles can be converted to account for opacity effects using ADAS 214. This is done automatically in the code, each transition being read in from the input file, its A-value modified by the appropriate Λ and written to the output 'optically thick' adf04 file. All of the existing ADAS codes assume that the plasma is optically thin, thus the absorption factor technique of modifying the Einstein A-values with Λ factors is ideal in that it allows the 'optically thin' collisional-radiative codes to process opacity modified adf04 files and generate a thick population structure.

2.8 Using the code as a line ratio diagnostic

ADAS 214 has an extension from the original code which allows the user to specify a range of column densities for which to run the absorption factor calculation. The code then evaluates absorption factors for each column density, producing corresponding adf04 files and opacity modified population distributions (via ADAS 214's own statistical balance subroutine). It is then a small matter to look up the escape probability expression at each column density for two chosen transitions and use equation (1.46) to work out the opacity modified line ratio. Thus one can evaluate any given emergent flux line ratio as a function of column density. See figure 2.7 for an example of this. The modified populations which are evaluated are for one point in the plasma and it is assumed that they remain constant along the line of sight. This is not entirely consistent with the selection of a modified upper level density distribution in the absorption factor calculation. That is, the upper level population modification is taken into account in the evaluation of Λ and Θ, but not in the $N_{n'}$ used in the emergent flux calculation. Within this limitation the line ratio option of the code can provide an estimate of any given ratio for immediate comparison with observational data. Alternatively the user can evaluate the modified population density along the line of sight themselves and perform the integrated flux and hence line ratio calculation themselves.

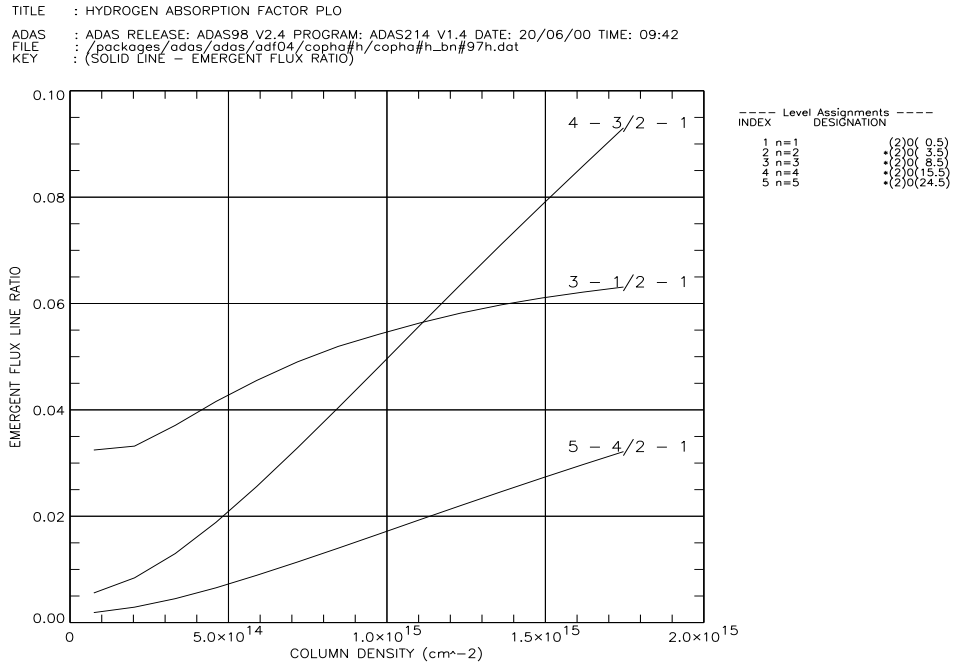

Figure 2.7: Example of the emergent flux line ratio evaluation vs column density from ADAS 214. The ratios are evaluated for hydrogen with the indexes corresponding to upper and lower principal quantum numbers. The plasma parameters are those from the fusion divertor study of section 1.3.2

2.9 Example of the use of the code for He line identification using CDS quiet sun observations

A useful illustration of ADAS 214 is found in part of the spectral line identification work of Brooks et al. (1999). In this study the Coronal Diagnostic Spectrometer (CDS) instrument onboard the SOHO spacecraft was used to obtain a complete spectrum of the quiet sun using the instrument's full wavelength range ($308-381\mathring{A}$, $513-633\mathring{A}$), the aim being to identify as many spectral lines as possible. An example of an observed spectral region is shown in figure 2.8 with some of the line identifications marked. Strict criteria were used in the identification of the lines. Firstly wavelength coincidence with accepted values was considered, and for lines where this coincidence was good, 'position patterns' could be used to confirm an identification. These position patterns refer to a technique first introduced in the analysis of data for the Spacelab 2 CHASE experiment in Lang, Mason & McWhirter (1990) and elaborated in Brooks et al. (1999). Spectra were taken over a range of spatial and temporal points and assigned a unique position index. Thus the different observations reflect typical quiet sun variabilities in density, temperature, structure. Each spectral line is then reduced to a single value by taking its intensity in counts divided by its average over all positions. These points are then plotted logarithmically against position index. When the position patterns for identified lines are arranged in order of similar patterns, and labelled with the ions temperature (from the peak of its $G(T_e)$), it is found that there are similar patterns for lines emitted by the same ion and for lines from ions formed at approximately the same temperature. Thus the position patterns of unidentified lines can act as a fingerprint indicating the probable temperature of formation of the line, thus aiding in its identification. It was sometimes possible to use line intensity ratios to judge whether or not lines originated from the same emitting ion and in this way further confirm certain identifications. A brief description is presented below on the use of ADAS 214 in aiding in the identification of four He I lines.

From wavelength coincidence and the similarities of their position plots, it was strongly suspected that four observed lines were

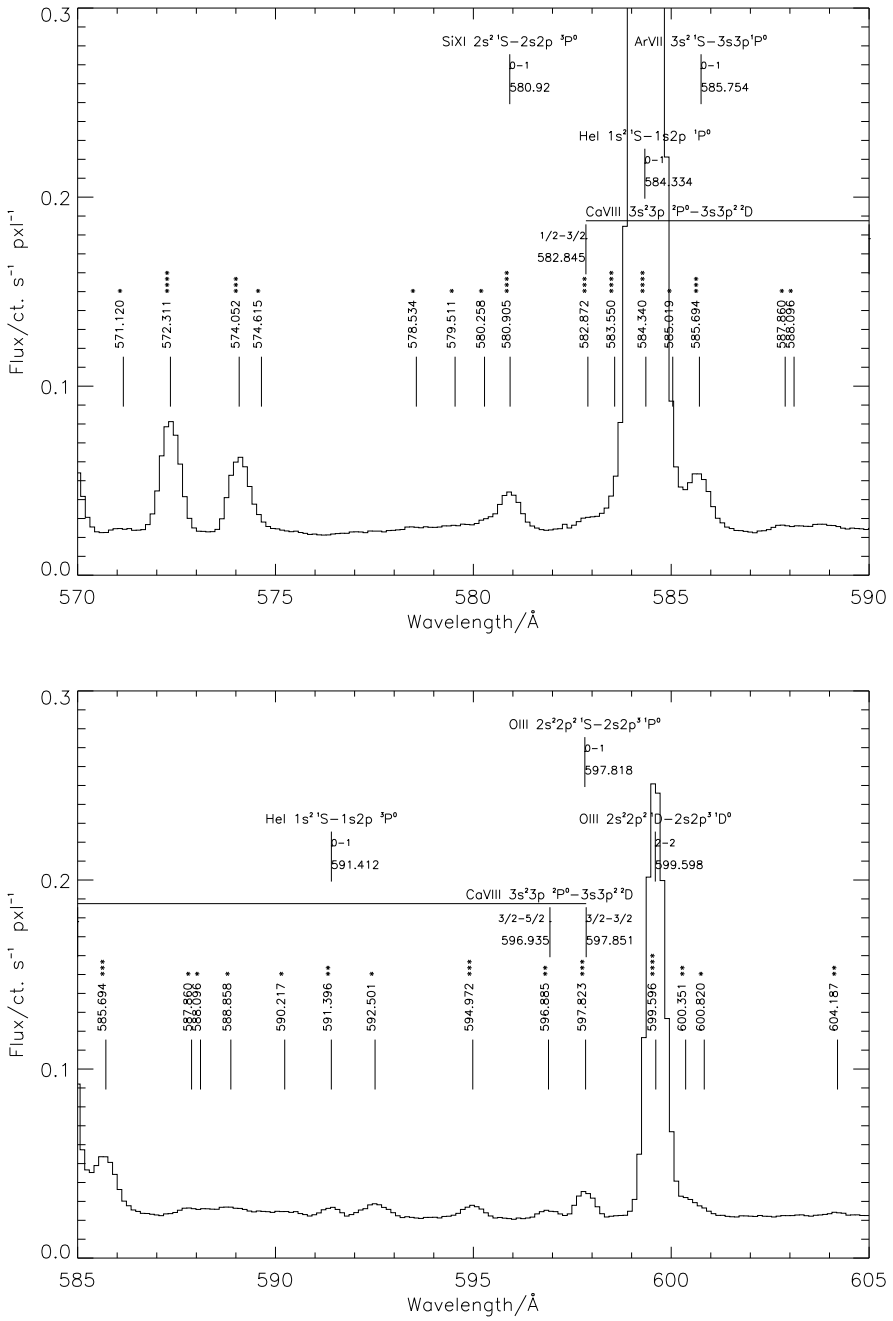

Figure 2.8: Example of the observed CDS spectrum used in the line identification work, taken from Brooks et al. (1999).

- He I $1s^2\ ^1S_0 - 1s4p\ ^1P_1$ 522.257$\mathring{A}$
- He I $1s^2\ ^1S_0 - 1s3p\ ^1P_1$ 537.091$\mathring{A}$
- He I $1s^2\ ^1S_0 - 1s2p\ ^1P_1$ 584.360$\mathring{A}$
- He I $1s^2\ ^1S_0 - 1s2p\ ^3P_1$ 591.411$\mathring{A}$

The 522, 537, and 584 lines were all strong and there was no doubt about their identification (see figure 2.8 upper plot for the 584 line), in fact these lines were used as calibration lines in the study. The 591 intercombination line on the other hand was very weak (see figure 2.8 lower plot) and evidence of the consistency of the observed intensities was needed for a definite identification. The observed line intensity ratios of each line to the 584 line intensity are shown in column two of table 2.1. Also shown is the predicted optically thin intensity ratio (column three) where the populations were evaluated from ADAS. It can be seen that the observed $I(537)/I(584)$ and $I(522)/I(584)$ ratios lie close to their optically thin values, while the $I(591)/I(584)$ ratio significantly deviates from it. It would be expected that the strong lines (584, 537 and 522) would be optically thick and so have a reduced emergent flux from the sun. If they have similar opacities they may experience similar intensity reductions, moving their ratios back to the expected thin values.

To see if opacity could explain the deviation of the $I(591)/I(584)$ ratio from that observed, ADAS 214 was used to return opacity and line ratio estimates. A disk geometry was chosen with a large aspect ratio to simulate a near infinite slab for the solar atmosphere. Doppler profiles were used along with a homogeneous density distribution, with the temperature being taken as $28,000K$ from the peak of the $G(T_e)$ function, see figure 2.9. A helium density of $1 \times 10^{10} cm^{-3}$ was taken from the corresponding value in the Vernazza et al (1981) solar atmosphere model, assuming that the helium density to be ten percent of the hydrogen density. The length of the slab was judged approximately from the height from the photosphere to the transition region, again taken from the Vernazza model. The input adf04 file was generated using the autostructure code via the ADAS 701 interface. An A-value for the intercombination line of $0.6s^{-1}$ was taken from Summers (1977).

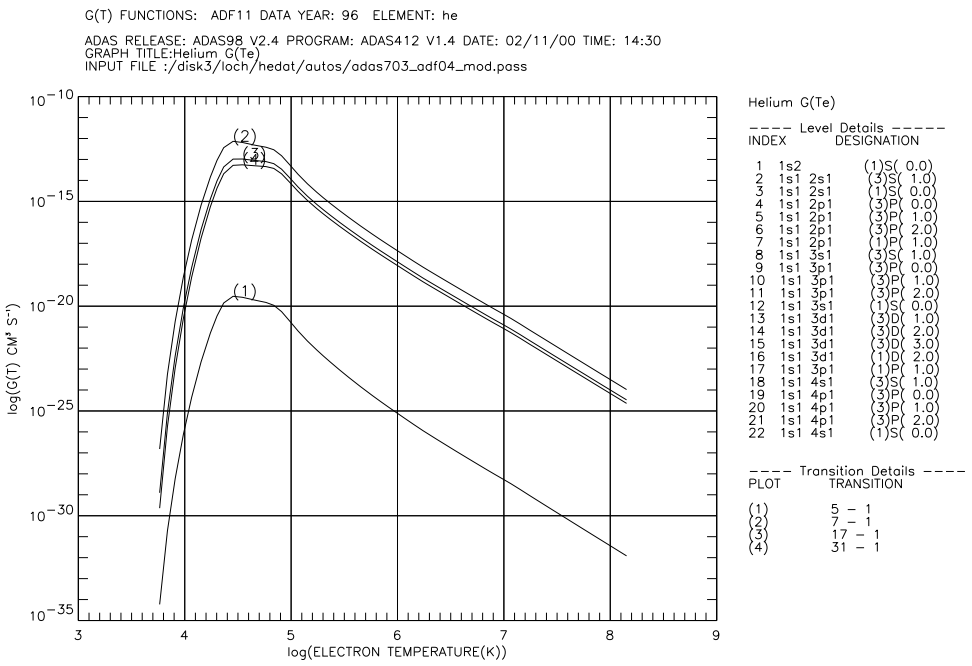

Figure 2.9: $G(T_e)$ function for helium evaluated using ADAS 412; note that the peak of the $G(T_e)$ lies at about $28,000K$.

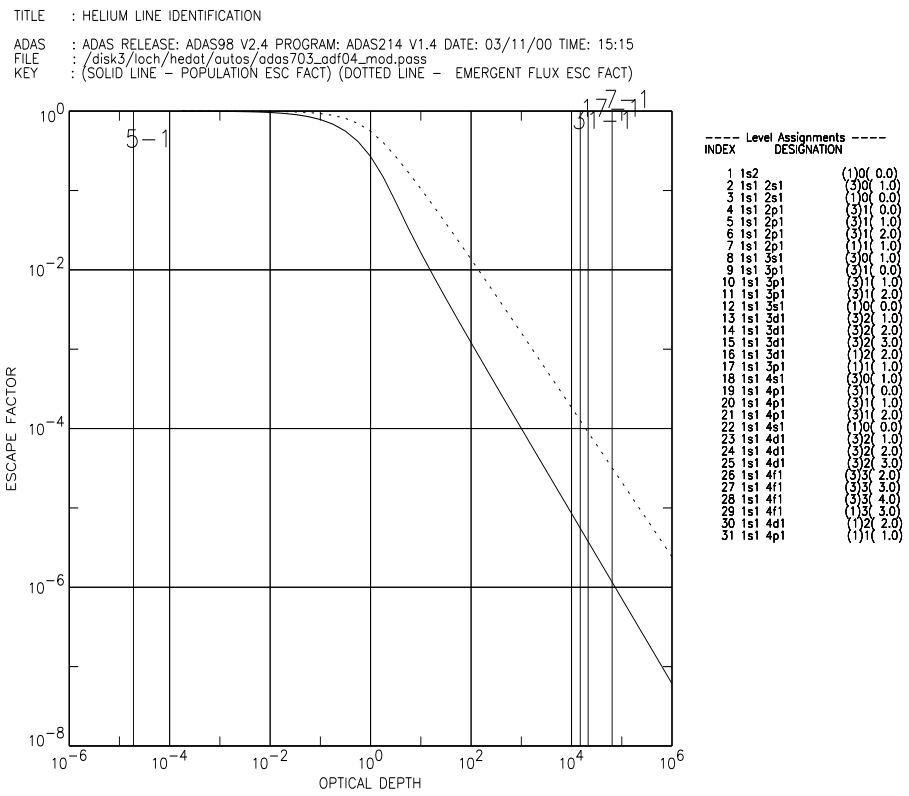

Figure 2.10: Escape factor plot generated using ADAS 214 for the helium line identification work.

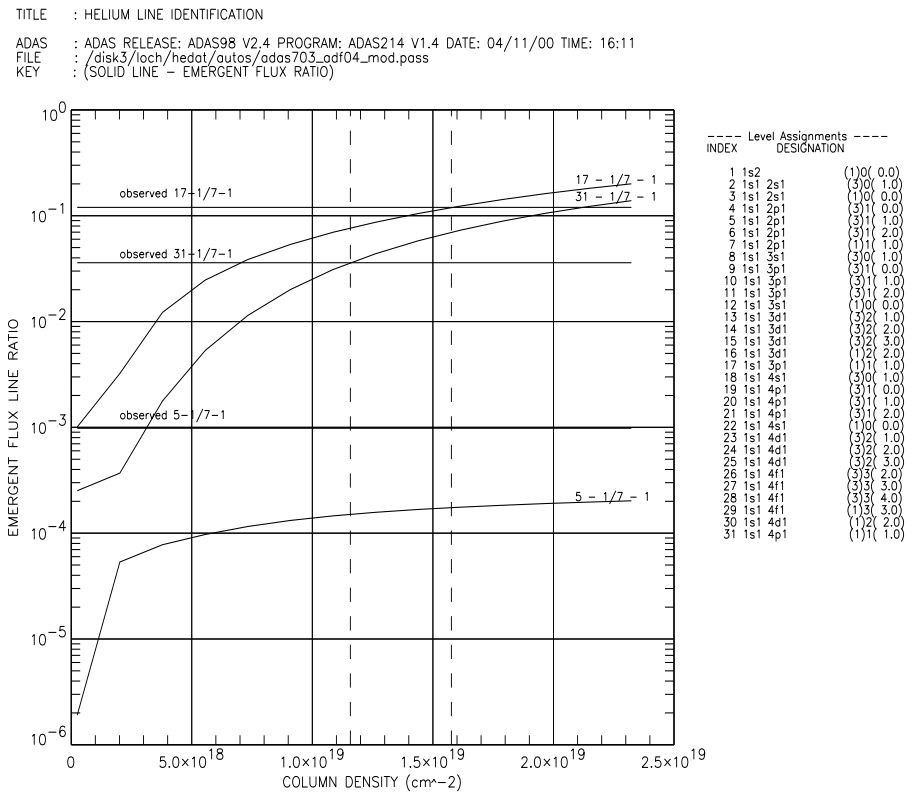

Figure 2.11: Line ratio plot generated using ADAS 214 for the helium line identification work.

Using these values an escape factor calculation was performed. The results are shown in figures 2.10 and 2.11. The 584, 537 and 522 lines are clearly extremely optically thick. Note that they have similar opacities, thus their ratios should be close to the optically thin values (i.e. their intensities scale similarly with optical depth so their ratios can still remain close to the optically thin ratio, even though the individual lines are optically thick). The 591 line on the other hand can be seen to be optically thin, and so the observed deviation from the thin line is to be expected. So a quick assessment of the escape probabilities using ADAS 214 has qualitatively explained the observed ratios.

The intensity ratios were then estimated - note that a ratio analysis like this is not the main purpose of the code, since the evaluated absorption factor is only valid at the centre of the geometry under investigation and the ratio evaluation assumes that it is valid for the whole line of sight. Despite this it was useful to estimate the ratios within the bounds of the code to get an indication of their behaviour. A range of column densities surrounding the value for which figure 2.10 was generated were chosen and the ratios produced. The results are shown in figure 2.11. Note that both the $I(537)/I(584)$ and $I(522)/I(584)$ cross their observed values at approximately the same column density ($\approx 1.3 \times 10^{19} cm^{-2}$). The $I(591)/I(584)$ on the other hand does not reach its observed value, always lying below it. This is not unexpected as we are running the code in the regime beyond which it is normally valid. The predicted $I(591)/I(584)$ ratio is too low, indicating that we have overestimated the I(584) intensity. As a result of this analysis it was decided to run the MULTI radiative transfer stellar atmosphere code (Carlson, 1986) to predict the line ratios. This approach is more likely to give a better estimate of the line ratios than ADAS 214 as it uses a solar atmosphere model based geometry and density distribution (in the case here the model of Vernazza et al., 1981). MULTI was run and line ratios produced - see column four of table 2.1. As can be seen from the table the predicted ratios are good for both the $I(537)/I(584)$ and $I(522)/I(584)$ ratios. The optically thick model matches the $I(591)/I(584)$ ratio better than the thin model, though it is still a little low.

As a result of this analysis the line was positively identified as $HeI\ 1s^2\ ^1S_0 - 1s2p\ ^3P_1$

Ratio	Measured	Predicted Ratio	
		Opt. thin ratio	MULTI ratio
I(537)/I(584)	$(1.2 \pm 0.3) \times 10^{-1}$	$(0.6 - 1.3) \times 10^{-1}$	$(1.5) \times 10^{-1}$
I(522)/I(584)	$(3.6 \pm 1.0) \times 10^{-2}$	$(1.8 - 4.2) \times 10^{-2}$	$(5.9) \times 10^{-2}$
I(591)/I(584)	$(9.8 \pm 3.2) \times 10^{-4}$	$(1.0 - 1.8) \times 10^{-4}$	$(4.3) \times 10^{-4}$

Table 2.1: Observed and calculated solar atmosphere helium line ratios with and without the effects of opacity.

591.411$\mathring{A}$. To the author's knowledge this line has not been observed before in the sun. The short illustration shown here provides a good example of the use of ADAS 214 for more complex problems than its assumptions might allow. The code provides a means of quickly estimating the opacity effects on spectral lines of moderately optically thick plasmas, and if the lines are found to fall outside of the optical depths for which the code is valid, it allows the investigator to decide whether it is worthwhile doing a more complex opacity study on the lines in question, as was done in this case.

2.10 Further theory and code development : Inclusion of a background radiation field

2.10.1 Theory

One of the first assumptions made in evaluating the escape and absorption factor expression was the exclusion of a background radiation field. Expressions (2.10) through to (2.14) can be re-evaluated to include a contribution from the background radiation field. Note that the parabolic expression is not included in the work shown here, though it is straightforward to extend the algebra to allow for it.
For the homogeneous distribution the line integrated fluxes become

$$\int_0^b \varepsilon(\nu, l) e^{(l-b)\bar{\alpha}(\nu)} dl \;=\; \frac{\varepsilon(\nu)}{\bar{\alpha}(\nu)} \left[1 - e^{\bar{\alpha}(\nu)b}\right] + I(\nu, 0) e^{-\bar{\alpha}(\nu)b}$$

$$\int_0^{2b} \varepsilon(\nu,l) e^{(l-2b)\bar{\alpha}(\nu)} dl = \frac{\varepsilon(\nu)}{\bar{\alpha}(\nu)} \left[1 - e^{2\bar{\alpha}(\nu)b}\right] + I(\nu,0) e^{-\bar{\alpha}(\nu)2b} \quad (2.18)$$

and

$$\begin{aligned} \int_0^{b} \varepsilon(\nu,l) e^{(l-b)\bar{\alpha}(\nu)} dl &= \frac{\varepsilon(\nu,b)}{\bar{\alpha}(\nu)} \left[1 - \frac{1}{\bar{\alpha}(\nu)b} + \frac{1}{\bar{\alpha}(\nu)b} e^{-\bar{\alpha}(\nu)b}\right] + I(\nu,0) e^{-\bar{\alpha}(\nu)b} \\ \int_0^{2b} \varepsilon(\nu,l) e^{(l-2b)\bar{\alpha}(\nu)} dl &= \frac{\varepsilon(\nu,b)}{\bar{\alpha}(\nu)} \frac{1}{\bar{\alpha}(\nu)b} \left[1 - 2e^{-\bar{\alpha}(\nu)b} + e^{-2\bar{\alpha}(\nu)b}\right] + I(\nu,0) e^{-\bar{\alpha}(\nu)2b} \end{aligned} \quad (2.19)$$

for the linear distribution.

These result in escape and absorption factors expressions for a homogeneous density distribution of

$$\begin{aligned} \Theta &= \frac{1}{2b\varepsilon_L + \int_{line} u_{BB}(\nu) d\nu} \int_{line} \left[\frac{\varepsilon_L}{\bar{\alpha_L}} \left[1 - e^{-2\bar{\alpha}(\nu)b}\right] + u_{BB}(\nu) e^{-2\bar{\alpha}(\nu)b}\right] d\nu \\ \Lambda(l) &= \frac{2}{4\pi} \int_\Omega \int_0^\infty \left[\theta(\nu) e^{-\bar{\alpha}(\nu)b(\Omega)} - \frac{\bar{\alpha(\nu)}}{\varepsilon_L} u_{BB}(\nu) e^{-\bar{\alpha}(\nu)b(\Omega)}\right] d\nu d\Omega \end{aligned} \quad (2.20)$$

and

$$\begin{aligned} \Theta &= \frac{1}{b\varepsilon_L + 2\int_{line} u_{BB}(\nu) d\nu} \\ &\quad \times \left[2 \int_{line} \frac{\varepsilon(\nu,b)}{\bar{\alpha}(\nu)} \frac{1}{\bar{\alpha}(\nu)b} \left[1 - 2e^{-\bar{\alpha}(\nu)b} + e^{-2\bar{\alpha}(\nu)b}\right] + u_{BB}(\nu) e^{-2\bar{\alpha}(\nu)b}\right] d\nu \\ \Lambda(l) &= \frac{2}{4\pi} \int_\Omega \int_0^\infty \left[\left(\frac{1}{\bar{\alpha}_L b(\Omega)} - \frac{1}{\bar{\alpha}_L b(\Omega)} e^{-\bar{\alpha}_L b(\Omega)}\right) - \right. \\ &\quad \left. \frac{\bar{\alpha}(\nu)}{\varepsilon_L(b)} u_{BB}(\nu) e^{-\bar{\alpha}(\nu)b(\Omega)}\right] d\nu d\Omega \end{aligned} \quad (2.21)$$

for a linear density distribution, where $u_{BB}(\nu)$ is the incident background radiation density at frequency ν. A modified version of ADAS 214 was produced to account for such a background field. Although the resultant escape probabilities were found

to be well behaved, it proved to be difficult to evaluate meaningful absorption factors for all possible optical depths. For example, consider the case of a plasma that shows only moderate opacity and has an incident background radiation field which is close to black body. Due to the low opacity of the plasma, the radiation field at the center will be close to black body (mostly due to the background field). Note from the absorption factor expressions (2.20) and (2.21) that the multiplier on u_{BB} is α/ε. If the background radiation density is black body, one only gets $\lambda = 0$ if α and ε have Boltzmann populations. However, the code assumes an initial excited state population structure with default Boltzmann deviation factors of 0.1 (with the option for the user to enter a different deviation factor). This serves to increase α/ε, allowing the background field contribution to λ to become less than negative one, resulting in negative absorption factors. If the system were allowed to iterate then the large radiation field would increase the population of the excited states and keep the absorption factors positive. Since the direction of the present work seeks to exploit the linear nature of the escape factor approach no further work was done on this aspect.

2.11 Conclusions

A description of the ADAS 214 opacity code has been given and it can be seen that it integrates well with the existing ADAS collisional-radiative codes. It provides a quick and effective way of evaluating opacity adjustments to both atomic populations and emergent flux from moderately optically thick plasmas.

Chapter 3

Continuity of high series opacity

3.1 Introduction

The present chapter focuses on calculating opacity consistently in a single spectral series from low lying discrete member lines through to the continuum within the escape factor framework. This is done by analytically extending the usual bound-bound definitions of the escape probabilities and absorption factors into bound-free regimes. It is shown that blended high series lines merge with a broadened continuum smoothly across the series limit with no need to introduce an ionising microfield which effectively 'dissolves' high quantum shells into the continuum. The continuous escape probabilities are evaluated in a new code and used to adjust high series and bound-free continuum emergent intensities for opacity. Similarly the continuous absorption factors are used to modify high series spontaneous emission and free electron recombination rates for population calculation in an analogous manner to their bound-bound counterparts. This chapter considers only hydrogenic opacity, with the recognition that the theory can be extended to non-hydrogenic elements.

3.2 Analytic continuity

Expressions (1.8) and (1.14) are the starting points for demonstrating analytic continuity. In the following algebra, bound-bound quantities are denoted either by the

subscripts 'nn' or 'bb', and the bound-free quantities with subscripts 'bf' or '$n\kappa$' with no change in meaning. We seek to show that

$$\Lambda_{bb}(\underline{r}) = 1 - \frac{\int \alpha_{bb}(\nu, \underline{r}) I(\nu, \underline{r}) d\nu}{\int \int_{\Omega} \varepsilon_{bb}(\nu, \underline{r}) d\Omega d\nu} \tag{3.1}$$

continues analytically into

$$\Lambda_{bf}(\underline{r}) = 1 - \frac{\int \alpha_{bf}(\nu, \underline{r}) I(\nu, \underline{r}) d\nu}{\int \int_{\Omega} \varepsilon_{bf}(\nu, \underline{r}) d\Omega d\nu} \tag{3.2}$$

and that

$$\Theta_{bb} = \frac{\int_{\Delta\nu} \int_0^b \varepsilon_{bb}(\nu, l) e^{-\int_l^b \alpha_{bb}(\nu, l') dl'} dl d\nu}{\int_{\Delta\nu} \int_0^b \varepsilon_{bb}(\nu, l) dl d\nu} \tag{3.3}$$

continues into

$$\Theta_{bf} = \frac{\int_{\Delta\nu} \int_0^b \varepsilon_{bf}(\nu, l) e^{-\int_l^b \alpha_{bf}(\nu, l') dl'} dl d\nu}{\int_{\Delta\nu} \int_0^b \varepsilon_{bf}(\nu, l) dl d\nu} \tag{3.4}$$

The b-b and b-f emission and absorption coefficients are defined in chapter 1. We seek to prove, upon transformation of $n' \to i\kappa$, that $\varepsilon_{bb} \to \varepsilon_{bf}$ and $\alpha_{bb} \to \alpha_{bf}$, leading to continuity in Θ and Λ. For clarity, the ε and α expressions are reproduced below.

$$\varepsilon_{bb}(\nu) = \frac{1}{4\pi} N_{n'} A_{n' \to n} \phi_{n'n}(\nu) \tag{3.5}$$

will continue into

$$\begin{aligned} \varepsilon_{bf}(\nu) d\nu &= \frac{1}{4\pi} \left[N_i f(v) b_\kappa dv \right] \left[N_e v \sigma_{\kappa n} \right] \\ \Rightarrow \varepsilon_{bf}(\nu) &= \frac{1}{4\pi} \left[N_i f(v) b_\kappa dv \right] \left[N_e v \sigma_{\kappa n} \frac{1}{d\kappa} \right] \frac{d\kappa}{d\nu} \end{aligned} \tag{3.6}$$

with $f(v)$ being the Maxwellian velocity distribution for free electrons and $\sigma_{\kappa n}$ is the target area for free electron capture, given by

$$\sigma_{\kappa n} = \frac{2^4}{3\sqrt{3}} \frac{e^2 h}{m^2 c^3} \frac{1}{\left[\frac{1}{n^2} + \frac{1}{\kappa^2} \right]} \frac{\kappa^2}{n^3} g_{\kappa n}^{II} \tag{3.7}$$

Similarly

$$\alpha_{nn'}(\nu) = N_n \frac{\pi e^2}{mc} f'_{nn'} \phi_{nn'}(\nu) g^I_{nn'} \tag{3.8}$$

will continue into

$$\alpha_{n\kappa}(\nu) = N_n \frac{\pi e^2}{mc} f'_{n\kappa} \frac{d\kappa}{d\nu} g^{II}_{n\kappa} \tag{3.9}$$

Note that the proofs shown here hold for NLTE population distributions with the inclusion of b-factors, b_n, for bound states which continue into b_κ factors for free states (representing deviations from a Maxwellian free-electron velocity distribution).

3.2.1 Continuity of emission coefficient

The resultant emission rate to level n for a given series, once the profiles start to blend together at high series members, is simply the sum of the b-b emission rates over all transitions in the series. That is,

$$\varepsilon_n(\nu) = \frac{1}{4\pi} \sum_{n'} N_{n'} A_{n' \to n} \phi_{n'n}(\nu) \tag{3.10}$$

As the series limit is approached, only nearby profiles contribute, the values of $N_{n'}$ and $A_{n' \to n}$ do not vary significantly and can be replaced by representative values $N_{\bar{n}'}$ and $A_{\bar{n}' \to n}$ and taken out of the summation. The emission rate to level n then becomes

$$\varepsilon_n(\nu) = \frac{1}{4\pi} N_{\bar{n}'} A_{\bar{n}' \to n} \sum_{n'} \phi_{n'n}(\nu) \tag{3.11}$$

For high series members, the profiles broaden and tend to the same basic distribution, only shifted slightly in frequency due to the increased energy of the upper level. We calculate the average emission rate over a small frequency interval, equal to the separation between line centres $\Delta\nu$

$$\varepsilon_n(\nu) = \frac{1}{4\pi} N_{\bar{n}'} A_{\bar{n}' \to n} \frac{1}{\Delta\nu} \int_{\Delta\nu} \sum_{n'} \phi_{n'n}(\nu) d\nu \tag{3.12}$$

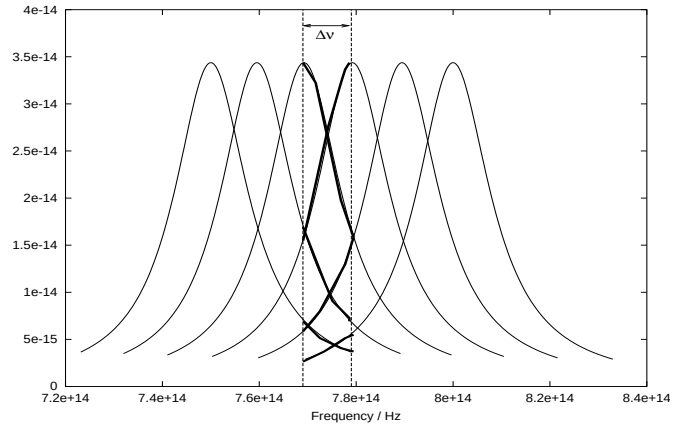

Figure 3.1: Diagram illustrating the contribution of overlapping profiles to the integration in eqn (3.12). Consider the contribution from each profile to the region of integration within the dotted lines. If one traces out the contributions from each profile in turn (see the bold segments of the profiles) it is equivalent to integrating over one normalised profile.

For high series members $\phi_{n'n}(\nu)$ is approximately the same for adjacent profiles, only shifted in frequency by $\Delta\nu$. As can be seen from figure 3.1, the summation inside the integral simply serves to select adjacent segments from the normalised profiles, and in the case of figure 3.1 we have an integral over one complete profile. If the region $\Delta\nu$ is then increased to cover $\Delta\bar{n}'$ profiles, the integral would be over $\Delta\bar{n}'$ normalised profiles. Thus the integral over $\Delta\nu$ reduces to $\Delta\bar{n}'$ (i.e. the number of line centres within the $\Delta\nu$ frequency region). Note that as our frequency element approaches the series limit, broadened profiles from the continuum form part of this contribution to the $\Delta\nu$ region (this is most clearly seen in the numerical simulation later in this section). In the limit of $\Delta\nu$ becoming very small, the average over the frequency region tends to $d\bar{n}'/d\nu$. Thus the number of spontaneous emissions over the region $d\nu$ is given by

$$\varepsilon_n(\nu) = \frac{1}{4\pi} N_{\bar{n}'} A_{\bar{n}' \to n} \frac{d\bar{n}'}{d\nu} \tag{3.13}$$

This is then analytically extended to continuum states using expressions for $N_{\bar{n}'}$ and $A_{\bar{n}'\to n}$ transformed into the continuum. That is,

$$N_{\bar{n}'} = N_e N_i \left[\frac{h^2}{2\pi m k T_e}\right]^{\frac{3}{2}} \frac{\omega_{\bar{n}'}}{2} \exp\left[\frac{I_{\bar{n}'}}{kT_e}\right] b_{\bar{n}'} \tag{3.14}$$

is extended into free states by letting $\bar{n'} \to i\kappa$ and using

$$\omega_\kappa = \frac{8\pi m^3 v^2 dv}{N_e h^3} \tag{3.15}$$

for the statistical weight of an electron in state κ (Menzel & Pekeris, 1935). The continuum statistical weight is defined over a momentum and volume element and is defined such that it is consistent with ω_n, that is there is no ω_+ term for the statistical weight of the ion. Also use

$$I_{\bar{n}'} = \frac{Rz_0^2}{\bar{n}'^2} \tag{3.16}$$

for the ionisation potential of level $\bar{n'}$. Thus

$$\begin{aligned} N_{\bar{n}'n} &\to N_e N_i \left[\frac{h^2}{2\pi m k T_e}\right]^{\frac{3}{2}} \frac{1}{2} \frac{8\pi m^3 v^2 dv}{N_e h^3} \exp\left[-\frac{Rz_0^2}{\kappa^2 k T_e}\right] b_\kappa \\ &= N_i 4\pi v^2 \left[\frac{1}{2\pi k T_e}\right]^{\frac{3}{2}} \exp\left[-\frac{Rz_0^2}{\kappa^2 k T_e}\right] b_\kappa \frac{m^3}{m^{\frac{3}{2}}} dv \\ &= N_i 4\pi v^2 \left[\frac{m}{2\pi k T_e}\right]^{\frac{3}{2}} \exp\left[-\frac{Rz_0^2}{\kappa^2 k T_e}\right] b_\kappa dv \end{aligned} \tag{3.17}$$

The Maxwellian velocity distribution, $f(v)$ is given by

$$f(v)dv = 4\pi v^2 \left[\frac{m}{2\pi k T_e}\right]^{\frac{3}{2}} \exp\left[-\frac{mv^2}{2kT_e}\right] dv \tag{3.18}$$

and the energy (E_κ) of the free electron is

$$E_\kappa = \frac{1}{2} m v^2 = \frac{Rz_0^2}{\kappa^2} \tag{3.19}$$

Thus letting $n' \to i\kappa$ in equation (3.17) gives

$$N_{n'n} \rightarrow N_i f(v) b_\kappa dv \tag{3.20}$$

To transform the A-values, express A in terms of oscillator strengths, i.e.

$$A_{\bar{n'}\rightarrow n} = \frac{\omega_n}{\omega_{\bar{n'}}} \frac{8\pi^2 e^2}{mc^3} \nu^2_{\bar{n'}n} f'_{\bar{n'}n} g^I_{\bar{n'}n} \tag{3.21}$$

and use

$$\nu_{\bar{n'}n} = \frac{Rz_0^2}{h}\left[\frac{1}{n^2} - \frac{1}{\bar{n'}^2}\right] \tag{3.22}$$

and

$$f'_{\bar{n'}n} = \frac{2^6}{3\sqrt{3}\pi} \frac{1}{\omega_n} \frac{1}{\left[\frac{1}{n^2} - \frac{1}{\bar{n'}^2}\right]^3} \frac{1}{n^3 \bar{n'}^3} \tag{3.23}$$

to obtain

$$\begin{aligned} A_{\bar{n'}\rightarrow n} &= \frac{\omega_n}{\omega_{\bar{n'}}} \frac{8\pi^2 e^2}{mc^3} \left(\frac{Rz_0^2}{h}\right)^2 \left[\frac{1}{n^2} - \frac{1}{\bar{n'}^2}\right]^2 \frac{2^6}{3\sqrt{3}\pi} \frac{1}{\omega_n} \frac{1}{\left[\frac{1}{n^2} - \frac{1}{\bar{n'}^2}\right]^3} \frac{1}{n^3 \bar{n'}^3} g^I_{\bar{n'}n} \\ &= \frac{1}{\omega_{\bar{n'}}} \frac{8\pi^2 e^2}{mc^3} \left(\frac{Rz_0^2}{h}\right)^2 \frac{2^6}{3\sqrt{3}\pi} \frac{1}{\left[\frac{1}{n^2} - \frac{1}{\bar{n'}^2}\right]} \frac{1}{n^3 n'^3} g^I_{\bar{n'}n} \end{aligned} \tag{3.24}$$

Letting $n \rightarrow i\kappa$ and using eqn (3.15) for the statistical weight of an electron in the continuum gives

$$\begin{aligned} A_{\bar{n'}\rightarrow n} &\rightarrow -\frac{N_e h^3}{8\pi m^3 v^2 dv} \frac{8\pi^2 e^2}{mc^3} \frac{R^2 z_0^4}{h^2} \frac{2^6}{3\sqrt{3}\pi} \frac{1}{\left[\frac{1}{n^2} + \frac{1}{\kappa^2}\right]} \frac{1}{n^3 \kappa^3} g^{II}_{\kappa n} \\ &= \frac{N_e h}{v^2 dv} \frac{e^2}{m^4 c^3} R^2 z_0^4 \frac{2^6}{3\sqrt{3}} \frac{1}{\left[\frac{1}{n^2} + \frac{1}{\kappa^2}\right]} \frac{1}{n^3 \kappa^3} g^{II}_{\kappa n} \end{aligned} \tag{3.25}$$

Then using

$$\frac{1}{2} m v^2 = \frac{Rz_0^2}{\kappa^2} \tag{3.26}$$

to convert the dv into $d\kappa$ via

$$dv = -\frac{1}{mv}\frac{2Rz_0^2}{\kappa^3}d\kappa \tag{3.27}$$

The transformed A-value is

$$\begin{aligned} A_{\bar{n'}\to n} &\to \left[-N_e h\frac{1}{v^2}\frac{1}{dv}\frac{e^2}{m^4c^3}R^2z_0^4\right]\left[\frac{2^6}{3\sqrt{3}}\frac{1}{\left[\frac{1}{n^2}+\frac{1}{\kappa^2}\right]}\frac{1}{n^3\kappa^3}g_{\kappa n}^{II}\right] \\ &= -N_e h\left[\frac{m\kappa^2}{2Rz_0^2}\right]\left[-\frac{mv\kappa^3}{2Rz_0^2 d\kappa}\right]\frac{e^2}{m^4c^3}R^2z_0^4\left[\frac{2^6}{3\sqrt{3}}\frac{1}{\left[\frac{1}{n^2}+\frac{1}{\kappa^2}\right]}\frac{1}{n^3\kappa^3}g_{\kappa n}^{II}\right] \\ &= \left[N_e v\frac{2^4}{3\sqrt{3}}\frac{e^2h}{m^2c^3}\frac{1}{\left[\frac{1}{n^2}+\frac{1}{\kappa^2}\right]}\frac{\kappa^2}{n^3}g_{\kappa n}^{II}\frac{1}{d\kappa}\right] \\ &= N_e v\sigma_{\kappa n}\frac{1}{d\kappa} \end{aligned} \tag{3.28}$$

which is the bound-free emission rate.

Thus the bound-bound emission coefficient continues smoothly into the bound-free expression as $\bar{n'} \to i\kappa$. That is

$$\varepsilon_{\bar{n'}\to n}(\nu) \longrightarrow \frac{1}{4\pi}\left[N_i f(v)dv\right]\left[N_e v\sigma_{\kappa n}\frac{1}{d\kappa}\right]\frac{d\kappa}{d\nu} \tag{3.29}$$

and analytic continuity between equations (3.5) and (3.6) has been shown. A code was written to demonstrate the continuity of the resultant emission coefficient across the series limit. Both Lorentzian profile expressions and the expression of Griem (1960) could be used in the calculation, and existing ADAS subroutines were used to evaluate the necessary Gaunt factors, A-values and population b-factors. For the demonstration shown here, Lorentzian profiles are used throughout. Note that the proof outlined here works independently of the choice of line profile, the only necessity has been that the line profiles must be normalised. In practice one would use appropriate line profile expressions and widths for the plasma under investigation. See chapter 5 for an opacity calculation using the profile expression of Griem.

The code takes the same approach in treating the continuity as the proof shown above. That is, a wavelength element is considered in the spectrum and the contributions

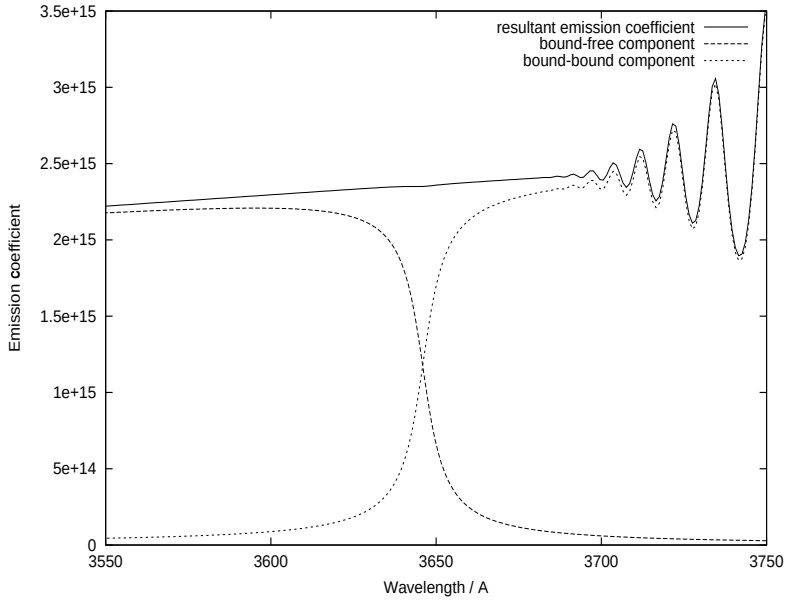

Figure 3.2: Emission coefficient for the Balmer series plotted across the series limit. The code was run for $N_e = 2 \times 10^{14} cm^{-3}$, $T_e = 1eV$. Note that the continuum contribution is made up of a continuous set of bound-free line profiles.

from all line and continuum profiles to this element are evaluated. This region is then scanned across the series limit and the results plotted. In the blended region and continuum this wavelength segment corresponds to an 'element' of population, made up from the continuous free states or the pseudo-continuous highly excited states. At low series wavelengths the main contribution to the wavelength element is from the sum of all bound-bound profiles. As one approaches the series limit, and the states become indistinguishable and it is more appropriate to model this summation as an integral of the contributing profiles over energy. The continuum is modelled as a continuous set of line profiles (assumed Lorentzian with constant width), and the contribution to the wavelength element found from the integral over energy of these bound-free profiles. The resultant emission coefficient in the wavelength element is the sum of the bound-bound and bound-free contributions. The results are shown in figure 3.2.

Note that the bound-bound profiles make a contribution at continuum wavelengths and similarly the broadened continuum contributes at bound-bound wavelengths. It is

the combination of these contributions which leads to the smooth continuation across the series limit of the emission coefficient. b-factors were calculated for all transitions, though for the higher transitions they are equal to one. A maxwellian velocity distribution was assumed (i.e. $b_\kappa = 1$). However, the proof of continuity is for emission from an element of population in the continuum, which is then 'scanned' down into bound states. Thus the expected emission resulting from a non-Maxwellian distribution of free electrons can be modelled with the introduction of the appropriate b_κ values. Note that the emission coefficient well into the continuum is made up from all the contributing bound-free profiles and is equal to the usual analytic expression used to model the continuum profile (equation (3.6)). The approach of continuity shown here is significantly different from the conventional approach, whereby an ionising microfield is introduced. See section 3.3 for a discussion on this point.

3.2.2 Continuity of absorption coefficient

In a similar manner the bound-bound absorption coefficient, equation (3.8), continues into its corresponding bound-free expression, equation (3.9). Starting with the bound-bound absorption coefficient expression, for absorption to high n-shells the upper levels become progressively closer together until adjacent absorption profiles start to overlap. The number of absorptions at frequency ν due to all the overlapping lines is

$$\alpha_n(\nu) = N_n \frac{\pi e^2}{mc} \sum_{n'} f'_{nn'} g^I_{nn'} \phi_{nn'}(\nu) \tag{3.30}$$

The average of this quantity over a small frequency region $\Delta\nu$ is

$$\alpha_n(\nu) = N_n \frac{\pi e^2}{mc} \frac{1}{\Delta\nu} \int_{\Delta\nu} \sum_{n'} f'_{nn'} g^I_{nn'} \phi_{nn'}(\nu) d\nu \tag{3.31}$$

On approaching the series limit the profiles, $\phi_{nn'}$, that contribute to the $\Delta\nu$ region have approximately the same shape and are simply shifted along in frequency. The oscillator strength and Gaunt factor values for the contributing transitions can be replaced by representative values ($= f'_{n\bar{n'}}$ and $g^I_{n\bar{n'}}$). This produces

$$\alpha_n = N_n \frac{\pi e^2}{mc} f'_{n\bar{n}'} g^I_{n\bar{n}'} \frac{1}{\Delta\nu} \int_{\Delta\nu} \sum_{n'} \phi_{nn'}(\nu) d\nu \tag{3.32}$$

Again considering $\Delta\nu$ equal to the separation between the line profiles a similar argument to the emission case holds. The effect of the summation is to contribute adjacent components in the line profile to the integral such that the integration is effectively over the number of line centres in $\Delta\nu$. Because the profiles are normalised, the integral reduces to $\Delta\bar{n}'$ and as $\Delta\nu$ becomes infinitesimally small the integral tends to $d\bar{n}'$. The absorption coefficient then becomes

$$\alpha_{n\bar{n}'}(\nu) = N_n \frac{\pi e^2}{mc} f'_{n\bar{n}'} g^I_{n\bar{n}'} \frac{d\bar{n}'}{d\nu} \tag{3.33}$$

$g^I_{nn'} \rightarrow g^{II}_{n\kappa}$ as shown in Burgess & Summers (1987) and $f'_{n\bar{n}'} \rightarrow -f'_{n\kappa}$ as seen in the definitions from Menzel & Pekeris (1935). From equation (3.22)

$$\frac{d\bar{n}'}{d\nu} \rightarrow -\frac{d\kappa}{d\nu} \tag{3.34}$$

It is now clear that equation (3.33) continues into equation (3.9) on transforming $n' \rightarrow i\kappa$. That is,

$$\begin{aligned} \alpha_{nn'}(\nu) &\rightarrow N_n \frac{\pi e^2}{mc} g^{II}_{n\kappa}(-f'_{n\kappa}) \left(-\frac{d\kappa}{d\nu}\right) \\ &= N_n \frac{\pi e^2}{mc} g^{II}_{n\kappa} f'_{n\kappa} \frac{d\kappa}{d\nu} \\ &= \alpha_{n\kappa}(\nu) \end{aligned} \tag{3.35}$$

The continuous absorption coefficient was also evaluated numerically. Using the same technique as for the emission coefficient, the contributions to a wavelength element were evaluated and this wavelength element 'scanned' across the series limit. The continuum contribution is modelled as the integral over free energies of the contributing continuum profiles (assumed Lorentzian in the calculation shown here). The bound-bound contribution is evaluated from the sum of all series profiles at low series wavelengths, and as an integral over bound energies after a certain wavelength cutoff. In practice it was found that the sum over all bound-bound profiles could be extended

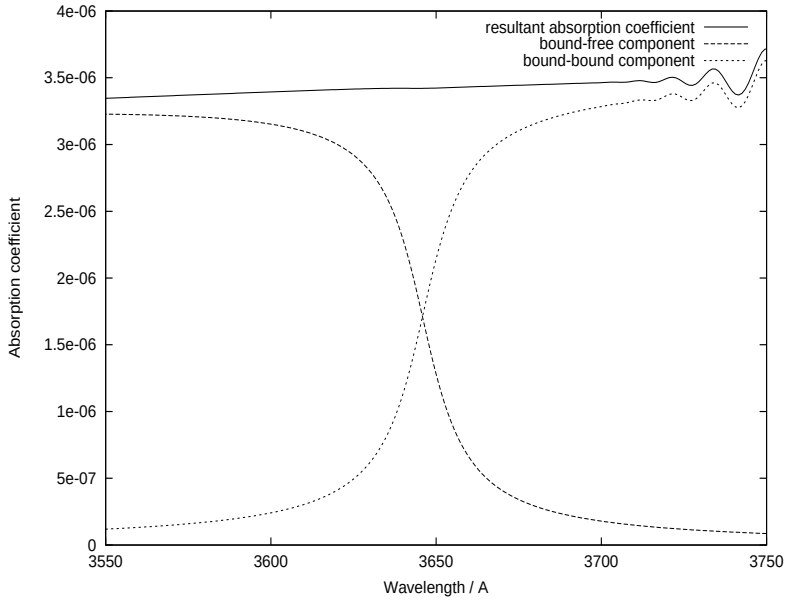

Figure 3.3: Absorption coefficient for the Balmer series plotted across the series limit. The code was run for $N_e = 2 \times 10^{14} cm^{-3}$, $T_e = 1eV$.

to sufficiently high profiles to catch all the details of the integration. The results are shown in figure 3.3.

Thus analytic continuity in each quantity in the absorption factor and escape probability equations has been shown and the bound-bound absorption factors and escape probabilities continue smoothly into the corresponding bound-free expressions. This has been evaluated for two practical examples in section 3.4.

3.3 Contrast with the occupation probability formalism

There is an alternative approach to deal with the detailed treatment of the line blending near the series limit. The work stems from the original analysis of Inglis & Teller (1939) who derived an equation relating the last observable series line to the local electron density. As a rough estimate the continuum is often considered to advance down to this 'spurious continuum edge'. A more detailed treatment is to introduce

a plasma microfield (set up by the fluctuating ions in the vicinity of the emitting atom or ion) to achieve smooth merging of blended lines into the continuum. The argument is that this field introduces a potential which can ionise highly excited electrons, thus there exists a quantum level above which electrons will be ionised before they have the chance to spontaneously decay to a lower level and electrons in these excited states will behave as if they were effectively free electrons. An 'occupation probability' can be evaluated, giving the probability that an excited electron is effectively 'dissolved' into the continuum. This approach has been widely used both in modelling series emission profiles and in collisional-radiative calculations. It was introduced by Gurovich & Engel'sht (1977) to obtain a non-divergent partition function and by Pigarov et al. (1998) in his modelling of atomic populations and emergent fluxes for Balmer series limit calculations.

Hubney et al. (1994) introduce an occupation probability, developed in Hummer & Mihalas (1988), in their stellar atmospheres code to include the effects of line blending near the series limit. It is instructive to examine their expression for the total absorption coefficient, derived from equation (2.4) of Hubney et al. (1994):

$$\alpha_n = N_n \left[\sum_{n'>n} \omega_{n'} \frac{\pi e^2}{mc} f_{n'n} \Phi_{n'n}(\nu) + \begin{cases} \sum_{n'>n} (1-\omega_{n'}) \frac{\pi e^2}{mc} \frac{df_{n'n}}{d\nu} & \nu < \nu_{nn'} \\ \sigma_{n\kappa} & \nu > \nu_{nn'} \end{cases} \right] \quad (3.36)$$

where $\sigma_{n\kappa}$ is equivalent to our bound-free absorption coefficient. The similarities with equations (3.30) and (3.33) are evident. The main difference is the introduction of the factor ω_n which they refer to as the 'dissolution factor'. Their blended line contribution is gradually reduced by this factor while the continuation of the bound-free absorption coefficient to bound-bound wavelengths is simultaneously increased. Thus as one approaches the series limit the absorption coefficient is driven to the extended continuum value by the microfield. Note that the continuum is treated as a profile with a sharp edge, not as a sum of bound-free profiles.

This approach differs from ours in that we have shown that the blended profiles along with the broadened continuum contribution give emission and absorption coefficients which merge smoothly through to the continuum, without any need to introduce an ionising microfield. The technique of modifying the statistical balance equations with

a level dissolution factor is incorrect on the grounds of detailed balance and energy conservation. Of course the microfield effects must be included in the collisional-radiative equations and the line broadening expressions to allow the populations and profiles to be accurately evaluated. The microfield effects on the line profiles are already included in this work with the use of the PPP broadening code. The inclusion of the microfield within the collisional-radiative framework as a rate with a corresponding inverse process is left for future work. The idea is that the microfield's effect on the populations are primarily due to individual ions moving closer than the nearest neighbour distance . These ions can remove an electron possibly via a charge exchange mechanism. This allows incorporation of the microfield as a process satisfying microreversibility consistently within the collisional-radiative framework and is planned for the next stage of ADAS development. Thus although the final continuous coefficients in this chapter are similar to those produced by the occupation probability method, the philosophies of the two approaches are quite different.

To the author's knowledge the generic proof of continuity shown here which holds for any physical set of line profiles has not been demonstrated before, with most authors opting for the occupation probability method. The closest example of the proof of this chapter is found in Seaton (1990). He considers the case of no line dissolution (i.e. no microfield effects) and states that the sum of many overlapping high series line profiles (considered to be step functions) in the high series absorption coefficient tends towards the photo-ionisation rate. However he then goes on to use an occupation probability approach to deal with series limits in his modelling of atomic data for hydrogen for the Iron project.

3.4 The use of continuous escape and absorption expressions

The absorption factor and escape probability expressions can now be evaluated. Such quantities can already be evaluated for discrete spectral lines (see chapter 2) and for continuum radiation (Drawin, 1970). Using the continuity theory shown here,

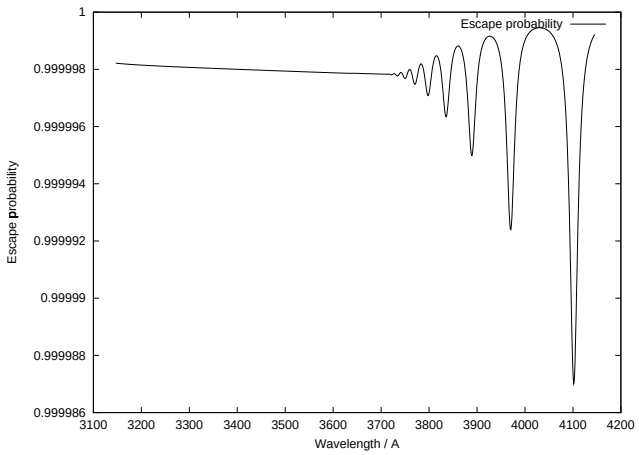

Figure 3.4: Continuous escape probability plotted for the case of the Balmer series in the fusion divertor. $N_e = 1 \times 10^{14} cm^{-3}$, $T_e = 1eV$, length=5cm, assuming Lorentzian profiles and a Maxwellian velocity distribution for the free electrons. Note the smooth merging of the escape probability across the series limit.

this can be extended to include elements 'within' the blended high series region and continuum. The continuous emission and absorption coefficients are combined to produce the necessary opacity expression as a function of plasma parameters.

3.4.1 Some illustrations

Escape probability evaluated

Using the resultant ε and α expressions it is possible to evaluate Θ across the series limit. Consider a homogeneous plasma such that ε and α are independent of position. Equation (3.3) reduces to

$$\Theta = \frac{\int_{\Delta\nu} \frac{\varepsilon(\nu)}{\alpha(\nu)} (1 - e^{-\alpha(\nu)b}) d\nu}{b \int_{\Delta\nu} \varepsilon(\nu) d\nu} \tag{3.37}$$

Consider the Balmer series limit in fusion divertor plasmas. This region is expected to be optically thin, with the lower Lyman members being the only thick lines. Nevertheless it provides a useful check on our method. The escape probability code was run for $N_e = 1 \times 10^{14} cm^{-3}$, $T_e = 1eV$, $b = 5cm$, the results are shown in figure 3.4. It can be seen that the escape factor for the Balmer lines through to and including

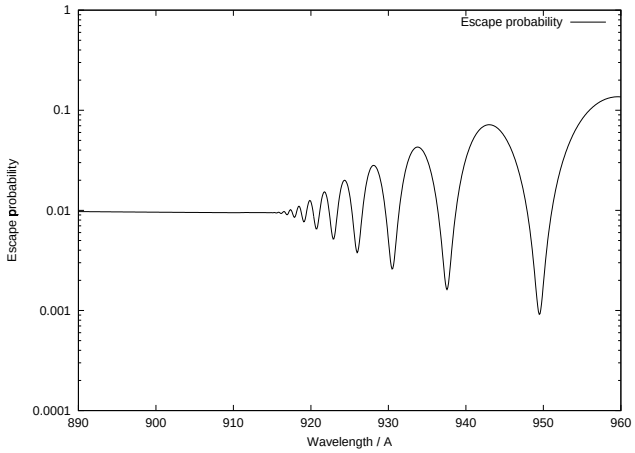

Figure 3.5: Continuous escape probability plotted for the case of the Lyman series in solar prominences. $N_e = 1 \times 10^{10} cm^{-3}$, $T_e = 1eV$, length=$1 \times 10^8 cm$. Only electron broadened Lorentzian profiles were used in this calculation. The Lyman series limit occurs at ~ 911 Å.

the continuum is, for all practical purposes, optically thin. Note that Θ continues smoothly across the series limit (~ 3645 Å).

Next consider the case of the Lyman series limit in solar prominences. In this case one expects the Lyman lines and continuum to be extremely optically thick. It should be noted that the atomic populations in a solar prominence are strongly controlled by photo-absorption of incident radiation and that a full radiative transfer approach is required to accurately model the populations, fluxes and exact line profile shapes (see Gouttebroze et al., 1993). We use the solar prominence case as a check to see if the continuum expressions developed here can predict reasonable continuum opacities which smoothly merge into high series opacities. Thus Θ was evaluated for $N_e = 1 \times 10^{10} cm^{-3}$, $T_e = 1eV$, $b = 1 \times 10^8 cm$, the results are shown in figure 3.5. Note that there is indeed significant opacity at continuum wavelengths and a smooth merging of Θ into bound-bound opacity across the series limit (~ 911 Å).

Absorption factors evaluated

The generic expression for an absorption factor in terms of the continuous absorption and emission coefficients is

$$\Lambda = 1 - \frac{\int_{\Delta\nu} \alpha_n(\nu, \underline{r}) I(\nu, \underline{r}) d\nu}{\int_{\Omega} \int_{\Delta\nu} \varepsilon_n(\nu, \underline{r}) d\nu d\Omega} \tag{3.38}$$

In the evaluation of Λ, the intensity term is evaluated by integrating the emission, attenuated by photo-absorption, over the volume of the plasma to get the resultant intensity at the point of interest. For the case of Λ at the centre of a homogeneous density plasma of spherical geometry (of radius b) the absorption factor reduces to

$$\Lambda = \frac{\int_{\Delta\nu} \varepsilon(\nu) e^{-b\alpha(\nu)} d\nu}{\int_{\Delta\nu} \varepsilon(\nu) d\nu} \tag{3.39}$$

Figure 3.6 shows the results for the Lyman series limit at expected solar prominence conditions. Λ is evaluated as a function of frequency to produce the absorption factor across the series limit. However, for adjustments to atomic population or free electron distributions it is necessary to define a population element (and hence a frequency element) for which to calculate the Λ factors.

Defining $\Delta\nu$ accordingly gives the expression most appropriate to our desired application. With $\Delta\nu$ covering one complete spectral line it is possible to generate the usual discrete line absorption factors. With $\Delta\nu$ chosen to be a small element, the absorption factor corresponding to a small population element below the continuum edge, or in the continuum itself can be found. If $\Delta\nu$ is chosen to cover $\kappa = \infty \rightarrow 0$ (i.e. $\nu = \nu_i \rightarrow \infty$, with ν_i the frequency at the continuum edge), we average over the whole continuum and get the same expression as Drawin (1970), i.e.

$$\begin{aligned} \Lambda_i &= 1 + \frac{1}{n_z n_e R_i} \left[\frac{\pi e^2}{m_o c} n_{z-1,i} \int_{\nu_i}^{\infty} u(\nu, \underline{r}) \frac{df}{d\nu} d\nu \right] \\ &= 1 - \frac{1}{n_z n_e R_i} \left[\frac{\pi e^2}{m_o c} n_{z-1,i} \int_{\nu_i}^{\infty} u(\nu, \underline{r}) f'_{n\kappa} g^{II}_{n\kappa} \frac{h\kappa^3}{2Rz_0^2} d\nu \right] \end{aligned}$$

where $(n_z n_e R_i)$ is the recombination rate from the continuum to level i

However, if $\Delta\nu$ is chosen to be smaller than this we can examine recombination from different parts of the Maxwellian distribution of free electrons. This could then be used to look at the population distribution 'inside' the continuum and thus to investigate photo-ionisation driven non-Maxwellian free electron distributions.

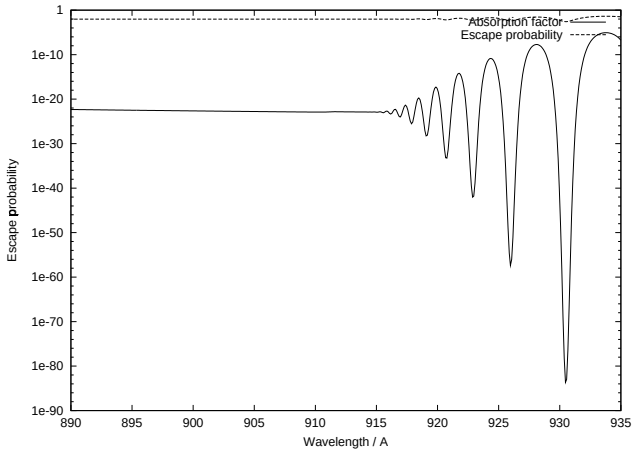

Figure 3.6: Absorption factor plotted for the Lyman series limit for typical prominence parameters. The code was run for $N_e = 1 \times 10^{10} cm^{-3}$, length $= 1 \times 10^8 cm$, $T_e = 1eV$

Note that for the situation shown, the absorption factor is significantly less than the escape factor at the same wavelength. This indicates the case where a photon has a chance of escaping along a given line of sight, but the probability of a photo-absorption at the centre of the plasma is very large due to the large radiation field incident at the centre (generated by the rest of the plasma volume). In these circumstances there is a stronger influence on the optically thick populations than on the emergent flux. Note that we have replaced the notion of a high series level with a small frequency element corresponding to an element of population. We would then need to model all the possible rates to and from these elements. A means of encorporating a continuous Λ into the present collisional-radiative calculation would be to still consider photo-absorption and emission from a discrete level, but to evaluate the intensity term in equation (3.38) from the overlapping profiles. Thus we have the intensity at the point of interest as the resultant intensity due to all overlapping profiles, which can then be absorbed by an individual profile, or emitted from that same profile. That is, our absorption factor expression becomes.

$$\Lambda = 1 - \frac{\int_{\Delta\nu} \alpha_{discrete}(\nu) I_{blend}(\nu) d\nu}{\int_{\Omega} \int_{\Delta\nu} \varepsilon_{discrete}(\nu) d\nu d\Omega} \tag{3.40}$$

where the frequency integration is over the one high series spectral line profile, and the emission and absorption coefficients correspond to the values for that discrete

line, i.e. no line blending is accounted for. It is only in the intensity term that the fully blended emission and absorption coefficients are considered.
This approach has the advantage that it requires minimal changes to the existing collisional-radiative framework. Rates already exist for these high n-shells, and the Λs evaluated here can be added directly, such a technique has been used in section 5.2.2.
One of the long term applications of this work is the investigation into non-Maxwellian free electron distributions. For this the specification of population 'elements' in the continuum and at high quantum shells would be necessary, and the more generic absorption factor expression is the appropriate one to use.

3.5 Conclusions

Analytic continuity of absorption factors and escape probabilities from bound through to free states has been shown. This allows opacity to be modelled in discrete spectral lines, blended high series lines and in the continuum. The approach shown here is contrasted with the occupation probability formalism and shown to be a more meaningful method of extending photo-rates across the ionisation threshold.
It should be noted that with the development of the analytically continuous emission coefficient in this chapter it is immediately possible to predict an emergent flux that continues smoothly from bound-bound to bound-free wavelengths for an optically thin plasma. This has been done for the case of the Balmer series limit in the fusion divertor and is described in section 5.3. The use of the escape probability and absorption factor expressions developed in this chapter allows this type of spectral feature generation to be extended to optically thick conditions (see section 5.2.2).

Chapter 4

Population modelling and computation

In this chapter an overview is presented of a scheme for handling the assembly and solution of collisional-radiative matrices suited to all future collisional-radiative work. In particular it is designed to support studies on heavy species as well as consistent studies involving bound and free states. In this chapter a high quantum shell module is developed which evaluates hydrogenic populations, this will be used to predict all the population distributions necessary for the hydrogen series limit spectral feature code of chapter 5. In section 4.1 the general picture for the new model is outlined. Section 4.2 describes a new set of Gaunt factors for use in the model. The details of the high n-shell collisional-radiative module in the computational implementation are then presented in section 4.3 and in section 4.4 an analysis is done into the validity and automation of the bundling cut-off scheme proposed in the new model.

4.1 An overview of the model

There already exist collisional-radiative codes for light elements within the structure of the ADAS suite of codes (Summers, 2001). These codes have been well tested and are proven to be effective in dealing with light elements. As has been described in chapter 1, it is inappropriate to apply these codes to heavy species and an alternative scheme

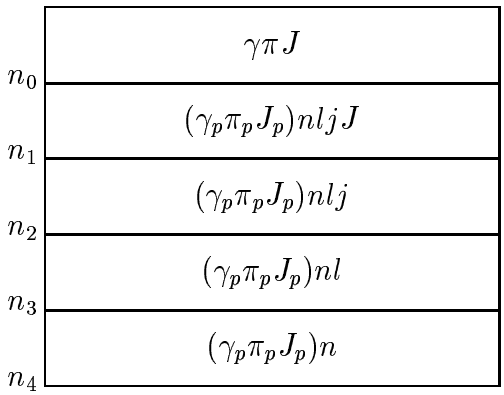

Figure 4.1: The details of the bundling scheme proposed for the new model.

must be developed. Figure 4.1 shows the new general picture with the switching principal quantum shells defining the subdivisions. In this new model one considers a fully resolved picture for the low levels, with the valence electron in the core . Here γ represents the configuration, π the parity and J the total angular momentum of the system. If the valence electron is in a more highly excited principal quantum shell it is possible to view the electron as 'built' on a parent structure. Here γ_p represents the parent level's configuration, π_p its parity and J_p its total angular momentum. The decreasing levels of resolution become valid as the levels become more degenerate and level populations become statistically distributed. One is therefore able to bundle the populations progressively into these less resolved pictures.

With the subdivisions in the level schemes shown in figure 4.1 it is possible to modularise the assembly of the collisional-radiative matrix, in particular for transitions where the parent is invariant. Consider briefly how the different levels of resolution that such a model possesses should be dealt with. For transitions within the two lowest schemes (i.e. $n < n_1$), one has a fully J-resolved system with corresponding transitions between all the possible levels. The rates for these regimes must be of high quality due to the detailed spectroscopy that is expected to be performed on the resulting spectra. These rates are assembled from the most comprehensive calculated and measured data available. The treatment of these lower levels falls within

the approach of the ADAS 208 statistical balance code, this code uses fundamental energy level and rate data from pre-assembled ADAS adf files. The influence of the higher populations are projected onto the lower level results. The treatment of the low levels is already well understood within the context of existing ADAS codes, and becomes an issue of gathering or calculating all of the necessary atomic data. This is a significant task for the heavier species due to the large sets of levels (arising from the J resolution) which must be dealt with.

This chapter concentrates on developing a general model and code that can assemble the collisional-radiative matrix blocks for the remaining three degrees of resolution. That is, the following block of the collisional-radiative matrix will be assembled.

$$\begin{array}{c|ccc|} & nlj & nl & n \\ nlj & [..] & [..] & [..] \\ nl & [..] & [..] & [..] \\ n & [..] & [..] & [..] \end{array} \qquad (4.1)$$

Where each 'element' in this matrix is in fact a matrix partition of its own, accounting for transitions within and between the various regimes of resolution. The bundling scheme to be used for transitions within the partition structure of (4.1) is shown more formally in (4.2). Note that the bundling, when valid, implies statistical relative populations of the component members of the bundle.

$$\begin{aligned}
n_1 < n \leq n_2 \quad &: \quad N_{(\gamma_p \pi_p J_p) nlj} = \sum_J N_{(\gamma_p \pi_p J_p) nljJ} \\
&\qquad N_{(\gamma_p \pi_p J_p) nljJ} = \frac{(2J+1)}{(2J_p+1)(2j+1)} N_{(\gamma_p \pi_p J_p) nlj} \\
n_2 < n \leq n_3 \quad &: \quad N_{(\gamma_p \pi_p J_p) nl} = \sum_j N_{(\gamma_p \pi_p J_p) nlj} \\
&\qquad N_{(\gamma_p \pi_p J_p) nlj} = \frac{(2j+1)}{2(2l+1)} N_{(\gamma_p \pi_p J_p) nl} \\
n_3 < n \leq n_4 \quad &: \quad N_{(\gamma_p \pi_p J_p) n} = \sum_l N_{(\gamma_p \pi_p J_p) nl}
\end{aligned}$$

$$N_{(\gamma_p \pi_p J_p)nl} = \frac{(2l+1)}{n^2} N_{(\gamma_p \pi_p J_p)n} \tag{4.2}$$

The rates for these higher states will generally be hydrogenic expressions (or quantum defect theory based extensions of hydrogenic expressions) from a radial matrix element point of view, the main alterations being in the angular parts required to account for the new degrees of resolution and the new coupling pictures that will be used. These angular parts will be incorporated in the Gaunt factors. Thus new Gaunt factor expressions must be derived which allow for transitions between all the necessary levels of resolution (see section 4.2, with results summarised in table 4.1).

4.1.1 Definition of block structures for advanced computation

Before proceeding with the details of the newly proposed code it is useful to review and define more carefully the basic building blocks that will be used and how they carry through to the final collisional-radiative matrix.

Block primitives

As can be seen from (4.1) the most basic matrix building block is that for transitions between two levels of resolution or within a single scheme, such as $nlj \rightarrow nl$, or $nlj \rightarrow nlj$. These building blocks will be referred to as 'block primitives' analogous to the 'feature primitives' used in the spectral feature generation codes of ADAS 602-604 (Summers, 2001), and in the high series spectral feature generation work of chapter 5. The block primitive represents the foundation upon which all the C-R matrices will be built. The C-R code developed in this chapter is modularised such that each module returns a block primitive for assembly into larger C-R structures.

Blocks

We refer to the assembled structure of block primitives as 'blocks', analogous to spectral 'features'. Thus ADAS 311 run in its hydrogen setup already returns a block for transitions between $nlSL$ and nS states which contains block primitives

for $nlSL \rightarrow n'l'S'L'$, $nlSL \rightarrow n'S'$, $nS \rightarrow n'l'S'L'$ and $nS \rightarrow n'S'$. Note that it is possible to assemble these blocks to obtain larger more general collisional-radiative matrices which allow for complexities such as parent changing transitions.

Superblocks

This assembly of blocks is referred to as a 'superblock', and is analogous to the spectral 'superfeature'. A superblock might typically contain on its diagonal, block partitions in which the parent configuration does not change. The off-diagonal partitions would then contain parent changing blocks. The superblock matrix would then be solved to obtain a comprehensive population solution for the atomic system under consideration.

Description of the particular block structure for the new model

The final aim of the new model is the assembly of such a superblock. The first diagonal block will contain all the transitions within the $(\gamma\pi J)$ scheme, where there is no defined parent. The next set of diagonal blocks describe non-parent changing transitions within the $(\gamma_p\pi_p J_p)nljJ$ scheme, with the off-diagonal blocks accounting for parent changing transition within this scheme and transitions down to $(\gamma\pi J)$. As has been noted, these blocks will be assembled using the existing ADAS 208 approach. The higher diagonal elements are then blocks for non-parent changing transitions within the remaining three resolution schemes, that is blocks of the form

$$\begin{bmatrix} C_{(P)nlj\rightarrow(P)nlj} & C_{(P)nlj\rightarrow(P)nl} & C_{(P)nlj\rightarrow(P)n} \\ C_{(P)nl\rightarrow(P)nlj} & C_{(P)nl\rightarrow(P)nl} & C_{(P)nl\rightarrow(P)n} \\ C_{(P)n\rightarrow(P)nlj} & C_{(P)n\rightarrow(P)nl} & C_{(P)n\rightarrow(P)n} \end{bmatrix} \tag{4.3}$$

The neighbouring off-diagonal blocks are for parent changing transitions within these three schemes. They are negligible contributors to the population structure, allowing them to be set to zero. There only remains the first few horizontal and vertical strips accounting for transitions from the upper three schemes to the lower two. These are

filled in using the projection scheme, as already used in ADAS 208.

4.2 Gaunt factors revisited

4.2.1 Background

For this work new Gaunt factors were developed accounting for all the possible coupling schemes for the initial and final states. Gaunt factors are essentially quantum mechanical corrections on classically derived oscillator strengths. The original Gaunt factors for b-b, b-f and f-f transitions were put together in Menzel & Pekeris (1935). Efficient methods have been developed for their determination (Burgess & Summers, 1987). It is usual to evaluate the radial and angular components of the Gaunt factor separately. The bound-bound Gaunt factor is described by

$$g^I_{i,i'}(\nu,\nu') = \frac{\sqrt{3}}{\pi 2^4}\left(\frac{E-E'}{z_1^2 I_H}\right)^4 \frac{1}{\omega_\gamma} Q_{i,i'} R^I_{i,i'}(\nu,\nu') \tag{4.4}$$

where ω_γ is the statistical weight of the parent state, R is the radial integral component and Q contains the angular factors. Q and R can alse be expressed as

$$Q_{i,i'} R^I_{i,i'}(\nu,\nu') = < (S_P L_P J_P M_P) nljmJM | \underline{r} | (S'_P L'_P J'_P M'_P) n'l'j'm'J'M' > \tag{4.5}$$

The evaluation of this expression allows immediate calculation of the corresponding Gaunt factor via equation (4.4). Thus the evaluation of equation (4.5) represents the main body of work involved in the calculation of the new Gaunt factors. The bound-free and free-free Gaunt factors can be evaluated by analytically extending the bound-bound expression to free states, as in the continuity work of chapter 3.

4.2.2 Gaunt factor evaluated for j-j coupling

Consider a transition between two fully J-resolved levels, we evaluate the $Q_{i,i'} R^I_{i,i'}(\nu,\nu')$ component of the Gaunt factor and split the position vector $\underline{r}$ into its radial and spherical harmonic components. The expression that needs to be evaluated becomes

$$\langle (S_p L_p J_p) nlj JM | \underline{r} | (S'_p L'_p J'_p) n'l'j'J'M' \rangle \;=\; \langle (S_p L_p J_p) nlj JM | r Y_{1\mu} | (S'_p L'_p J'_p) n'l'j'J'M' \rangle \tag{4.6}$$

In evaluating this equation, a similar technique to the one used in the L-S coupled Gaunt factor work of Burgess & Summers (1987) is used. From appendix-A the final result is

$$\begin{aligned} & |\langle (S_P L_P J_P) nlj J || r Y_1 || (S'_P L'_P J'_P) n'l'j'J' \rangle|^2 \\ = \;& (2J+1)(2j+1)(2j'+1)(2J'+1)\delta(S_P L_P J_P; S'_P L'_P J'_P) \\ & \times | < nl|r|n'l' > |^2 \, | < l||Y_1||l' > |^2 \begin{Bmatrix} j & J & J_P \\ J' & j' & 1 \end{Bmatrix}^2 \begin{Bmatrix} j' & l' & 1/2 \\ l & j & 1 \end{Bmatrix}^2 \end{aligned} \tag{4.7}$$

Table 4.1 shows the results of this expression for various levels of bundling resolution. The tabulated values can then be used to evaluate $Q_{i,i'} R^I_{i,i'}(\nu, \nu')$, thus Gaunt factors for j-j coupled to j-j coupled levels can be calculated.

4.2.3 Cross coupling Gaunt factors evaluated

Consider a transition in which a j-j coupled level goes to an L-S coupled level or vice-versa. As the very low level treatment for the future heavy ion work may be done in an L-S coupling framework it is necessary to develop Gaunt factors that allow for these cross-coupling transitions. The method of solution follows closely with that for the j-j coupling to j-j coupling picture from the previous section, this time the expression to be evaluated is:

$$| < (S_P L_P) nlSLJ || r Y_1 || (S'_P L'_P J'_P) n'l'j'J' > |^2 \tag{4.8}$$

From appendix A this reduces to

$$= \;\; (2J+1)(2J'+1)(2S+1)(2L+1)(2j'+1)^2(2J'_P+1)$$

	$(S_P L_P J_P)n'l'j'J'$	$(S_P L_P J_P)n'l'j'$	$(S_P L_P J_P)n'l'$	$(S_P L_P J_P)n'$
$(S_p L_p J_p)nljJ$	$(2J+1)(2J'+1)(2j+1)(2j'+1)$	$(2J+1)(2j'+1)$	$\frac{(2J+1)}{(2l+1)}$	$\frac{(2J+1)}{(2l+1)}$
	$\left\{ \begin{array}{ccc} j & J & J_P \\ J' & j' & 1 \end{array} \right\}^2$	$\left\{ \begin{array}{ccc} j' & l' & 1/2 \\ l & j & 1 \end{array} \right\}^2$		
	$\left\{ \begin{array}{ccc} j' & l' & 1/2 \\ l & j & 1 \end{array} \right\}^2$			
	$\mid < l \mid\mid Y_1 \mid\mid l' > \mid^2 \mid < nl \mid r \mid n'l' > \mid^2$	$\mid < l \mid\mid Y_1 \mid\mid l' > \mid^2 \mid < nl \mid r \mid n'l' > \mid^2$	$\mid < l \mid\mid Y_1 \mid\mid l' > \mid^2 \mid < nl \mid r \mid n'l' > \mid^2$	$\sum_{l'} \mid < l \mid\mid Y_1 \mid\mid l' > \mid^2 \mid < nl \mid r \mid n'l' > \mid^2$
$(S_p L_p J_p)nlj$	$(2J'+1)(2j+1)$	$(2j'+1)(2J_P+1)(2j+1)$	$\frac{(2J_P+1)(2j+1)}{(2l+1)}$	$\frac{(2J_P+1)(2j+1)}{(2l+1)}$
	$\left\{ \begin{array}{ccc} j' & l' & 1/2 \\ l & j & 1 \end{array} \right\}^2$	$\left\{ \begin{array}{ccc} j' & l' & 1/2 \\ l & j & 1 \end{array} \right\}^2$		
	$\mid < l \mid\mid Y_1 \mid\mid l' > \mid^2 \mid < nl \mid r \mid n'l' > \mid^2$	$\mid < l \mid\mid Y_1 \mid\mid l' > \mid^2 \mid < nl \mid r \mid n'l' > \mid^2$	$\mid < l \mid\mid Y_1 \mid\mid l' > \mid^2 \mid < nl \mid r \mid n'l' > \mid^2$	$\sum_{l'} \mid < l \mid\mid Y_1 \mid\mid l' > \mid^2 \mid < nl \mid r \mid n'l' > \mid^2$
$(S_p L_p J_p)nl$	$\frac{(2J'+1)}{(2l'+1)}$	$\frac{(2j'+1)(2J_P+1)}{(2l'+1)}$	$2(2J_P+1)$	$2(2J_P+1)$
	$\mid < l \mid\mid Y_1 \mid\mid l' > \mid^2 \mid < nl \mid r \mid n'l' > \mid^2$	$\mid < l \mid\mid Y_1 \mid\mid l' > \mid^2 \mid < nl \mid r \mid n'l' > \mid^2$	$\mid < l \mid\mid Y_1 \mid\mid l' > \mid^2 \mid < nl \mid r \mid n'l' > \mid^2$	$\sum_{l'} \mid < l \mid\mid Y_1 \mid\mid l' > \mid^2 \mid < nl \mid r \mid n'l' > \mid^2$
$(S_p L_p J_p)n$	$\frac{(2J'+1)}{(2l'+1)}$	$\frac{(2j'+1)(2J_P+1)}{(2l'+1)}$	$(2J_P+1)$	$(2J_P+1)$
	$\sum_l \mid < l \mid\mid Y_1 \mid\mid l' > \mid^2 \mid < nl \mid r \mid n'l' > \mid^2$	$\sum_l \mid < l \mid\mid Y_1 \mid\mid l' > \mid^2 \mid < nl \mid r \mid n'l' > \mid^2$	$\sum_l \mid < l \mid\mid Y_1 \mid\mid l' > \mid^2 \mid < nl \mid r \mid n'l' > \mid^2$	$\sum_{ll'} \mid < l \mid\mid Y_1 \mid\mid l' > \mid^2 \mid < nl \mid r \mid n'l' > \mid^2$

Table 4.1: $(j-j)$ coupling to $(j'-j')$ coupling Q and R values evaluated for various levels of resolution.

$$\times\Sigma_x(2x+1)(-1)^{3x}\left\{\begin{array}{ccc} L & l & L_P \\ x & S & J \end{array}\right\}^2\left\{\begin{array}{ccc} 1 & l' & l \\ x & J & J' \end{array}\right\}^2$$
$$\times\left\{\begin{array}{ccc} J'_P & x & 1/2 \\ l' & j' & J' \end{array}\right\}^2\left\{\begin{array}{ccc} J'_P & 1/2 & x \\ S & L_P & S_P \end{array}\right\}^2$$
$$\times|<nl|r|n'l'>|^2|<l||Y_1||l'>|^2 \qquad (4.9)$$

As before this can be averaged to account for any desired degree of resolution.

4.3 The new collisional-radiative code

We now seek to produce a subroutine that outputs a C-R matrix for non-parent changing transitions that can be called recursively to assemble the superblock described earlier. This is done for nl and n levels of resolution and the method is tested for nlj levels.

4.3.1 nl and n resolution

For the highly excited states one has an n or nl electron on top of a J-resolved core. This is similar to the existing hydrogen mode of ADAS 311 (Summers, 2001) which assembles rates for an nl or n electron on top of a bare nucleus, solving for the populations.

To adapt the code for our purposes the parent statistical weight expression was modified to account for a J-resolved core. The code was modularised such that it returns the block primitives individually. One complication was that ADAS 311 evaluates the nearly degenerate transition rate matrix elements outside the row and column loops. It needs to do this because it uses rates from elsewhere in the matrix to evaluate the lifetimes of the levels involved in the degenerate calculations. In the new code the nearly degenerate rates are evaluated within the row and column loops, the lifetimes being estimated from the level radiative rates evaluated using hydrogenic expressions. When the code is applied to heavy species the lifetimes can be estimated from the initial autostructure run which sets up the energy level structure.

The completed hydrogen module of the code can be run for a user defined set of electron temperatures and densities. Some illustrative results are shown in figure 4.2. It was found that the new modular version of the code agreed with the previous hydrogen results from ADAS 311, and that the population results varied as expected when non-zero J_p values were used. That is, the b-factors are unaltered and the actual population values are reduced by a factor of $(2J_p + 1)$.

4.3.2 nlj resolution

A test module was constructed for the nlj part of the new code. Consider the bundled-nl and bundled-n module of the code and split one single n level into its nlj substates. The population of these nlj substates are then solved including all the transition rates between the nlj substates and those to and from the surrounding nl and n states. The hydrogen module of the code is used in a prior calculation to evaluate the surrounding populations and new rate expressions used to evaluate the connecting rates to and from the nlj substates. In this way the population distribution within an nlj set of levels can be isolated and the nlj resolved rates examined. The advantage of generating such a test module before developing a new block primitive code is that one does not need to wait until the whole block primitive module is complete before being able to test it. As future modules are added onto the collisional-radiative code it will become progressively more difficult to error check the contributions from each block primitive. There is a further point from the test module, the nlj populations for a single n shell can be used to generate a spectral emission profile which will show the distortion produced by the relative populations of the nlj sublevels and their relative energy shifts. This is an important connection with our line profile studies and is demonstrated later in this section.

Turning to the details of the test code for a whole block primitive, a perturbative type of approach is done in which from the general C-R matrix block the nl block primitive which is to be later expanded into nlj sublevels is selected. One has

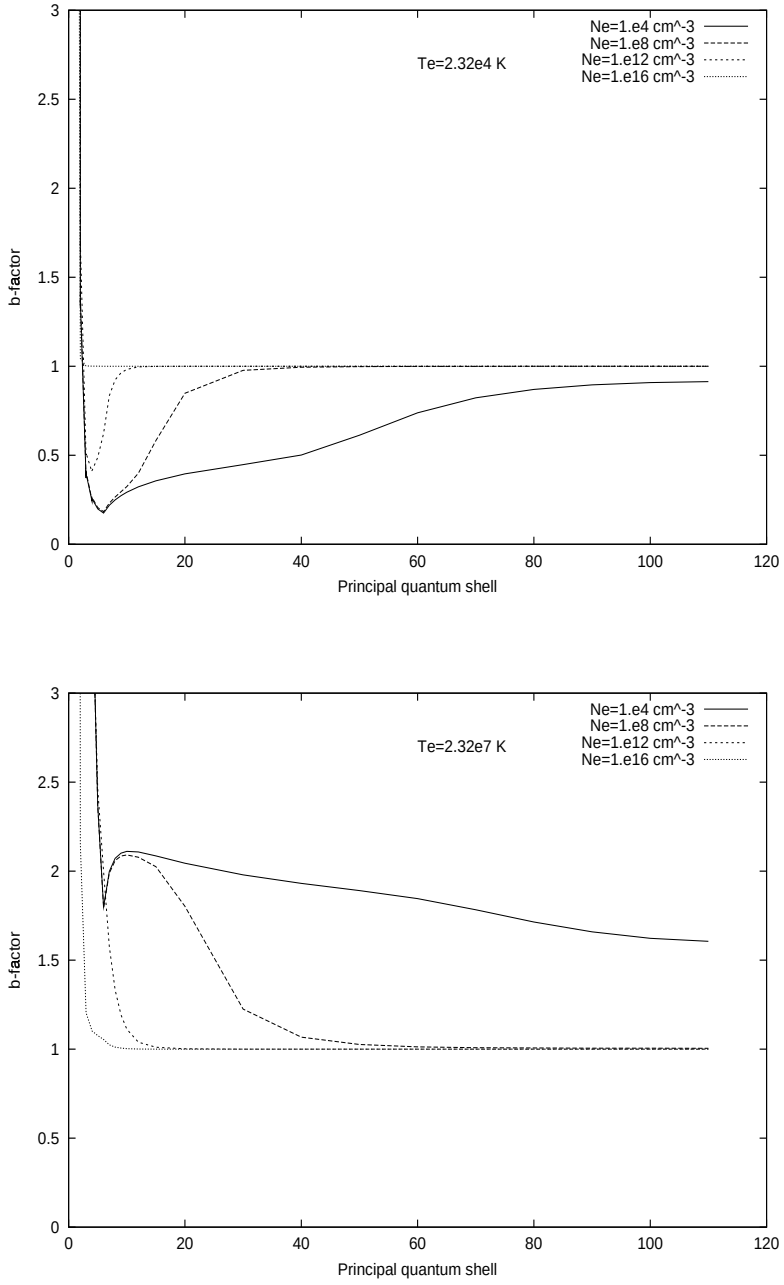

Figure 4.2: Population results from the hydrogen module of the new C-R code.

$$\left[\begin{array}{c|c|c} low\,block & \rightarrow & \rightarrow \\ \hline \leftarrow & chosen & \rightarrow \\ & nl\,block & \\ \hline \leftarrow & \leftarrow & n\,block \end{array}\right] \left[\begin{array}{c} N_1 \\ .. \\ .. \\ .. \\ .. \\ N_{max} \end{array}\right] = \left[\begin{array}{c} RHS \\ .. \\ .. \\ .. \\ .. \\ .. \end{array}\right] \tag{4.10}$$

The existing code solves the matrix equation in a b-factor picture where various atomic constants have been taken out from both the rate expressions and the atomic populations, giving

$$const \times \left[\begin{array}{c|c|c} C_{i,k'} & C_{i,n'l'} & C_{i,\bar{n}'} \\ \hline C_{nl,k'} & C_{nl,n'l'} & C_{nl,\bar{n}'} \\ \hline C_{\bar{n},k'} & C_{\bar{n},n'l'} & C_{\bar{n},\bar{n}'} \end{array}\right] \left[\begin{array}{c} b_{k'} \\ b_{n'l'} \\ b_{\bar{n}'} \end{array}\right] = \left[\begin{array}{c} RHS_k \\ RHS_{nl} \\ RHS_{\bar{n}} \end{array}\right] \tag{4.11}$$

The test code obtains the solution for the b-factors of this equation. That is,

$$\left[\begin{array}{c} b_{k'} \\ b_{n'l'} \\ b_{\bar{n}'} \end{array}\right] = \frac{1}{const} \times \left[\begin{array}{c|c|c} C_{i,k'} & C_{i,n'l'} & C_{i,\bar{n}'} \\ \hline C_{nl,k'} & C_{nl,n'l'} & C_{nl,\bar{n}'} \\ \hline C_{\bar{n},k'} & C_{\bar{n},n'l'} & C_{\bar{n},\bar{n}'} \end{array}\right]^{-1} \left[\begin{array}{c} RHS_k \\ RHS_{nl} \\ RHS_{\bar{n}} \end{array}\right] \tag{4.12}$$

One can take equation (4.11) and re-arrange it to isolate the selected nl block primitive. This is performed as follows:

$$[C_{nl,k'}]\,[b_{k'}] + [C_{nl,n'l'}]\,[b_{n'l'}] + [C_{nl,\bar{n}'}]\,[b_{\bar{n}'}] = \frac{1}{const}\,[RHS_{nl}] \tag{4.13}$$

$$\begin{aligned} [C_{nl,n'l'}]\,[b_{n'l'}] &= \frac{1}{const}\,[RHS_{nl}] - [C_{nl,k'}]\,[b_{k'}] - [C_{nl,\bar{n}'}]\,[b_{\bar{n}'}] \\ &= [new\,RHS_{nl}] \end{aligned} \tag{4.14}$$

We treat this as a new set of equations to solve for the $b_{n'l'}$ on the left hand side, the right hand side being known from the previous solution. The reorganisation can be checked by showing that the $b_{n'l'}$ results agree with their prior values.

The next step is to open up the nl block primitive into its nlj sublevels. Thus one splits each RHS_{nl} into $RHS_{nl\,l-1/2}$ and $RHS_{nl\,l+1/2}$. Similarly each b_{nl} is split into $b_{nl\,l-1/2}$ and $b_{nl\,l+1/2}$.

$$\begin{bmatrix} C_{nlj,n'l'j'} & .. & .. & .. \\ .. & .. & .. & .. \\ .. & .. & .. & .. \\ .. & .. & .. & .. \end{bmatrix} \begin{bmatrix} b_{nlj} \\ .. \\ .. \\ .. \end{bmatrix} = \begin{bmatrix} RHS_{nlj} \\ .. \\ .. \\ .. \end{bmatrix} \tag{4.15}$$

To expand the RHS for nlj resolution it is assumed that these overall rates involving the other n and nl states contribute to the nlj populations statistically. That is

$$RHS_{n\,l\,l-1/2} = \left(\frac{l}{2l+1}\right) RHS_{n\,l} \tag{4.16}$$

$$RHS_{n\,l\,l+1/2} = \left(\frac{l+1}{2l+1}\right) RHS_{n\,l} \tag{4.17}$$

A similar splitting is assumed (as a first step) for the collisional rates on the left hand side. This is justified as follows: The left hand side is made up of b-factors and rates such as spontaneous emission rates, collisional rates etc. The combination of the statistical weight in the b-factors and in the rate expression means that the collisional rates on the left hand side vary in the same way as the line strengths would. The corresponding weight terms have already been worked out in the previously evaluated Gaunt factor work. From the Gaunt factor tables, the weighting term is

$$\begin{aligned} & \frac{1}{2(2J_p+1)}(2j'+1)(2J_p+1)(2j+1) \begin{Bmatrix} j' & l' & 1/2 \\ l & j & 1 \end{Bmatrix}^2 \\ = \; & \frac{1}{2}(2j+1)(2j'+1) \begin{Bmatrix} j' & l' & 1/2 \\ l & j & 1 \end{Bmatrix}^2 \end{aligned} \tag{4.18}$$

At this point the equations can again be solved and the results should agree with $b_{n'l'l'-1/2} = b_{n'l'l'+1/2} = b_{n'l'}$. After this further check, we can proceed to include the proper rate expressions on the left hand side and evaluate the b-values for the new

nlj module (again assuming knowledge of the right hand side b_n and b_{nl} values). This test module can be used to examine the rate expressions and check limiting cases. In particular the condensation of the module by chosing representative levels can be investigated.

For the test code written here only one single n' is considered such that a distorted $n' \rightarrow n$ spectral transition can be modelled. This code is designed to be a proof that the redistributive rates can be used in the new nlj block primitive. Upon verification of this smaller test module the larger block primitive test code will be written.

So proceeding with the algebra for the smaller test module one returns to equation (4.14) and writes it out more fully in terms of all the possible n values that can appear in the nl partition. That is,

$$\begin{bmatrix} C_{n_0l_0,n_0l_0} & C_{n_0l_0,n_0+1l_1} & .. & .. \\ C_{n_0+1l_1,n_0l_0} & C_{n_0+1l_1,n_0+1l_1} & .. & .. \\ .. & .. & C_{n_cl_c,n_cl_c} & .. \\ .. & .. & .. & .. \end{bmatrix} \begin{bmatrix} b_{n_0l_0} \\ b_{n_0+1l_1} \\ b_{n_cl_c} \\ .. \end{bmatrix} = \begin{bmatrix} new\,RHS \\ .. \\ .. \\ .. \end{bmatrix} \tag{4.19}$$

Where n_cl_c represents the n-shell and corresponding l states that are to be expanded upon into nlj sub-states. Isolating the redistributive rates one is left with:

$$\begin{aligned} [C_{n_cl_c,n_cl_c}]\,[b_{n_cl_c}] &= [RHS_{n_cl_c}] - [C_{n_cl_c,n_0l_0}]\,[b_{n_0l_0}] - [C_{n_cl_c,n_0+1l_1}]\,[b_{n_0+1l_1}] - ... \\ &= [new\,RHS_{n_cl_c}] \end{aligned}$$

The procedure continues as described for a whole test block primitive. Results for $n_c = 3$ are shown here. Consider the redistributive rates. Only dipole transitions which redistribute the electrons in j are significant. There are of course ion quadrupole transition that provide J changing transition but as these are within a given nlj group they do not alter the individual j populations. Thus the main mechanism of indirect J redistribution and hence j redistribution is by transfer from $nljJ$ to $nl \pm 1j'J'$. Note that because of the near degeneracy in the relativistic picture of $nl(l+1/2)$ and $nl+1(l-1/2)$, it is only the collisional rates between $nl(l+1/2)J$ and $nl+1(l-1/2)J'$

which matter. These are allowed dipole transitions induced by positive ion impact. A code based on the theory of Pengelly & Seaton (1964) can be used to evaluate the ion collisional transition rates between adjacent l states. For an energy level separation greater than that for which the Pengelly/Seaton approach is valid, an impact parameter code (Burgess & Summers, 1976) can be used. These codes are also used in section 4.4 to evaluate bundling cut-offs.

The b_{nlj} factors evaluated for $z_0 = 36$ and $T_e = 1.05 \times 10^8 K$ (reduced temperature $T_e = 1 \times 10^5 K$) are shown as a function of density (N_e assumed equal to N_i) in figure 4.3. Note that at low densities coronal conditions apply and the populations are determined by spontaneous emission and collisional excitation from the ground. At about $1 \times 10^{22} cm^{-3}$ the j-redistributive rates become significant and couple the nearly degenerate $j = l \pm 1/2$ members of adjacent ls together. Note that the rise in the b-factors is due to population from the n=2 shell becoming significant. This was confirmed using ADAS 216. As the density increases further one would hope to see the b_{nl}-factors converging and then the b_n-factors converging. For the example shown in figure 4.3 the behaviour at higher densities is controlled by the n-shell behaviour and it was not possible to isolate the l convergence. Nevertheless the influence of the j-redistributive rates is as expected.

Distorted profiles

With the nlj non-statistical population results a distorted profile can be produced. Firstly a stick plot of the b_{nlj} factors is generated. This is then broadened using a standard Doppler profile expression to produce a distroted profile for a given $n_{upper} \rightarrow n_{lower}$ transition. Note that if the absolute populations are used along with calculated A-values and broadened profiles, an expected emission profile can be produced. We show the b-factor results here to isolate the population and energy scaling behaviour. Figure 4.4 shows a set of calculations for the $n = 3 \rightarrow 2$ transition. The plots are for a scaled density of $1 \times 10^{14} cm^{-3}$ and a scaled temperature of $1 \times 10^7 K$. Note that the energy splitting increases with z_0, resulting in a distortion of the spectral envelope. The resultant profile is normalised to one. The higher temperature than that used for figure 4.3 produces the increased b-factor values.

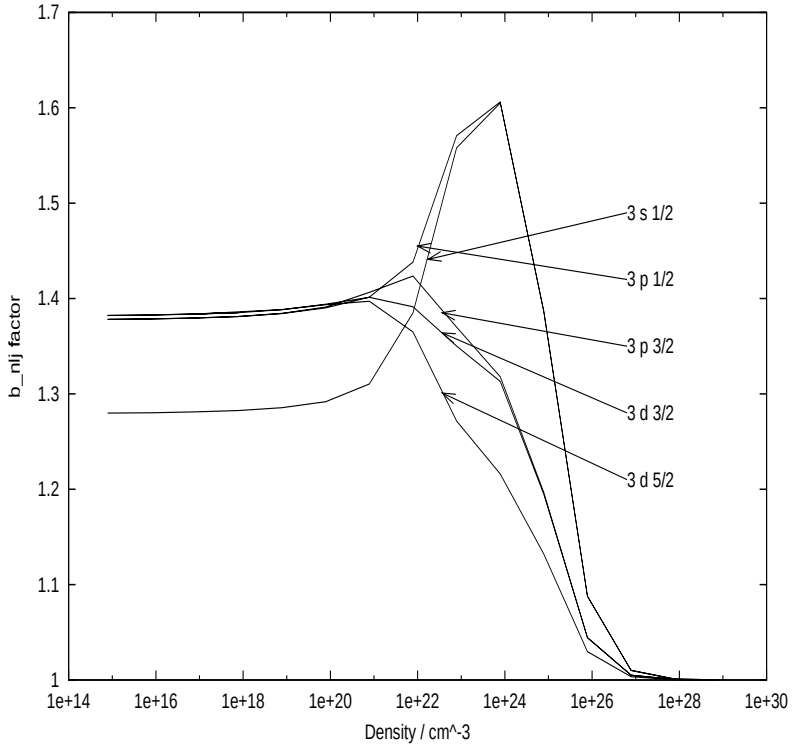

Figure 4.3: b_{nlj} results for n=3 as a function of density for $z_0 = 36$ and $T_e = 1.05 \times 10^8 K$.

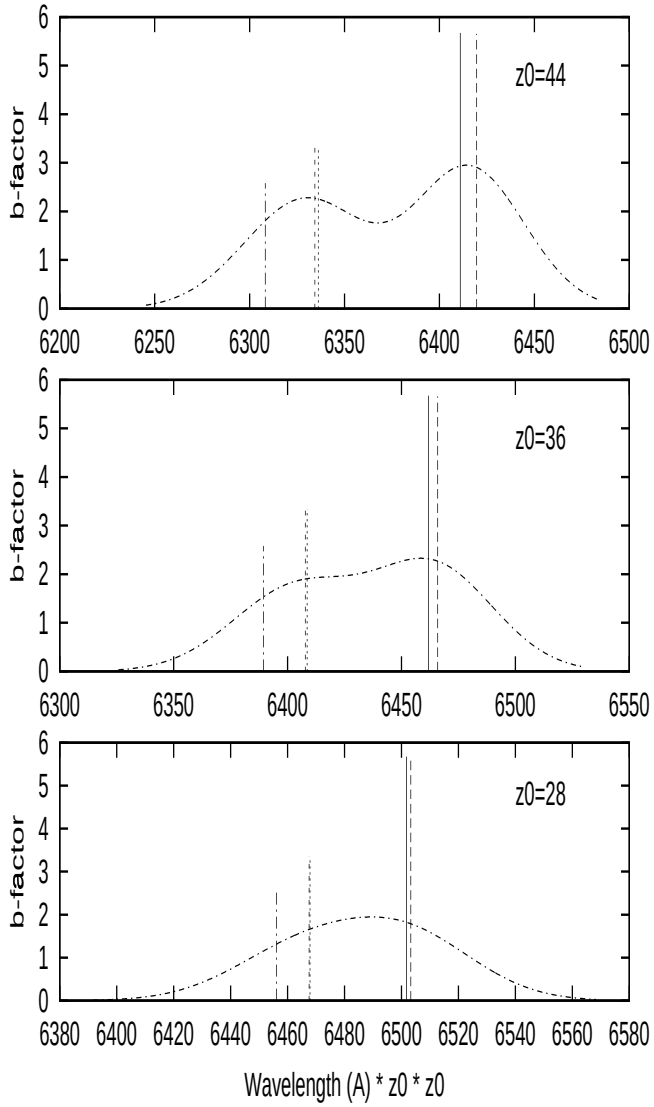

Figure 4.4: Plot showing the fine structure nlj splitting in the $n = 3 \rightarrow 2$ transition. The x-axis is the wavelength $\times z_0^2$ allowing the results for various z_0s to be plotted on the same scale. The plots are for $z_0 = 28$, 36 & 44, a reduced temperature of $1 \times 10^7 K$ and a reduced density of $1 \times 10^{14} cm^{-3}$.

4.4 Automatic detection of the bundling cut-offs

It is advantageous if the new collisional-radiative code can automatically detect the bundling cut-offs and set them appropriately. In this section the criteria for such cut-offs for the new collisional-radiative model are determined. The problem is firstly examined from an energy level perspective and then from a rate point of view.
The first step in the heavy species code is an autostructure run to determine the energy level structure. This section shows how typical autostructure data can be used in this general scheme to determine the critical n-shells between bundling regimes. Consider once more the bundling scheme of equation (4.2). It must be determined if there is indeed valid population separation in nl space of the intervals $n_0 < n \leq n_1$ and $n_1 < n \leq n_2$ for bundling to be appropriate. Consider this firstly from the energy level point of view.

4.4.1 Energy level investigation

The relativistic separations of the valence electron fine structure levels from the nl centroid, taken from Condon & Shortley (1935), are given by

$$\begin{aligned} \Delta E_{nl_{l+1/2}} &= \frac{z_1^4 \alpha^2 R_\infty}{n^4} \left(\frac{n}{(l+1)} - \frac{n}{(l+1/2)} \right) \\ \Delta E_{nl_{l-1/2}} &= \frac{z_1^4 \alpha^2 R_\infty}{n^4} \left(\frac{n}{l} - \frac{n}{(l+1/2)} \right) \end{aligned} \tag{4.20}$$

where z_1 is the ion charge $+1$, α is the fine structure constant and R_∞ is the Rydberg energy unit. By contrast, the J separation arises from the electrostatic interaction of the valence electron with the parent core. The interaction is diagonal in J with the level separations from the $(J_p)nlj$ centroid expressible in the form

$$\begin{aligned} \Delta E_{nl_j J} &= \sum_i (f_{2i} F_{2i} + g_{2i} G_{2i}) \\ &= \frac{z_1 R_\infty}{n^3} \sum_i (f_{2i} \bar{F}_{2i} + g_{2i} \bar{G}_{2i}) \end{aligned} \tag{4.21}$$

where the "barred" quantities are weakly dependent on z_1 and n and the fs, $\bar{F}$s and $\bar{G}$s are of order unity. The $\bar{F}$s and $\bar{G}$s are the usual slater integrals.

Consider a critical energy splitting ΔE_c which is the minimum level separation required for two levels to be resolved. This critical energy separation is determined from the ion collision rates and is the mimimum energy separation required for ion collisions to statistically populate the energy levels for the temperature and density of interest. Thus a critical n-shell n_2 will occur above which j levels are statistically populated. Similarly there will be a critical n-shell n_1 above which the J levels are statistically populated. For the proposed bundling to be appropriate we require $n_2 > n_1$. Taking the ratio of equation (4.20) to (4.21) one can see that this separation of bundling intervals $n_0 < n \leq n_1$ and $n_1 < n \leq n_2$ is appropriate if

$$\frac{n_2}{n_1} \sim z_1 \alpha^{2/3} > 1 \tag{4.22}$$

Energy scaling example - Carbon-like isoelectronic sequence

An illustration of the energy level scaling for the Carbon-like sequence is shown below. The superstructure code (Eissner et al., 1974) was used to generate an energy level structure for the C-like sequence with a valence electron that could be placed in a range of n and l shells. The core configuration was held constant at $1s^2 2s^2 2p$ and the Rydberg electron added on top of this configuration. The core configuration thus generated two possible parent states, namely $^2P_{1/2}$ and $^2P_{3/2}$. The energy splitting between these states is expected to be significantly stronger than the j or J fine structure splitting and should scale as z_1^4/n^3. For each parent configuration we have the further splitting into two possible j states with $j = l + 1/2$ or $j = l - 1/2$, since there is only one outer electron to form the l and s quantum numbers to give us the resultant j for the valence electron. This energy level splitting is expected to scale as in equation (4.20). There exists a further possible energy splitting due to the total J quantum number and this should scale as in equation (4.21). For our C-like sequence we have the following possible total J quantum numbers.

Parent	n	l	j	J			
$^2P_{1/2}$	n	l	$l-1/2$	l	$l-1$		
$^2P_{1/2}$	n	l	$l+1/2$	$l+1$	l		
$^2P_{3/2}$	n	l	$l-1/2$	$l+1$	l	$l-1$	$l-2$
$^2P_{3/2}$	n	l	$l+1/2$	$l+2$	$l+1$	l	$l-1$

It is expected that the largest energy splitting will be between parent states, followed by the j splitting and then the J separation. If everything scales as expected then it will be possible to predict the bundling cut-offs and assemble the collisional-radiative matrix elements as intended.

Three superstructure runs were performed in order to verify the energy scaling. For all runs the option was used to specify a core configuration and add on a Rydberg electron. The code returned the energy level values in Rydberg units with respect to the lowest level defined. Only a single core configuration was specified in order to isolate the various energy splittings. The first run was performed using a 5f Rydberg electron and z_1 was varied from 1 to 85. For the second run z_1 was held constant at 67 to allow sufficient resolution of the splitting to be generated and n varied from 4 to 16. Lastly with $z_1 = 72$ and $n = 13$, l was varied from 2 through to 10. It was possible from these runs to verify the z_1, n and l behaviour of the resolved energy level splittings as defined in equations (4.20) and (4.21). Note that it is this scaling behaviour that is sought here, not the evaluation of exact energy level values, hence there is no need for a more complex atomic structure to be entered into the superstructure code.

Considering first the parent energy level splitting. In figures 4.5 - 4.6 we show the z_1 and n behaviour of the parent splitting. The z_1 scaling is as expected i.e. z_1^4 for high z_1. As for the n-dependence, the parent energy splitting initially falls off sharply with n and then remains constant. It should be noted that the magnitude of the parent splitting is significantly greater that either the j or J splitting (compare the absolute energy difference values of figure 4.5 with those of figures 4.7 - 4.18).

The behaviour of the E_{nlj} fine structure level from the E_{nl} centroid, i.e. equation (4.20) was then investigated. Taking the results from the z_1 run it can be seen from figure 4.7 that the splitting varies as z_1^4 for all possible j values. As for the

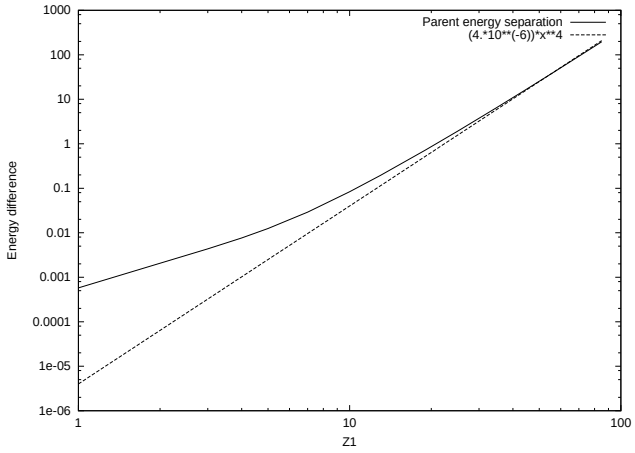

Figure 4.5: $E_{^2P_{1/2}}$ separation from $E_{^2P_{3/1}}$ centroid - z_1 dependence. Note that the energy splitting varies as z_1^4 for high z_1 as expected.

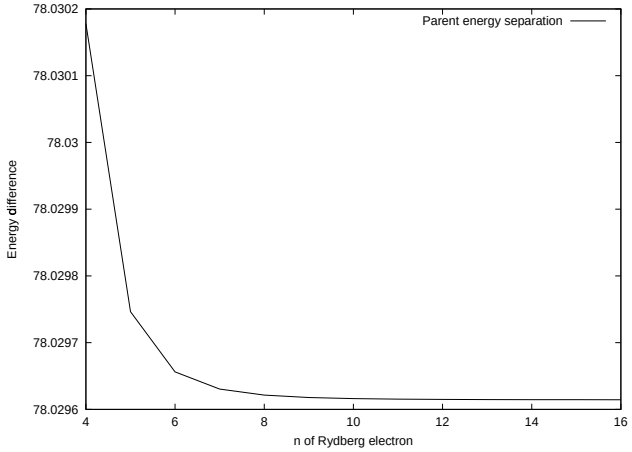

Figure 4.6: $E_{^2P_{1/2}}$ separation from $E_{^2P_{3/1}}$ centroid - n dependence.

n-dependence it can be seen in figure 4.8 that for both parents the splitting scales as $1/n^3$. The l-dependence is shown in figures 4.9 - 4.10. It can be seen that the splitting does indeed vary exactly as predicted in equation (4.20), note in particular that the constant of proportionality is also as expected.

Consider next the E_{nljJ} splitting from the E_{nlj} centroid as predicted by equation (4.21). Taking first the z_1-dependence one can see from figures 4.11 - 4.13 that the energy differences are indeed linear with z_1. The n-dependence is shown in figures 4.14 - 4.16 and is seen to scale as $1/n^3$.

The l behaviour is not so straightforward, the energy difference splits into two main groups defined by the $j = l - 1/2$ and $j = l + 1/2$ states (see figures 4.17 - 4.18). For low l there is a high degree of variance in the ΔE_{nljJ} behaviour, as expected due to the penetration of these orbitals into the core. As one increases to higher l the behaviour becomes smooth, scaling approximately as $1/l^3$ for the case of the $^2P_{3/2}$ parent. In both cases the splitting clearly falls off with increasing l.

From this worked example it can be seen that expressions (4.20) and (4.21) are indeed valid. Thus it is also possible to asses the n_2/n_1 ratio shown in equation (4.22) for the C-like case. Figures 4.19 - 4.22 show the ratio of ΔE_{nljJ} to ΔE_{nlj}. From equations (4.20) and (4.21) it can be seen that this ratio is equivalent to n_2/n_1. As expected from equation (4.22), the ratio becomes greater than one around $z_1 = 20$. That is, the choice of level bundling into the specified regions is valid for approximately $z_1 > 20$. This value varies for the different possible j values as can be seen from figures 4.19 - 4.22.

From the C-like superstructure data it was also possible to decide on the critical n values for each bundling region. If one specifies a critical energy difference (ΔE_c) above which bundling is no longer appropriate, n_1 and n_2 can be inferred from equation (4.22). For example using the energy splitting values of the $E_{^2P_{3/2}n(l-1/2)}$ and $E_{^2P_{3/2}n(l-1/2)J=4}$ levels and a $\Delta E_c = 0.01Ry$ the bundling cut-offs are at $n_1 = 4$ and $n_2 = 15$.

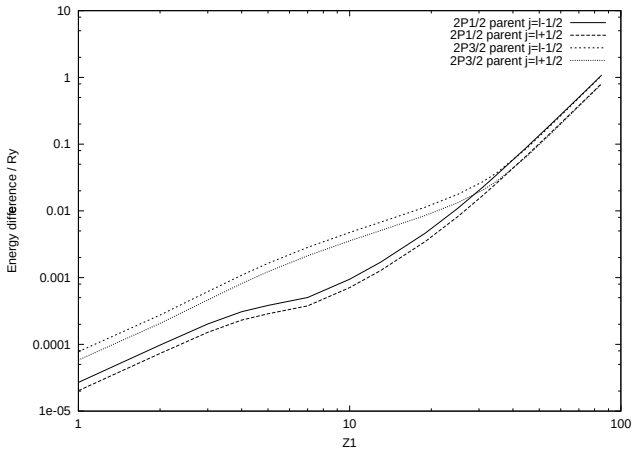

Figure 4.7: E_{nlj} separation from E_{nl} centroid - z_1 dependence. Note that the energy splitting varies as z_1^4 for high z_1 as predicted in equation (4.20). An electronic configuration of $1s^2 2s^2 2p\,(^2P_{1/2})5f$ was used throughout the superstructure run.

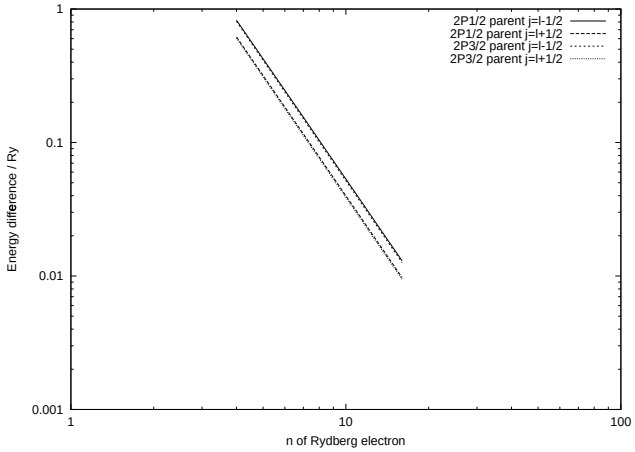

Figure 4.8: E_{nlj} separation from E_{nl} centroid - n dependence. The energy splitting varies as $1/n^3$ as expected from equation (4.20). An l value of 3 for the outer electron was used throughout the n dependence run. z_1 was held constant at 72 to ensure that there was sufficient level splitting at high n to be resolved.

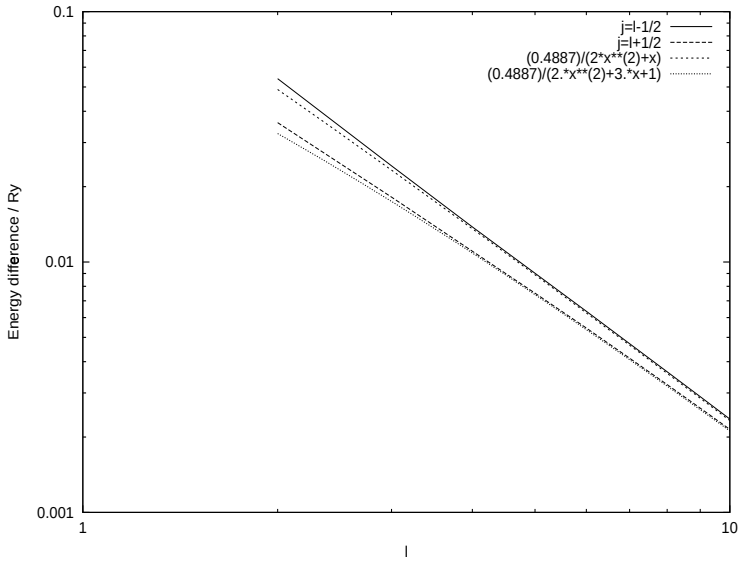

Figure 4.9: E_{nlj} separation from E_{nl} centroid for $^2P_{1/2}$ parent - l dependence. The energy splitting varies exactly as predicted from equation (4.20). An n value of 13 was used for the autostructure run and l varied from 2 through to 10. z_1 was again held constant at 72 to ensure that there was sufficient level splitting to be resolved.

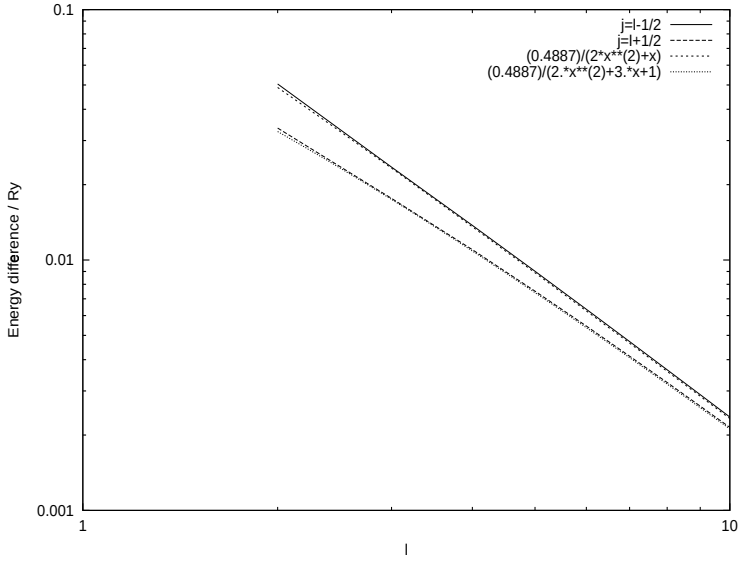

Figure 4.10: E_{nlj} separation from E_{nl} centroid for $^2P_{3/2}$ parent - l dependence. The energy splitting varies exactly as predicted from equation (4.20). An n value of 13 was used for the autostructure run and l varied from 2 through to 10. z_1 was again held constant at 72 to ensure that there was sufficient level splitting to be resolved.

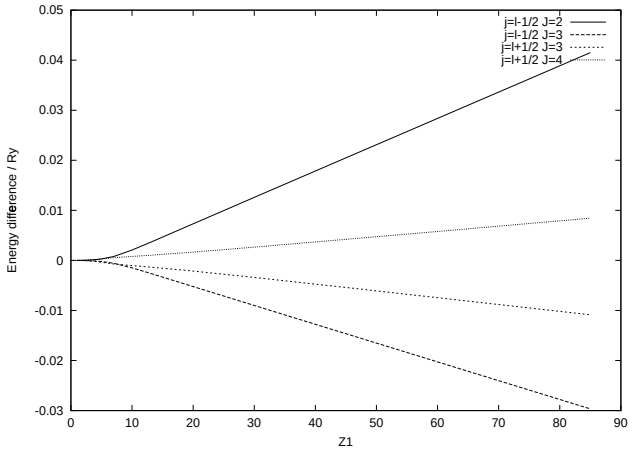

Figure 4.11: E_{nljJ} separation from E_{nlj} centroid for $^2P_{1/2}$ parent - z_1 dependence.

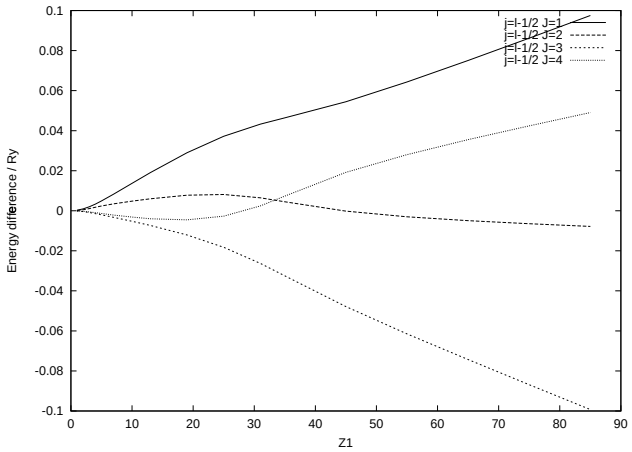

Figure 4.12: E_{nljJ} separation from E_{nlj} centroid for $^2P_{3/2}$ parent $j = (l - 1/2)$ - z_1 dependence.

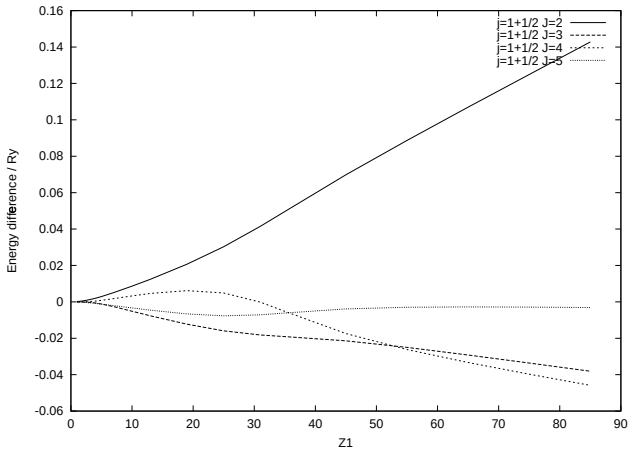

Figure 4.13: E_{nljJ} separation from E_{nlj} centroid for $^2P_{3/2}$ parent $j = (l + 1/2)$ - z_1 dependence.

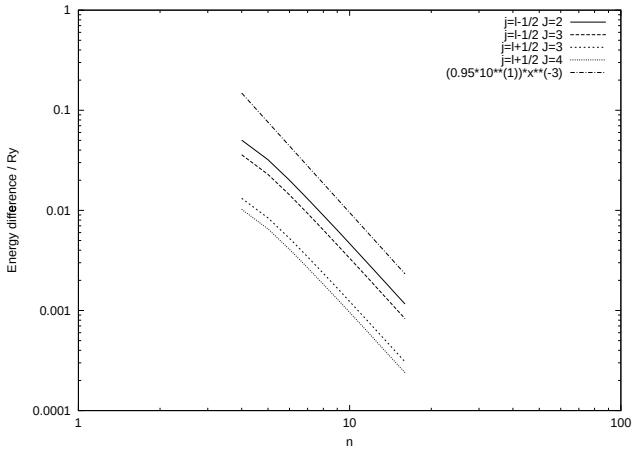

Figure 4.14: E_{nljJ} separation from E_{nlj} centroid for $^2P_{1/2}$ parent - n dependence.

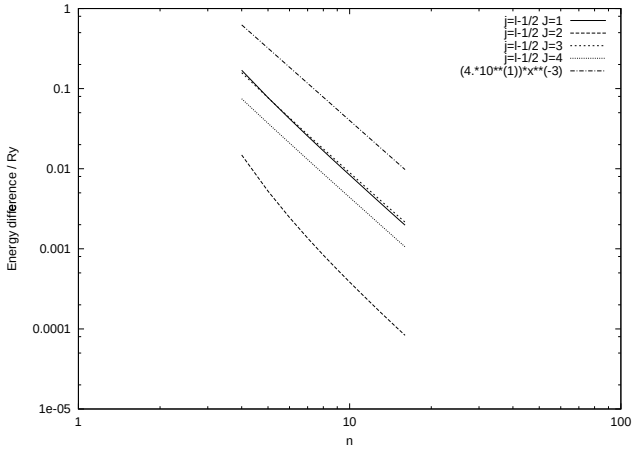

Figure 4.15: E_{nljJ} separation from E_{nlj} centroid for $^2P_{3/2}$ parent j=l-1/2 state - n dependence.

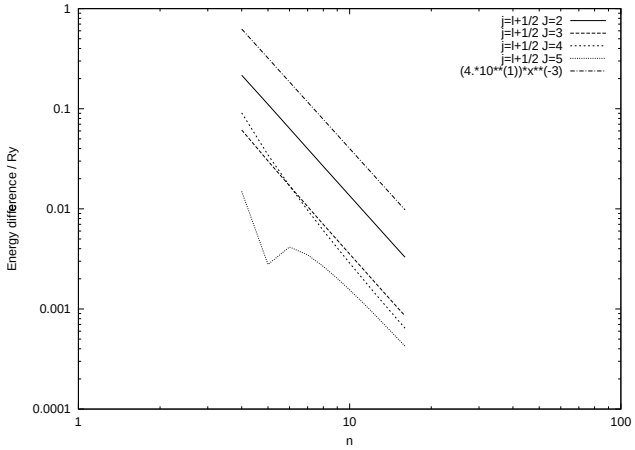

Figure 4.16: E_{nljJ} separation from E_{nlj} centroid for $^2P_{3/2}$ parent j=l+1/2 state - n dependence.

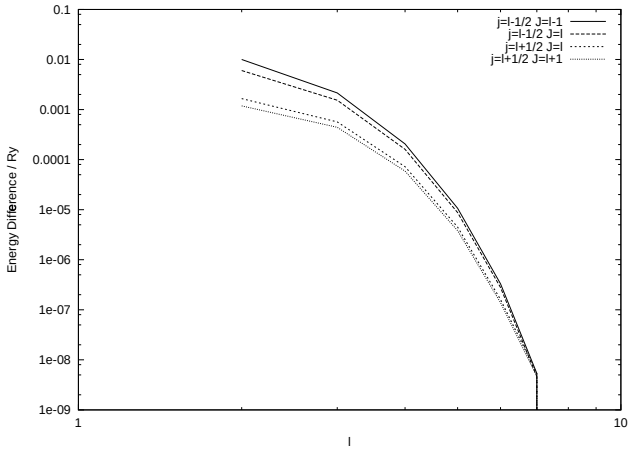

Figure 4.17: E_{nljJ} separation from E_{nlj} centroid for $^2P_{1/2}$ parent - l dependence.

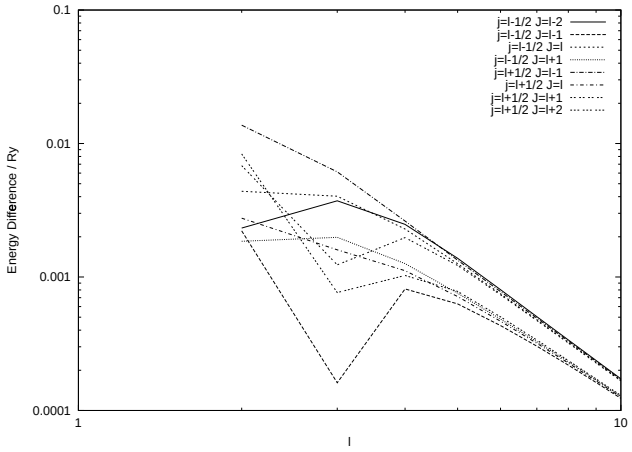

Figure 4.18: E_{nljJ} separation from E_{nlj} centroid for $^2P_{3/2}$ parent - l dependence.

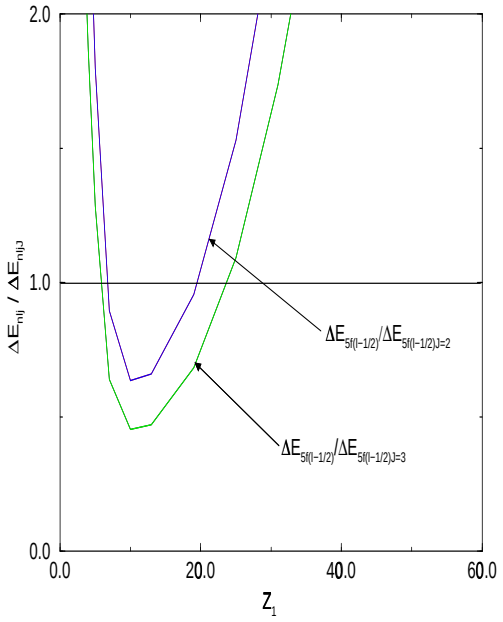

Figure 4.19: $\Delta E_{nljJ}/\Delta E_{nlj}$ for $^2P_{1/2}$ parent, j=l-1/2.

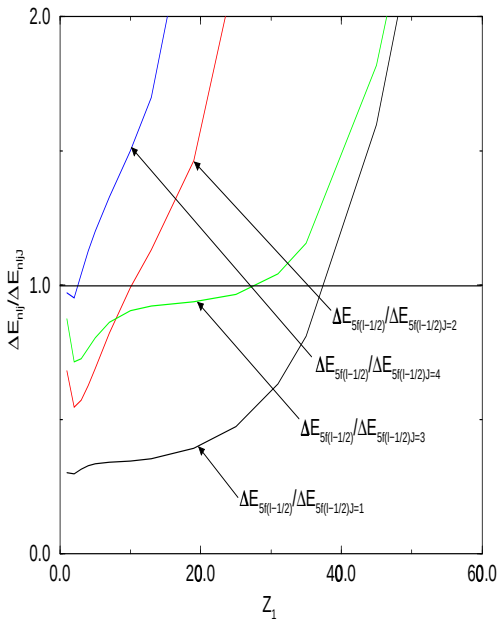

Figure 4.20: $\Delta E_{nljJ}/\Delta E_{nlj}$ for $^2P_{3/2}$ parent, j=l-1/2.

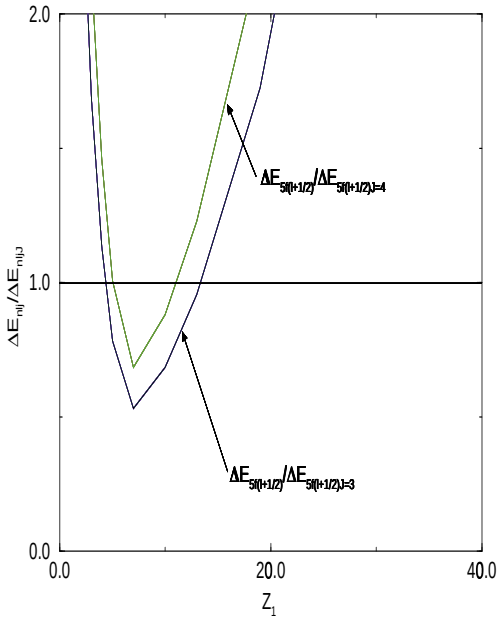

Figure 4.21: $\Delta E_{nljJ}/\Delta E_{nlj}$ for $^2P_{1/2}$ parent, j=l+1/2.

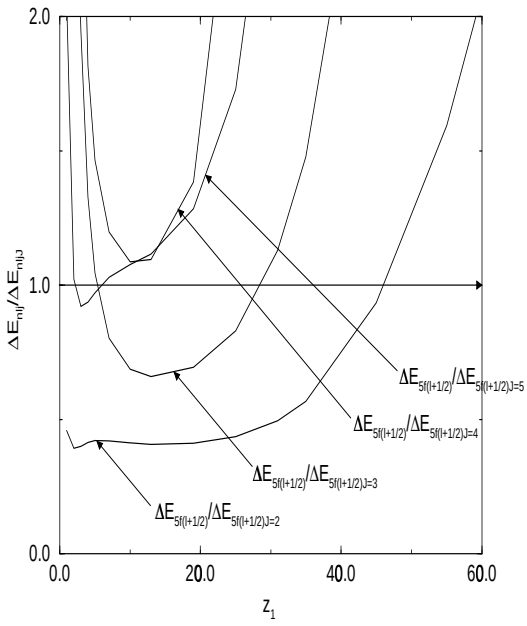

Figure 4.22: $\Delta E_{nljJ}/\Delta E_{nlj}$ for $^2P_{3/2}$ parent, j=l+1/2.

4.4.2 Collisional redistribution evaluated

It has been seen that the energy splitting of a given atomic system can be predicted. Of course the actual source of the levels becoming statistically populated (with respect to each other) is that ion collisions redistribute the electrons within a given set of levels faster than they can decay through spontaneous emission. These ion collisions are strongly dependent upon the energy level splitting, and thus it is important to be able to track the splitting for any system being investigated, as in the previous section. To ensure that the levels are statistically populated one must look at the actual collisional rates. There are two main collisional rates that can redistribute the electrons amongst the J levels of a given $(J_P)nlj$ group that must be considered for the n_1 cut-off to be diagnosed. The first process is collisionally induced quadrupole transitions between members of the $(J_P)nlj$ group, and the second is dipole transitions from adjacent l states.

Quadrupole transitions within the one $(J_P)nlj$ group

Consider a set of J levels within a given parent and j. The critical density at which the J-levels will be relatively statistically populated will be given by

$$N_{c_1}^{(zeff)} =< A_J > / << q_{J\rightarrow J'}^{(zeff)}(T^{(zeff)}) >> \tag{4.23}$$

where $< A_J >$ denotes the average over J of the level reciprocal radiative lifetime and $<< q_{J\rightarrow J'}^{(zeff)} >>$ denotes the rate coefficient summed over final states J' and averaged over initial states J. Note that this is for transitions between J populations of the same $(J_P)nlj$ group.

It was possible to evaluate the ion collisional redistribution rate using a code based on the theory given in Alder et al. (1956). The code was taken from the ADAS database of codes at JET and was originally developed by Summers. The code was originally designed to model proton collisional rates for any given target. It was possible to scale the proton collisional cross sections to apply to any colliding ion. This is shown briefly below.

Cross section scaling for heavy ions

The proton collisional cross sections scale in a straightforward manner to the cross sections for ion collisions. The ion collisional rate, $q(T_i)$, is found from the cross section $\sigma_i(v)$. Assuming a Maxwellian velocity distribution for the colliding ions $q(T_i)$ is given by

$$\begin{aligned} q(t_i) &= \int_0^\infty 4\pi \left(\frac{m_i}{2\pi k T_i}\right)^{3/2} v^2 e^{\frac{mv^2}{2kT_i}} v\sigma_i(v)dv \\ &= \int_{E_0}^\infty 8\pi \left(\frac{m_i}{2\pi k T_i}\right)^{3/2} \frac{1}{2} m_i v^2 m_i^{-\frac{1}{2}} \sigma_i(v) dE \end{aligned} \tag{4.24}$$

The ion collisional cross sections are equal to ${z_i}^2$ (the effective charge of the collider) times the proton collisional cross section evaluated at the same velocity. That is if E_p is the proton energy and E_i is the ion energy, then

$$\begin{aligned} E_i &= \frac{1}{2} m_i v^2 \\ &= \frac{1}{2} m_i \frac{E_p}{\frac{1}{2} m_p} \\ &= \frac{m_i}{m_p} E_p \end{aligned} \tag{4.25}$$

Thus

$$\sigma_i(E_i) \rightarrow z_i^2 \sigma_p(E_p) \tag{4.26}$$

Therefore

$$\begin{aligned} q(T_i) &= \int_{E_0}^\infty \frac{8\pi}{m_i^{\frac{1}{2}}} \left(\frac{1}{2\pi k T_i}\right)^{3/2} E_i e^{\frac{E_i}{kT_i}} z_i^2 \sigma_p(E_p) dE_i \\ &= \int_{E_0}^\infty \frac{8\pi}{m_i^{\frac{1}{2}}} \left(\frac{1}{2\pi k T_i}\right)^{3/2} \frac{m_i}{m_p} E_p e^{\frac{m_i}{m_p}\frac{E_p}{kT_i}} z_i^2 \sigma_p(E_p) \frac{m_i}{m_p} dE_p \\ &= \int_{E_0}^\infty \frac{8\pi}{m_p^{\frac{1}{2}}} \left(\frac{1}{2\pi k \left(\frac{m_p}{m_i} T_i\right)}\right)^{3/2} E_p e^{\frac{E_p}{k\left(\frac{m_p}{m_i} T_i\right)}} z_i^2 \sigma_p(E_p) dE_p \\ &= z_i^2 q_p(T_p) \end{aligned} \tag{4.27}$$

where

$$T_p = \frac{m_p}{m_i} T_i \tag{4.28}$$

is the scaled proton temperature. Thus in order to run the code for any possible collider, one has to evaluate the proton temperature at this scaled temperature and multiply the cross section by z_i^2.

The C-like sequence was used to illustrate the behaviour of $N_{c_1}^{(zeff)}$ for the electric quadrupole transitions. The superstructure code (Eissner et al., 1974) was run to generate the fundamental atomic data required to evaluate these rates. The system was restricted to two allowed configurations, namely

- $1s^2 2s^2 2p^2$
- $1s^2 2s^2 2p : nd$

where nd represents the Rydberg electron that could be placed in a range of n-shells. The possible J-values that the system can take are shown in table 4.4.2.

Configuration	Parent	j	possible J
$1s^2 2s^2 2p^2$	$^2P_{1/2}$	3/2	2,1
$1s^2 2s^2 2p^2$	$^2P_{1/2}$	1/2	1,0
$1s^2 2s^2 2p^2$	$^2P_{3/2}$	3/2	3,2,1,0
$1s^2 2s^2 2p^2$	$^2P_{3/2}$	1/2	2,1
$1s^2 2s^2 2p : nd$	$^2P_{1/2}$	5/2	3,2
$1s^2 2s^2 2p : nd$	$^2P_{1/2}$	3/2	2,1
$1s^2 2s^2 2p : nd$	$^2P_{3/2}$	3/2	3,2,1,0
$1s^2 2s^2 2p : nd$	$^2P_{3/2}$	5/2	4,3,2,1

For the purposes of evaluating the ion collisional rates, it was decided to look at the $1s^2 2s^2 2p(^2P_{3/2})$, $j = l - 1/2$ set of levels to see at which point the ion collisions balance the spontaneous emission rate. With the configuration chosen it is possible to get electric quadrupole transitions between the J levels of this group and dipole allowed spontaneous emission to any of the ground configuration terms allowed for within the

$\Delta J \leq 1$ selection rule (as there will alway be a change of parity between the Rydberg electron configuration and the ground). For the highly excited electrons, there will also exist many other spontaneous emission decay routes that are not accounted for within the simple atomic structure chosen for the superstructure runs. Thus it was decided to evaluate hydrogenic A-values for each $1s^2 2s^2 2p : nd$ set of levels. In this way a more accurate lifetime could be calculated for use in equation (4.23).

The ion collision code needs to know the energy values, electric quadrupole line strengths and the statistical weights for each level involved in the transition as well as the effective charge of the projectile and ion temperature of the plasma. The superstructure code was run to get the energy level values and the electric quadrupole line strengths. This was done for a range of n-shells, z_1's and ion temperatures. Alpha particles were used as the colliders to illustrate the results in the context of a fusion tokamak.

To evaluate equation (4.23) it was then necessary to form the various averages. $< A_J >$ was calculated by finding the average over J of the total spontaneous emission rates from each level. Similarly $<< q^{(zeff)}_{J \rightarrow J'}(T^{(zeff)}) >>$ was found by taking the average over J of the total ion collisional rate (excitation and de-excitation) from each J to all the other possible J levels in the j=l-1/2 set of levels. The results are shown in figures 4.23 - 4.26.

It can be seen that the average A-values increase with z_1 and falls off with increasing n. This is as expected due to the excited electron being held closer to the core for high z_1, thus allowing for stronger decay to the lower states. Similarly for higher n, the electrons are further from the core and so less likely to decay.

Note that the critical density scaling is as expected with $N^{(zeff)}_{c_1}$ increasing with z_1 and decreasing as one progresses up the various n-shells. It can also be seen that for a light element of $z_1 \approx 1$ and $n \approx 15$, the critical density for statistical redistribution in J occurs at a reasonable value ($N_{c_1} \approx 1 \times 10^{10} cm^{-3}$).

In order to evaluate the critical n-shell above which the levels are statistically populated we plot $< A_J > /(<< q^{(zeff)}_{J \rightarrow J'}(T^{(zeff)}) >> N_{ion})$, see figure 4.27 for the results. The critical n-shell is the one at which the curves cross 1. The plot shows the results for a range of effective nuclear charges. The results are as one would expect, with

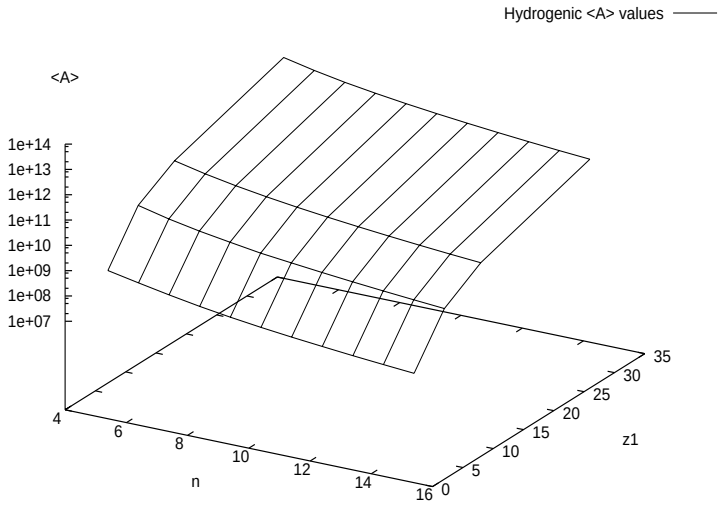

Figure 4.23: A-values for the range of physical parameters that the autostructure code was run, n and z_1 dependence.

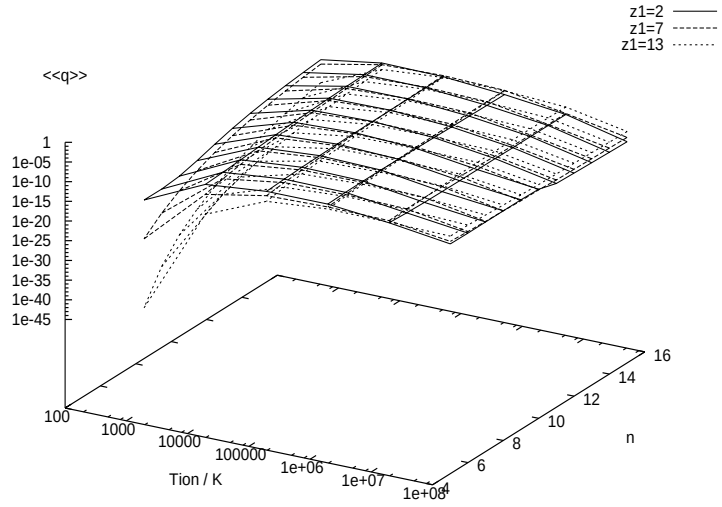

Figure 4.24: Ion quadrupole collisional rates as a function of temperature and n-shell.

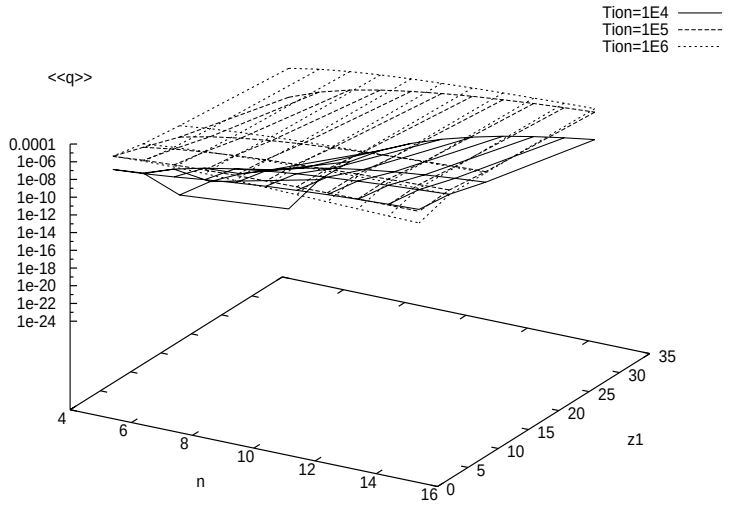

Figure 4.25: Ion quadrupole collisional rates as a function of n-shell and z_1.

$n \approx 9$ for $z_1 = 2$ and $n \approx 15$ for $z_1 = 7$.

Dipole allowed transitions between adjacent l states

There is a second mechanism of indirect J redistribution by transfer from $nljJ$ to $nl \pm 1j'J'$. Note that because of the near degeneracy in the relativistic picture of $nl_{l+1/2}$ and $nl+1_{l-1/2}$, it is only the collisional rates between $nl_{l+1/2}J$ and $nl+1_{l-1/2}J'$ which matter. These are allowed dipole transitions but again induced by positive ion impact. The critical density for redistribution by this pathway is

$$N_{c_1}^{(zeff)} =< A_J > / << q_{nlJ \to nl \pm 1J'}^{(zeff)}(T^{(zeff)}) >> \tag{4.29}$$

The critical density for J redistribution is the smaller of the N_{c_1} values from equations (4.23) and (4.29). Alternatively, for specified $N^{(zeff)}$ in the plasma, we seek the lowest value of n $(= n_1)$ for $l > 1$ for which the equalities are acceptably satisfied.
Transitions from $nljJ$ to $nl \pm 1j'J'$ levels were evaluated for the C-like sequence to illustrate the critical density and n-shell behaviour. For the rates, the same code

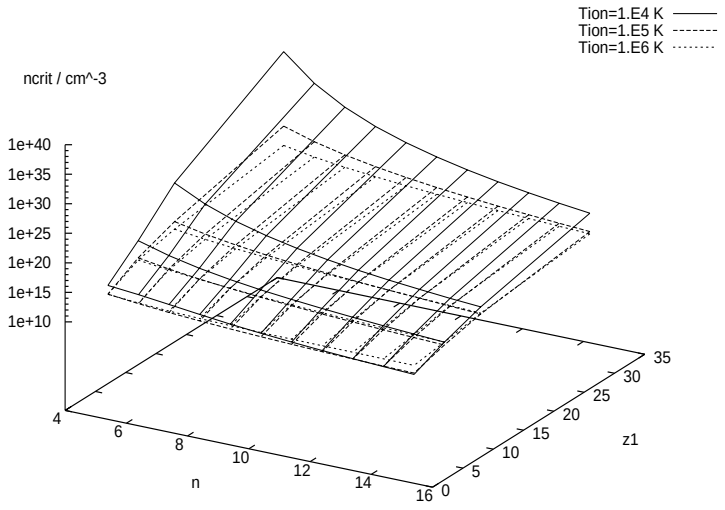

Figure 4.26: Critical density at which the ion quadrupole collisions balance the spontaneous emission rates from the j=l-1/2 set of levels.

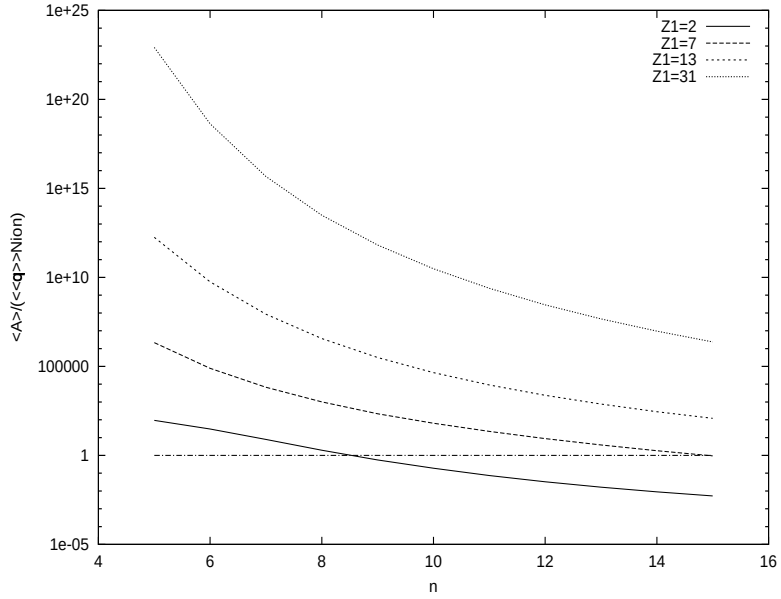

Figure 4.27: Critical n-shell plot showing the critical value at which the ion collisions balance the spontaneous emission rates from the j=l-1/2 set of levels. A collider density of $1 \times 10^{14} cm^{-3}$ and temperature of $1 \times 10^{4} K$ were used.

as that for the nlj test code was used. The superstructure code was again run to generate the atomic data necessary for the code. An atomic structure of $1s^2 2s^2 2p : nl$ was used, this time the Rydberg electron was allowed to occupy either the p, d or f states and make transitions between them or alternatively down to the ground $1s^2 2s^2 2p^2$ configuration. Results were generated for a range of n-shells and nuclear charges.

The Pengelly/Seaton code requires energy level values, absorption oscillator strengths, statistical weights, all of which were extracted from the superstructure runs. The code also requires initial and final state lifetimes. Due to the simple atomic structure used in the superstructure runs, there were many spontaneous decay routes which were not accounted for. To allow for realistic lifetimes to be produced, hydrogenic A-values were again generated for each level of interest, accounting for decay to all possible lower states. In this way the $nd\ ^2P_{1/2}$ set of levels were investigated, considering all the possible dipole collisional transitions to and from the adjacent l states, and spontaneous decay to all allowed lower states.

The $< A_J >$ and $<< q >>$ values are shown in figures 4.28 and 4.29, and both scale as one would expect. The critical density at which statistical redistribution occurs was plotted for a range of n and z_1 values, see figure 4.30. As can be seen, there is a straightforward increase of the critical density with z_1, and a decrease with n. There is also a slight increase with collider temperature, with the ion collisions becoming less effective at higher temperatures. The critical n-shell at which redistribution occurs was also plotted for a range of z_1's, see figure 4.31. As before, the results are intuitive and verify the proposed bundling method with statistical redistribution occurring at $n \approx 5$ for $z_1 = 2$ and $n \approx 12$ for $z_1 = 7$.

Thus one can see that it is possible in principal to evaluate the n_1 cut-off for any medium/heavy element.

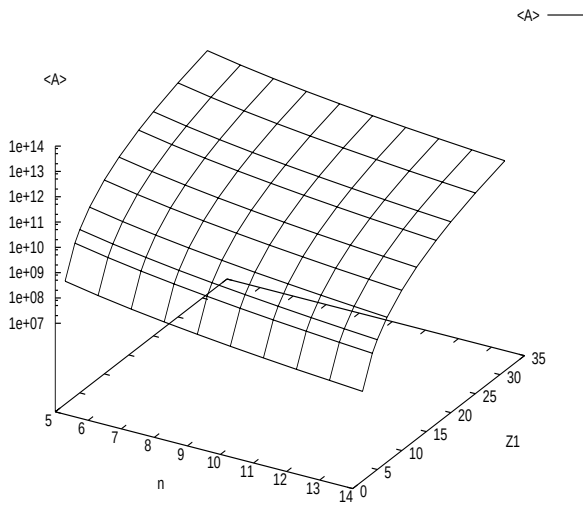

Figure 4.28: $< A_J >$ evaluated for the C-like system for the $1s^2 2s^2 2p : nd$ set of levels.

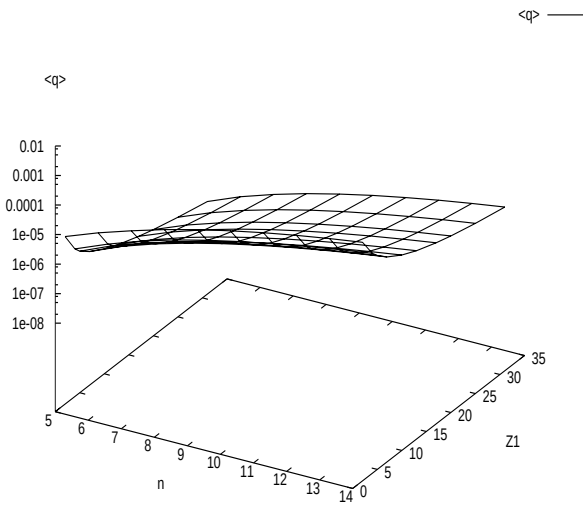

Figure 4.29: $<< q^{(zeff)}_{nlJ \to nl \pm 1J'}(T^{(zeff)}) >>$ evaluated for the C-like system for the $1s^2 2s^2 2p : nd$ set of levels for a collider temperature of $1 \times 10^4 K$.

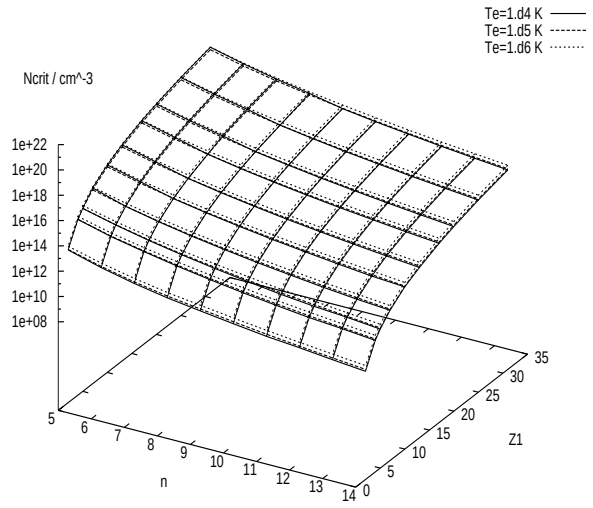

Figure 4.30: $< A_J > /(<< q^{(zeff)}_{nlJ \rightarrow nl \pm 1 J'}(T^{(zeff)}) >>)$ evaluated for the C-like system for the $1s^2 2s^2 2p : nd$ set of levels.

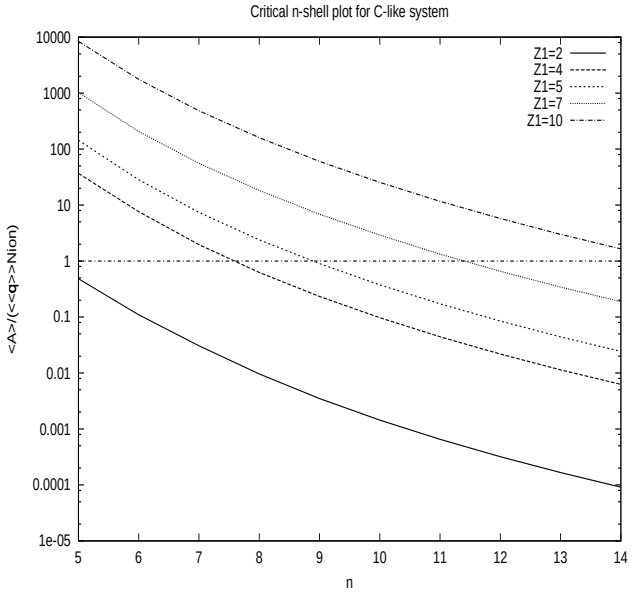

Figure 4.31: $< A_J > /(<< q^{(zeff)}_{J \rightarrow J'}(T^{(zeff)}) >> N_{ion})$ evaluated for the C-like system for the $1s^2 2s^2 2p : nd$ set of levels. A collider density of $1 \times 10^{14} cm^{-3}$ and temperature of $1 \times 10^4 K$ were used for all the results shown.

4.5 Conclusions

In this chapter much of the ground work for the new collisional-radiative code for application to heavy elements has been laid down. The new bundling scheme has been described and a code developed for the bundled-nl and bundled-n block primitives. A test module to evaluate the bundled-nlj block primitives has been demonstrated, and the usefulness of this approach in the development of future modules is clear. The necessary Gaunt factors for the new code have been developed and an investigation into the automation of detection of the bundling cut-offs performed using standard ion collisional rate expressions.

The thesis work presented here is a stepping stone into the full development of the new heavy species code. The lower levels will be dealt with in the existing ADAS 208 approach, requiring a phase of intensive fundamental atomic data production for the heavy species to be investigated. A code has to be developed to evaluate the new j-j coupled and cross-coupled Gaunt factors. Also, the bundling cut-off scheme has to be fully automated. This work is planned for the next phase of the ADAS collisional-radiative development. For a more indepth discussion on the future work necessary to carry the work here through to completion see chater 6.

Chapter 5

Special feature synthesis for continuum edge spectral analysis

5.1 Series limit spectral modelling background

A complete spectrum for series limit wavelengths through to the continuum can now be generated as a function of basic plasma parameters. This synthetic spectrum is referred to as a 'spectral feature'. To generate such a spectral feature it is necessary to bring together the population, line profile, opacity and continuity work presented thus far, the individual components of this feature being referred to as 'feature primitives'. This is analogous to the collisional-radiative block primitives and blocks of chapter 4. This chapter outlines the method of high series spectral feature generation and demonstrates the use of a code tailored for JET divertor conditions.

ADAS contains various diagnostic codes that perform a maximum likelihood fit of a spectral feature to observational data. ADAS 602 fits gaussian profiles to an observed spectrum and was used in the line identification work mentioned in section 2.9 and Brooks et al. (1999), and in the doppler shift diagnostic work of Spadaro et al. (2000) which led to the first observations of siphon flows in the solar atmosphere. ADAS 603 fits Zeeman spectral features to an observed spectrum thus diagnosing parameters such as the plasma magnetic field. See Summers (2001) for a description of both of these codes. Given the worth of such fitting codes as plasma diagnostics, the series

limit feature work forms a natural addition to the ADAS suite of codes.
Consider the following expression for the optically thick emergent flux from a plasma of length of line of sight b, with no incident background radiation field:

$$I(\lambda) = \int_0^b \varepsilon(\lambda, \underline{r})\Theta(\lambda)dl \tag{5.1}$$

The analytically continuous emission coefficient and escape probability expressions from chapter 3 are used. For applications such as those we are considering in this chapter it is also necessary to include other contributions to the emission coefficient such as those from other hydrogen continua, hydrogen bremsstrahlung emission and emission from plasma impurities. Section 5.2 deals in turn with all the contributions to equation (5.1). Section 5.3 describes a code that is being developed as a diagnostic tool for use in the divertor region of JET, with section 5.3.3 giving two example fits to observations with a corresponding diagnosis of plasma parameters.

5.2 General components of the series limit feature

5.2.1 Atomic populations

Since it is mainly high series hydrogen-like systems that are being considered at this stage, the high n-shell module of the population code described in chapter 4 is an appropriate means of evaluating the population distributions. The code evaluates b-factors for the populations up to arbitrary high n-shells for defined plasma parameters. A sample output datafile is shown in figure 5.1. The B(ACTUAL) column contains the b-factors for the populations. This is split up into various contributing parts, namely that from the ground state (metastable contributions can also be included in an extension of the code) in the F1 column, and the contribution from free-electron recombination in the F2 column. These contributions are then recombined independently to give the b-factor value B(CHECK), as a check to ensure that the separation procedure worked correctly without cancellation error.
The procedure is used in the spectral feature creation is as follows: the code is run for the required plasma parameters and a datafile as in figure 5.1 produced. The b-factor

values are then read from this file by the spectral feature code. Saha-Boltzmann populations are then modified by these b-values to give the resultant populations. Thus each different density and temperature parameter set requires a separate run of the population code. Although this increases the run-time for the feature generation, it is not a major issue for a final fitting code. A future ADAS fitting code will use a pre-calculated set of synthetic spectra or possibly spectral/population components (called 'feature files') which cover a wide range of plasma parameters. That is, to optimise the speed of the fit, the feature generation code will be separate from the fitting itself.

5.2.2 Opacity

Provided the plasma does not fall outside the moderate optical depth regime for which the escape factor technique is valid, one can use the continuous escape factor code of chapter 3 to allow optically thick series limit spectra to be modelled. This produces an escape probability as a function of wavelength that can be used in equation (5.1) as a modification to the escaping flux.

The opacity adjustments to the high lying populations can be done in a number of ways. In the absorption factor approach, the Λ values are used as parametric adjustments on the Einstein A-values in the collisional-radiative matrix. This is straightforward for low lying discrete lines where there is one unique Λ for each transition. For the higher series lines, there is some ambiguity as to whether an emitted photon originated from one upper level or from its neighbour. One approach is to split the high level populations into population elements, with corresponding frequency elements in the evaluation of Λ. The justification for this is that, as the levels merge together, it is no longer meaningful to talk about a discrete population and arbitrary elements of population can be defined. One can then evaluate rate expressions for all these 'elements' and insert them into the new collisional-radiative matrix to produce a population structure using Λs evaluated for each of these frequency elements. For future application to non-Maxwellian distributions this is the appropriate method to adopt.

```
EFFECTIVE CONTRIBUTION TABLE FOR ION PRINCIPAL QUANTUM SHELL POPULATIONS IN THERMAL PLASMA

0   HYDROG                   Z0 = 1.00E+00               Z1 = 1.00E+00

    TRAD = 1.00E+08 K        TE = 1.00E+04 K             TP = 1.00E+04 K
       W = 0.00E+00          NE = 1.00E+14 CM-3          NP = 1.00E+14 CM-3

      EH = 4.00E+04 EV/AMU   NH = 1.00E+07 CM-3       NH/NE = 1.00E-07   FLUX = 2.77E+15 CM-2 SEC-1

0COLLISIONAL DIELECTRONIC RATES

        IG         I             ALF     EFFECTIVE IONISATION AND CROSS COUPLING RATES
                                                 1              0              0
         1         1       2.2892252E-12  1.4270595E-14

0LEVELS OF MULTIPLICITY  2
0  IR     N     L   LT            F1             F2          B(CHECK)       B(ACTUAL)       NN/(BN*N+)
    1     1     0    0        2.6916359E+03  0.0000000E+00  2.6916359E+03  2.6916359E+03  5.9597787E-02
    2     2     0    0        2.1924905E+00  2.6379997E-02  2.2188705E+00  2.2188705E+00  1.7158663E-06
    3     3     0    0        4.3777740E-01  5.5533383E-01  9.9311124E-01  9.9311124E-01  4.3081850E-07
    4     4     0    0        8.3100860E-02  9.0542056E-01  9.8852142E-01  9.8852142E-01  3.5550177E-07
    5     5     0    0        2.0605225E-02  9.7560245E-01  9.9620768E-01  9.9620768E-01  3.8938354E-07
    6     6     0    0        6.5030788E-03  9.9215098E-01  9.9865405E-01  9.9865405E-01  4.6230796E-07
    7     7     0    0        2.4537084E-03  9.9700543E-01  9.9945914E-01  9.9945914E-01  5.6013275E-07
    8     8     0    0        1.0424843E-03  9.9871819E-01  9.9976068E-01  9.9976068E-01  6.7838517E-07
    9     9     0    0        4.7017507E-04  9.9941826E-01  9.9988843E-01  9.9988843E-01  8.1525759E-07
   10    10     0    0        2.0878734E-04  9.9973969E-01  9.9994848E-01  9.9994848E-01  9.6989633E-07
   11    12     0    0        3.0043268E-05  9.9996096E-01  9.9999100E-01  9.9999100E-01  1.3308700E-06
   12    15     0    0        4.0354204E-06  9.9999442E-01  9.9999846E-01  9.9999846E-01  1.9990008E-06
   13    20     0    0        3.1874614E-07  9.9999951E-01  9.9999983E-01  9.9999983E-01  3.4463330E-06
   14    30     0    0        2.6482030E-08  9.9999996E-01  9.9999998E-01  9.9999998E-01  7.5860560E-06
   15    40     0    0        5.4066752E-09  9.9999999E-01  1.0000000E+00  1.0000000E+00  1.3383208E-05
   16    50     0    0        1.6586765E-09  1.0000000E+00  1.0000000E+00  1.0000000E+00  2.0837106E-05
   17    60     0    0        6.6968164E-10  1.0000000E+00  1.0000000E+00  1.0000000E+00  2.9947585E-05
   18    70     0    0        3.4176328E-10  1.0000000E+00  1.0000000E+00  1.0000000E+00  4.0714588E-05
   19    80     0    0        2.1517221E-10  1.0000000E+00  1.0000000E+00  1.0000000E+00  5.3138091E-05
   20    90     0    0        1.6116508E-10  1.0000000E+00  1.0000000E+00  1.0000000E+00  6.7218084E-05
   21   100     0    0        1.3712864E-10  1.0000000E+00  1.0000000E+00  1.0000000E+00  8.2954561E-05
   22   110     0    0        1.2764456E-10  1.0000000E+00  1.0000000E+00  1.0000000E+00  1.0034752E-04

                                          BN = F1*(N1/N+) + F2
                                          N1 = POPULATION OF GROUND STATE OF ION
                                          N+ = POPULATION OF GROUND STATE OF NEXT IONISATION STAGE
                                          NN = POPULATION OF PRINCIPAL QUANTUM SHELL N OF ION
                                          BN = SAHA-BOLTZMANN FACTOR FOR PRINCIPAL QUANTUM SHELL N
                                          EH = NEUTRAL HYDROGEN BEAM ENERGY
                                           W = RADIATION DILUTION FACTOR
                                          Z0 = NUCLEAR CHARGE
                                          Z1 = ION CHARGE+1

NIP    =  0    INTD  =  3     IPRS   =  0   ILOW  =  0    IONIP =  0
NIONIP =  0    ILPRS =  0     IVDISP =  1   ZEFF  =  1.0  TS    =  1.00D+08
W      =  0.00D+00            CION   =  0.0       CPY   =  0.0
W1     =  0.00D+00            ZIMP   =  0.0 (  0.00D+00)
```

Figure 5.1: Population datafile produced by the hydrogen collisional-radiative code. Results are shown for $N_e = 1 \times 10^{14} cm^{-3}$, $T_e = 1 \times 10^4 K$. The b-factors are given in column B(ACTUAL), with the contributions from the ground state in column F1 and from recombination in F2. The plasma parameters are given at the top of the datafile.

An alternative approach is to consider discrete level populations, with corresponding rates for each level. One then considers the absorption from the resultant total intensity due to any overlapping profile at the right frequency to be absorbed by that line. That is, our absorption factor expression becomes:

$$\Lambda = 1 - \frac{\int_{\Delta\nu} \alpha_{discrete}(\nu) I_{blended}(\nu) d\nu}{\int_{\Omega} \int_{\Delta\nu} \varepsilon_{discrete}(\nu) d\nu d\Omega} \tag{5.2}$$

where the frequency integration is over the one high series spectral line profile, and the emission and absorption coefficients correspond to the values for that discrete line, i.e. no line blending is accounted for. It is only in the intensity term that the fully blended emission and absorption coefficients are considered.

This approach has the advantage that it requires minimal changes to the existing C-R code framework. Rates already exist for these high n-shells, and the Λ values evaluated here can be included directly. Figure 5.2 shows some results for this technique, generated using the high quantum shell Λ code from chapter 3 - note that, as expected, the absorption factors increase as one progresses up the series. It should be noted that for the $14 - 2$ transition and above, the lines are blending together significantly, and at higher optical depths one sees a slight decrease in absorption factor for these transitions. This is due to the fact that the radiation field causing the photo-absorptions is due to all the overlapping profiles and thus is greater than that produced if the emitting line was isolated. This naturally leads to more photo-absorptions in the line under investigation and hence a reduced absorption factor. This effect has been also been noted in the thesis of Fischbacher (2001). As the density increases the absorption factors decrease, as one would expect (recall the definition of the absorption factor in equation (1.14)).

It is easier to deal with the continuum opacity modifications to the population structure. The rates that are used in the collisional-radiative codes are all Maxwell averaged ones, thus it is most appropriate to evaluate an absorption factor that is also averaged over the whole continuum and can be used as parametric adjustments on the spontaneous recombination rates. A procedure has been written to evaluate this (see section 3.4.1), and the results are shown in figure 5.3 for an electron density of $1 \times 10^{14} cm^{-3}$ and an electron temperature of $1eV$.

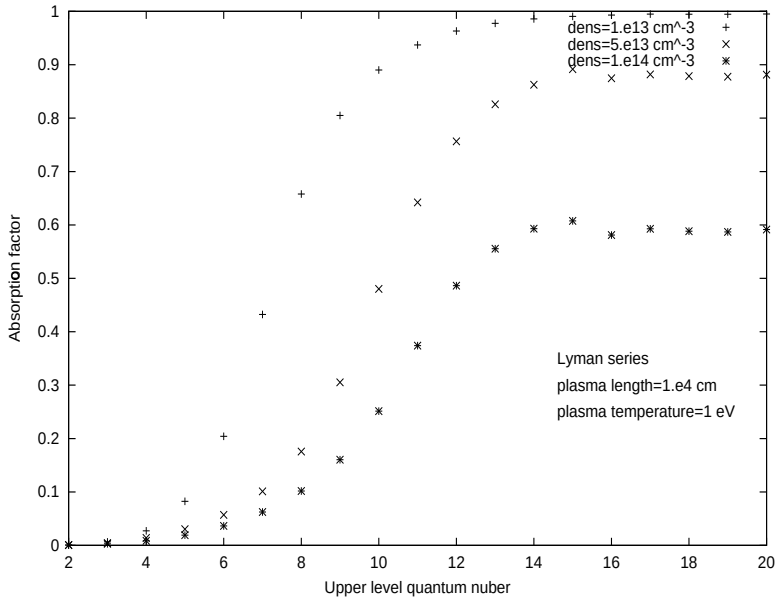

Figure 5.2: Continuum absorption factors as a function of upper level quantum number for the Lyman series for a plasma with $T_e = 1 \times 10^4 K$, $length = 1 \times 10^4 cm$ and a range of plasma densities.

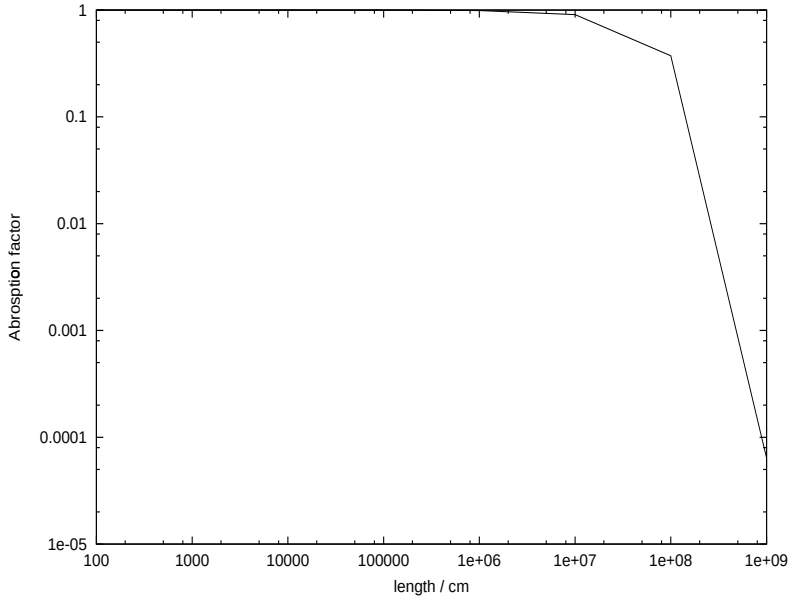

Figure 5.3: Continuum averaged Λ for the Lyman continuum plotted as a function of plasma length with $N_e = 1 \times 10^{14} cm^{-3}$, $T_e = 1eV$. Results are generated using the code of chapter 3

5.2.3 Line profile evaluation

Spectral line profiles are evaluated as described in chapter 3. The expression of Griem (1960) is used as the basic profile for all levels, but is substituted as appropriate for key observed lines by improved approximations. Here such high quality profiles are calculated by the PPP code (Talin et al., 1995, Talin et al., 1997). PPP is used for approximately the first fifteen series members. Calculation of the higher series members is somewhat computationally demanding, but is also of less importance, allowing the Griem profiles to be used. These line profile calculations are combined with the population results to evaluate the bound-bound contribution to the emission coefficient.

It is interesting to compare the line profile expressions as evaluated by the Griem equation with those evaluated using the PPP code. The profiles are primarily dependent on the electron density, but also vary with the electron temperature. Figure 5.4 shows the Griem profiles overplotted on the PPP results for a range of densities. It was found that the Griem profiles produce profiles extremely close to the PPP results up to densities of $\sim 2 \times 10^{14} cm^{-3}$ for typical divertor temperatures ($\approx 1eV$). For densities above this, the Griem profiles underestimate the electron broadening and thus produce profiles which are too narrow. Our primary interest for this work is in the divertor region of tokamaks with densities from $(0.1 - 5) \times 10^{14} cm^{-3}$, thus we are in the regime where the Griem expression is starting to break down. Nevertheless, it will still produce good profiles for many of the densities that one would want to investigate, and for densities beyond its region of validity the PPP profiles are used.

5.2.4 Bound-free, bremsstrahlung and impurity contributions

The higher bound-free hydrogen continuum contributions are evaluated from expressions such as equation (3.6). In the spectral feature code, a routine first developed for analysis of the bremsstrahlung emission in the JET tokamak (Horton, 2001) formed the basis for evaluation of all the hydrogenic bound-free contributions. The Horton procedures agreed exactly with an independent routine developed here. For compatibility with ADAS and other applications, it was decided to base the work here on

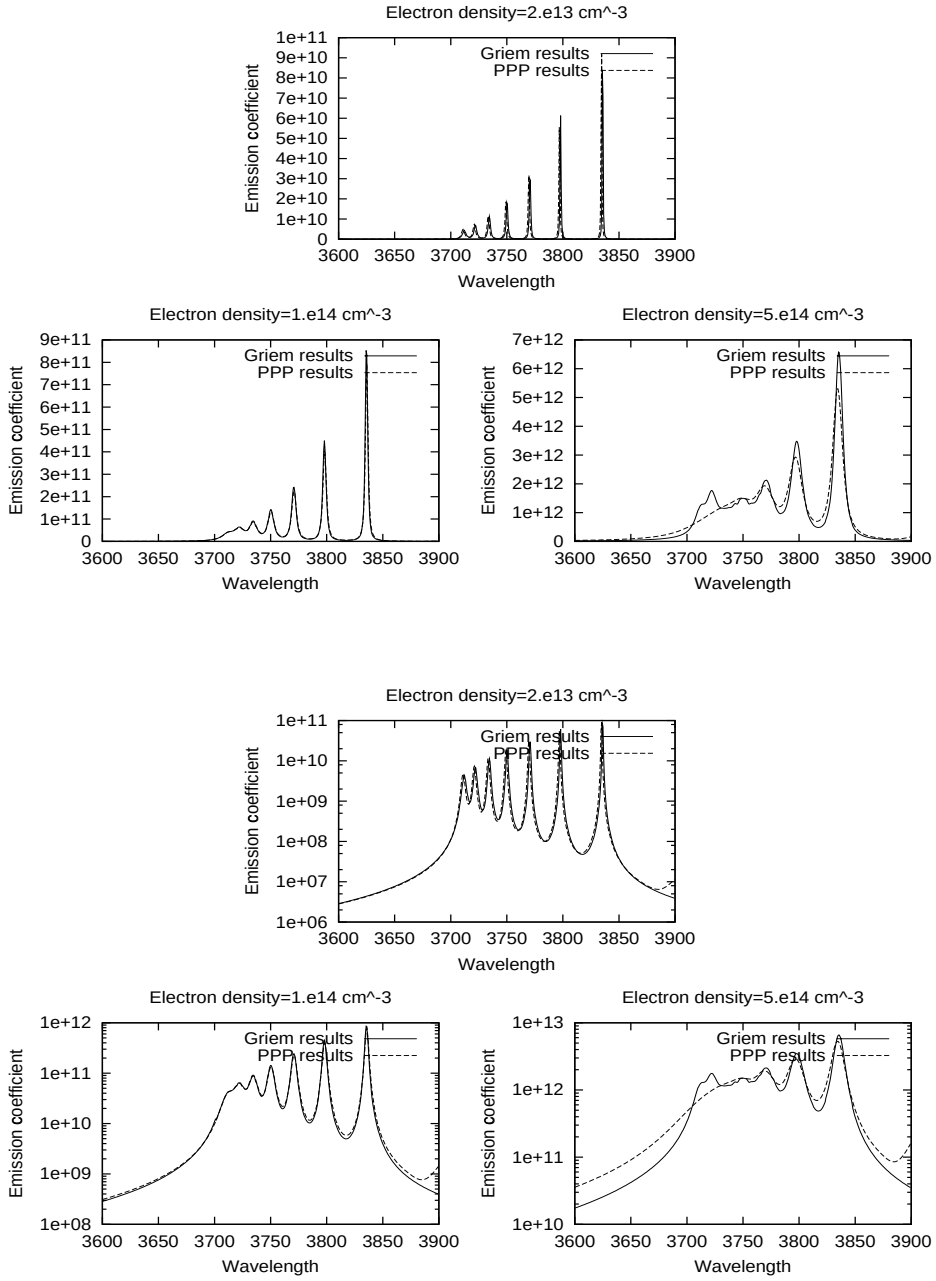

Figure 5.4: The resultant bound-bound emission coefficient evaluated using the collisionally broadened profiles of Griem (1960) compared with those from the PPP line broadening code. The lower set of plots show the results on a logarithmic y-axis. The first fifteen profiles of the Balmer series are evaluated. Note that the discrepancy at large densities is largely due to the Lorentzian profiles not being good extensions from Griem's profiles for these plasma parameters.

the Horton procedures. The hydrogen bremsstrahlung contribution from the Horton code is evaluated from analytic hydrogenic expressions given by Burgess & Summers (1987). Horton's code also evaluate all the continua from impurity species. For this it requires information on the ionisation and recombination coefficients for each ionisation stage of the impurity in question. This information is obtained using the ADAS subroutine d2data.for which in turn accesses atomic data from ADAS adf11 files. Note that all ionisation stages of an impurity are included
All the continua contributions from all possible impurity species are generated within the spectral feature calculation by this method. The impurity emitters may originate from a different region of the line of sight than the hydrogen emitters. Thus the code allows for different temperatures, densities and length of emitting regions in the impurity calculation.

5.3 A specific code for modelling the Balmer emission in the JET divertor.

5.3.1 Details of the physical problem

With the possibility of generating a complete spectral feature incorporating the continuum edge, a much more complete comparison with spectral observations is now possible. The main study here is as a potential diagnosis tool for the JET divertor. A description of divertor conditions and typical high series spectra has been given in chapter 1. In this region, one sees a strong Balmer series limit spectrum when the plasma detaches from the divertor wall. Under these circumstances it is no longer possible to rely on langmuir probe temperature and density measurements (such probes are embedded in the divertor walls) and alternative pure spectroscopic techniques such as this high series one become of value. The plasma parameters in this case are extracted by fitting a synthetic spectrum to the complete series limit and continuum edge observations. This has in fact been done with some success by Pigarov et al. (1998). See section 3.3 for a description of the differences between the approach presented here and the one used by Pigarov. The plasma parameters which

can be deduced in principle are the electron temperature from the free-bound continuum slope and intensity ratio of the high series members, the electron density from the width of the high series lines, the recombination state from the series decrement and, if the impurity contribution to the emission is significant, the Z-effective and impurity concentrations from the underlying continuum level.

The JET KT3 spectrometer was used to measure the high series Balmer spectra. KT3's line of sight 'sees' about 70% of the outer divertor target as shown in figure 5.5. It is estimated from the JET plasma transport codes that the Balmer emission originates from approximately 2-3 cm of the divertor region for the vertical plate discharge and 3-4 cm for the horizontal plate discharge, though these values have large uncertainties. As one can see from figure 5.5 the line of sight of KT3 passes through the centre of the tokamak cross section so the total observed intensity will potentially contain contributions from outwith the divertor region. In the experiment the KT3 instrument takes a sequence of temporal shots over a single JET pulse. Information is generated from each track (i.e. spatial position) at each time slice. KT3 has a spatial resolution of 13mm and 0.1nm spectral resolution. An exposure time of 100 msec was used for the high-n Balmer observations. Note that the spectrometer is able to measure the Paschen continuum edge and the spectral feature code is also able to model this spectral region. An analysis of Paschen spectra has yet to be performed. From Meigs et al. (1998) typical JET divertor conditions would be an electron density of $\sim 1 \times 10^{14} cm^{-3}$, neutral deuterium density of $\sim 1 \times 10^{13} cm^{-3}$ and electron and ion temperatures of $\sim 1 \times 10^{4} K$.

5.3.2 Modelling work

Population results

Figure 5.6 shows the b-value results of the population code for an electron density of $1 \times 10^{14} cm^{-3}$, and electron temperature of $1 \times 10^{4} K$. It can be seen that the atomic populations reach Saha-Boltzmann values by about $n = 5$. The b-values in figure 5.6 correspond to the datafile shown in figure 5.1. Examination of the datafile shows that the excited level populations are largely populated through recombination (i.e.

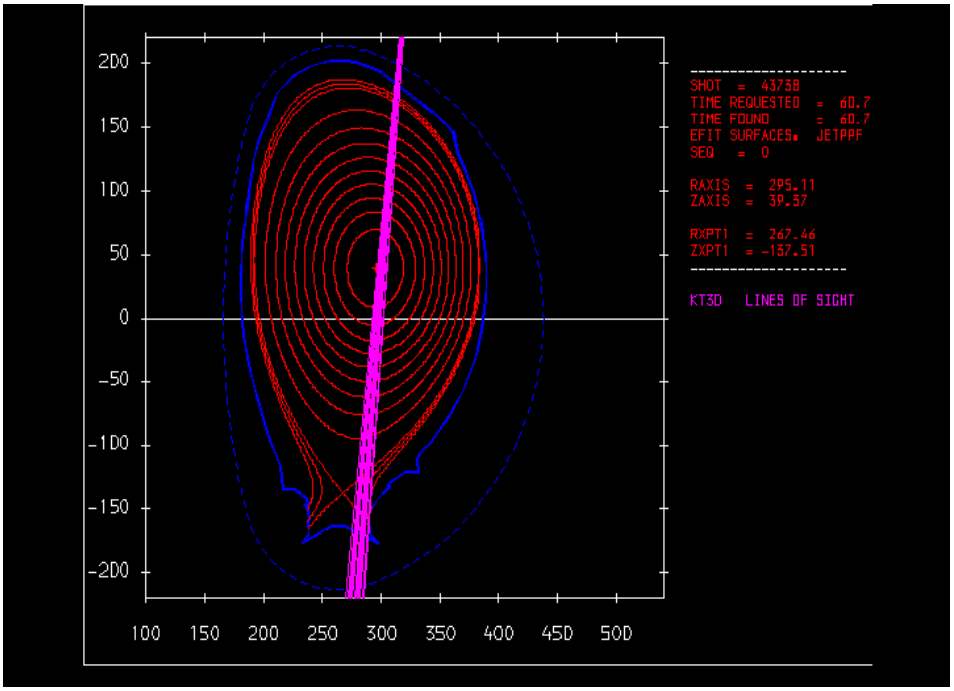

Figure 5.5: Illustration of the lines of sight of the KT3 instrument in the Balmer series limit observations.

the contributions to b_n come largely from the F2 column), as one would expect from a strongly recombining plasma.

Thus, for the higher Balmer series transitions which are of interest here, the upper level populations are close to their thermodynamic equilibrium values. Also, one can have confidence that the free electrons will have a Maxwellian velocity distribution, making the hydrogenic continua expressions for Θ and ε (which assume Maxwellian distributions) valid. Despite the fact that TE values would be sufficient, the spectral feature code takes the evaluated b-values into account to allow for extension to NLTE conditions if necessary.

Opacity results

The opacity code of chapter 3 was run for the selected divertor conditions and as expected the plasma is optically thin both from an emergent flux and a population point of view for the spectral region (see figure 5.7). Thus Θ can be set to one for the

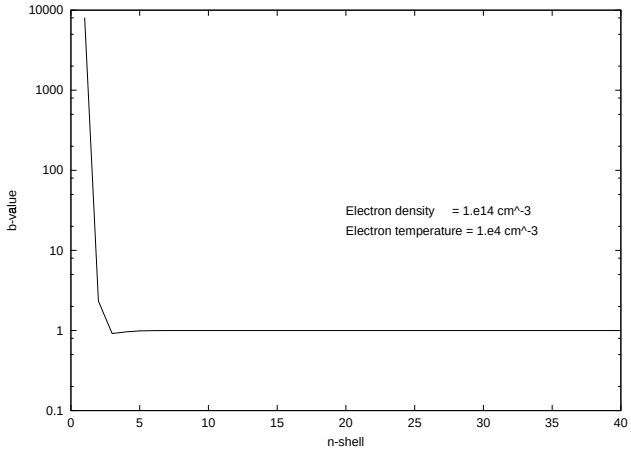

Figure 5.6: Population b-factors vs principal quantum shell for divertor conditions.

emergent flux calculation and no population adjustments are necessary for the higher series transitions.

As has already been shown in figure 1.11, the lower Lyman lines are likely to be optically thick. An optically thick population calculation was performed to evaluate the effect of Lyman series photo-absorption on the excited state population structure. ADAS 214 was used to generate the optically thick adf04 for population processing via ADAS 205, see figure 5.8. It can be seen that the n=2, 3 & 4 shells all have enhanced populations. Upon closer investigation it was found (for an electron density of $1 \times 10^{14}\, cm^{-3}$) that the increase in the n=2 population is due to photo-absorption, while the increase in the n=3 & 4 populations is mainly due to electron excitation from the enhanced n=2 shell, with the effect becoming less pronounced as one increases in n-shell. Thus there is an indirect influence of opacity on the populations for n $>$ 3. As was seen from figure 5.1, recombination dominates over collisional excitation for the highly excited states, and these opacity effects are not likely to change this. However, the photo-absorption enhanced population of the n=2 shell and subsequent collisionally enhanced populations of the higher shells must be included for completeness in the final ADAS code to allow lower series members to be modelled correctly. Thus for the series limit work presented in this chapter opacity is considered to have a negligible effect on the highly excited populations.

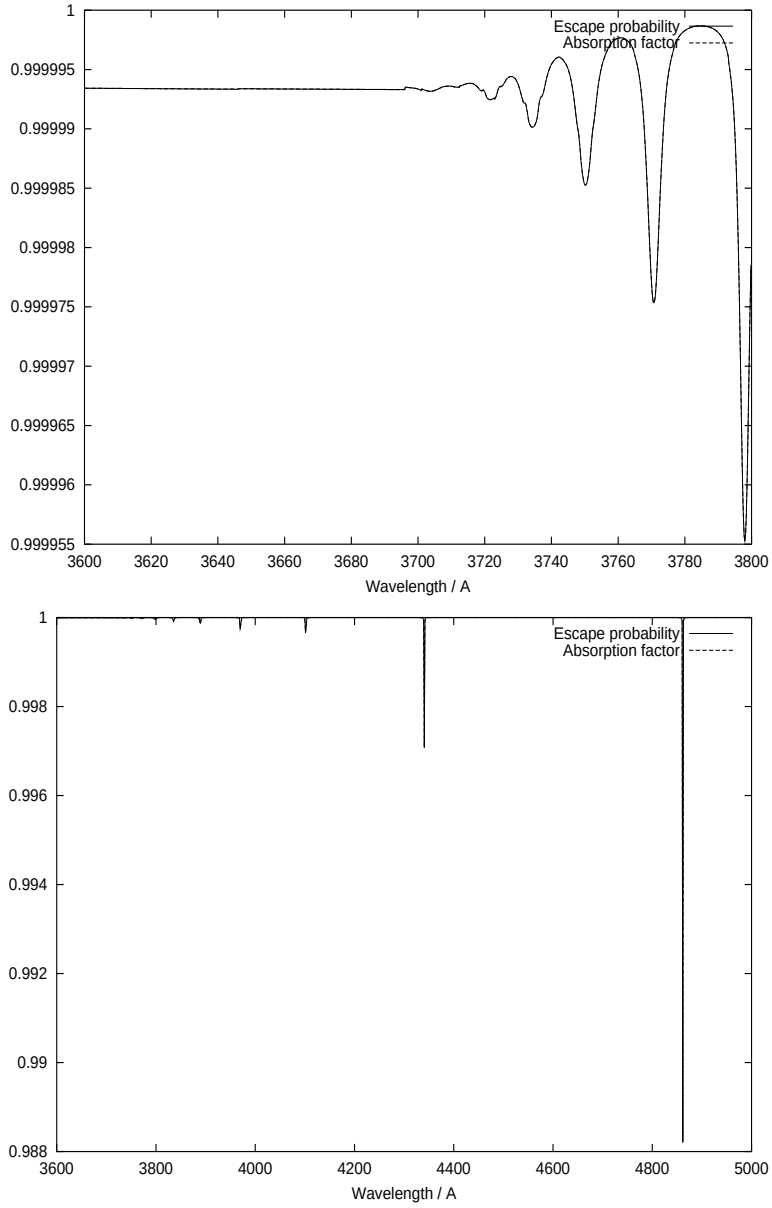

Figure 5.7: Analytically continuous escape probabilities and absorption factors vs. wavelength evaluated for typical divertor conditions. The upper plot shows the results near the series limit and the lower plot the results including lower series members. Note that on both scales, the factors are negligible.

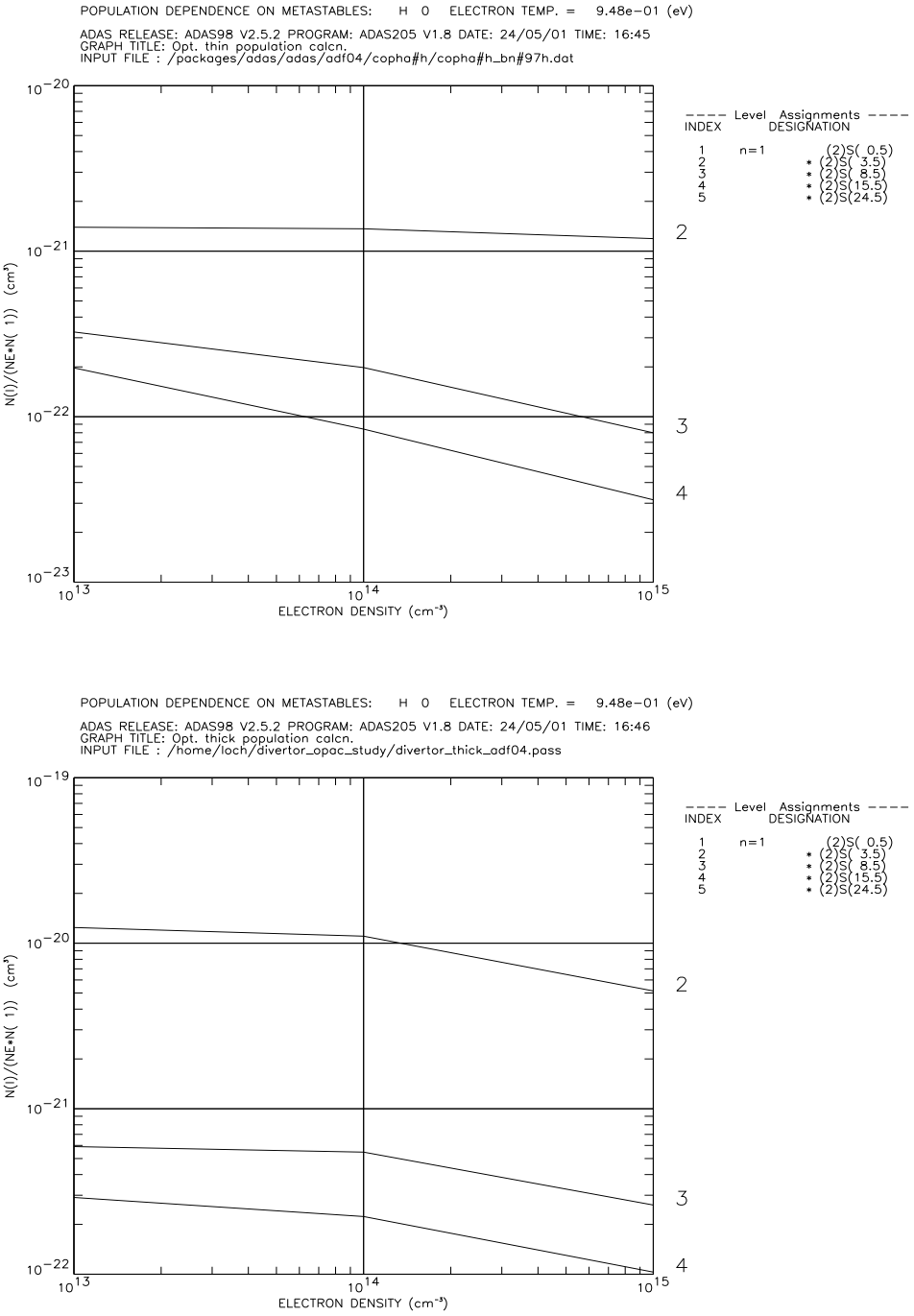

Figure 5.8: Upper plot shows the optically thin excited population densities for the first five n-shells for typical divertor conditions. The lower plot shows the optically thick results.

Hydrogen bound-bound, bound-free, bremsstrahlung results and impurity contributions

The emission coefficient as evaluated in the code is made up of many components. Figure 5.9 shows the hydrogen bound-bound, bound-free and bremsstrahlung contributions for the case of an electron density of $1 \times 10^{14} cm^{-3}$, electron temperature of $1eV$ and a line-of-sight length of $10cm$. Note that the other hydrogen continua, in particular the Paschen continuum makes a significant contribution to the resultant spectrum at the minima between discrete series lines. The bremsstrahlung contribution is the least significant, but must still be accounted for.

In order to evaluate the impurity contributions to the emission it is necessary to know the impurity concentrations in the divertor plasma. Typical values for JET are given in McCracken et al. (1998). Figure 5.10 shows the contributions to the total intensity of the synthetic spectrum from carbon, oxygen and beryllium impurities at the median concentrations of McCracken (i.e. impurity concentrations of 1 %, 1 % and 0.2 % of the deuterium density respectively). The impurity contribution, although present, does not significantly alter the synthetic spectrum. For the results shown in figure 5.9 and 5.10 the hydrogen b-b, b-f and impurity emitters were given identical line of sight lengths, electron densities and temperatures.

Note that the inclusion of the various continuum contributions (even at the 10 % level) significantly alters the diagnostic values returned by a fit to the observed spectrum. If these contributions are excluded then a higher electron density is inferred - the fit procedure increases the model density to broaden the lines so that the minima between discrete lines can be matched.

5.3.3 Fitting the JET data and diagnostic results.

Fits were performed on data from two different density runs where the tokamak was configured such that the strike point was on the vertical and then on the horizontal plates of the divertor (JET pulse numbers 43735 and 43738). Observational data from KT3 was available for these two pulses for a range of time slices and track numbers. For consistency it was decided to examine the results from track number 6 for both

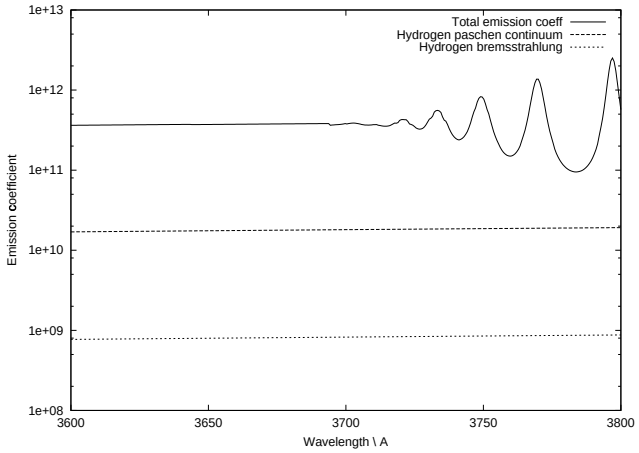

Figure 5.9: Contributions to the emission coefficient from the different hydrogen components. The code was run for $N_e = 1 \times 10^{14} cm^{-3}$, $T_e = 1eV$, emitting length=$5.5cm$. The bremsstrahlung emission is assumed to come from the same emitting region as the bound-bound and bound-free components.

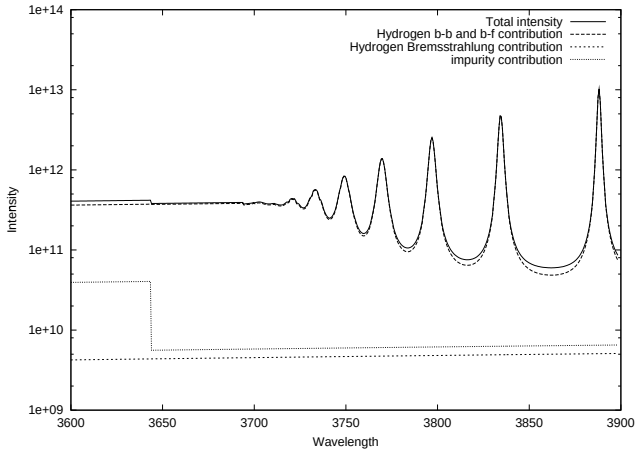

Figure 5.10: Contributions to the total intensity from all the hydrogen and impurity emitters. The input parameters were as in figure 5.9. The step in the impurity contribution is because the impurity code assumes hydrogenic continuum edges for each ionisation stage.

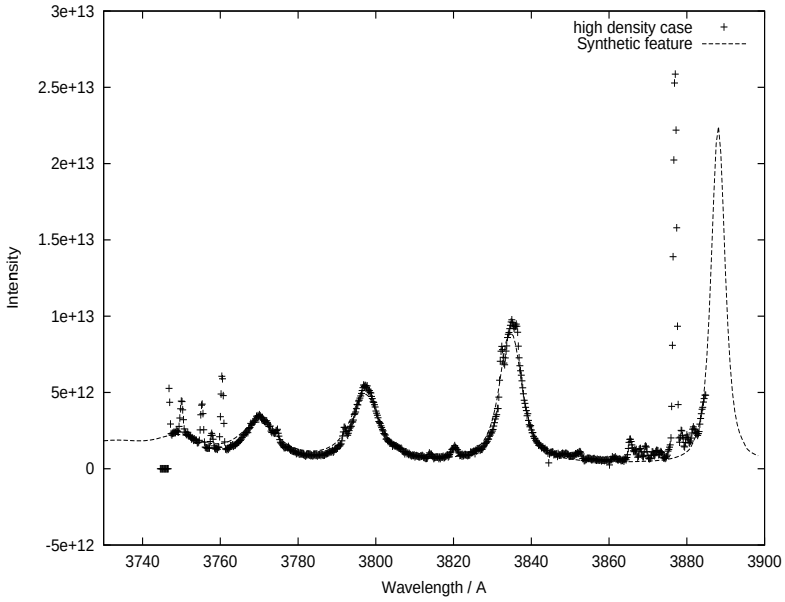

Figure 5.11: Diagnostic fit to pulse 43735, Balmer series limit spectrum, track 6, t=18.95s

pulses. An analysis of these pulses has already been performed (Meigs et al., 1998 and Meigs et al., 2000) where the FWHM of the 9-2, 10-2 and 11-2 lines were measured and the electron density inferred. An electron density is deduced by Meigs for each of thee three lines independently using a Stark profile expression from Breger, 1998. For a meaningful comparison to be given, it was decided to model each pulse at a time slice for which FWHM data and hence diagnosed electron density had been obtained. Figure 5.11 shows our optimised fit to the data of pulse 43735. Note that the fit was optimised iteratively by hand. The automatic least squares optimising of the feature to the data is in development as a future ADAS code. The diagnostic values from the fit are shown in table 5.1 with the results from the FWHM analysis of Meigs shown in table 5.2.

The second fit performed was to the results of pulse 43738. Figure 5.12 shows our fit to this lower density data. The deduced parameters are shown in table 5.3 and the FWHM results in table 5.4.

Physical quantity	Value for synthetic feature
Electron density	$3 \times 10^{14} cm^{-3}$
Ion density	$3 \times 10^{14} cm^{-3}$
Electron Temperature	$1eV$
Length of line of sight	$3cm$
Impurities	Carbon, Oxygen, Beryllium
Impurity abundances	$1\%, 1\%, 0.2\%$

Table 5.1: The diagnostic values returned from the fit shown in figure 5.11

Balmer line	FWHM $\mathring{A}$	Diagnosed density cm^{-3}
9-2	4.6792922	$4.19 \times 10^{14} cm^{-3}$
10-2	5.8150216	$4.29 \times 10^{14} cm^{-3}$
11-2	7.5598365	$4.29 \times 10^{14} cm^{-3}$

Table 5.2: Diagnosed electron densities from the FWHM analysis of Meigs.

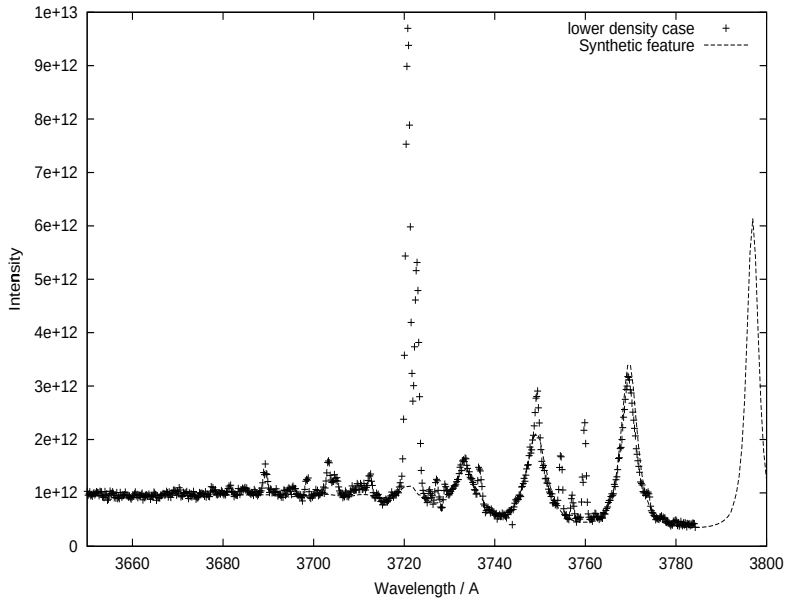

Figure 5.12: Diagnostic fit to pulse 43738, Balmer series limit spectrum, track 6, t=19.45

Physical quantity	Value for synthetic feature
Electron density	$0.85 \times 10^{14} cm^{-3}$
Ion density	$0.85 \times 10^{14} cm^{-3}$
Electron Temperature	$1eV$
Length of line of sight	$16cm$
Impurities	Carbon, Oxygen, Beryllium
Impurity abundances	$1\%, 1\%, 0.2\%$

Table 5.3: The diagnostic values returned from the fit shown in figure 5.12

Balmer line	FWHM $\mathring{A}$	Diagnosed density cm^{-3}
9-2	2.7419637	$1.88 \times 10^{14} cm^{-3}$
10-2	3.6132523	$2.10 \times 10^{14} cm^{-3}$
11-2	4.5239519	$2.10 \times 10^{14} cm^{-3}$

Table 5.4: Diagnosed electron densities from the FWHM analysis of Meigs.

Discussion of the fit

As one can see from the graphs and the optimised input parameters, reasonable fits have been achieved. The present fits to the spectra yield systematically lower densities that those returned from the FWHM analysis. This is because the continua contribution are not considered in the FWHM analysis. As was indicated in section 5.3.2, neglecting the complete set of continuum contributions can leads to an inferred electron density that is spuriously high. Failure to account for all continuum contributions may also explain a similar discrepancy noted as point (iii) of the series limit analysis of stellar flares in Zarro & Zirin (1985).

It should be noted that obtaining an optimal fit as shown above is not just a matter of matching the line widths on the high series lines. The code returns the absolute intensity of the spectrum and it is necessary for this to match the observations as well. Thus the line widths, degree of line blending and absolute intensity all have to be correct for a good fit to be achieved. This internal consistency adds value to the diagnostic parameters returned from the fit.

Some development of the code is required before it can be used as a diagnostic tool. The first thing to note is that there are many variables that affect the fit. An unconstrained multi-variable optimised fit would certainly reveal many local minima and an ambiguous set of 'optimised' parameters. A number of the variables, such as impurity concentrations are only weakly orthogonal from the point of view of continuum emission. The number of search parameters must be reduced, or some 'global optimisation' of a whole range of diagnostic measurements including this present series limit one must be adopted. For the demonstration here, we have felt able to specify a number of parameters to a reasonable degree of accuracy independently (especially impurity abundance and length of emitting region) to allow the remaining parameters to be varied and a meaningful fit achieved. We note that the the line-of-sight length used in the fit of pulse 43735 is longer than one might expect. For typical divertor models, the length of emitting region is $\sim 3 - 5cm$. It is probable that contributions to the measured intensity also came from the part of KT3's line-of-sight passing through the core of the plasma. A possibly improvement to our mehtod is to use the KS4 instrument as a second reference spectrometer. It is similar to the KT3 instrument, except that its line-of sight excludes the divertor region. This could be used to determine the contribution to the intensity from regions outside the divertor and hence be used to adjust the KT3 observations. Even with this it is probably necessary to model the predicted intensity as originating from two different emitting regions within the divertor as is done in Pigarov et al. (1998). More information from JET plasma modelling codes is needed to guide such an approach.

5.4 Conclusions

The generation of complete series limit spectral features has been demonstrated and the fitting of such features to JET divertor observations shown. Good fits were achieved for both a 'low' ($N_e \sim 0.85 \times 10^{14} cm^{-3}$) and a 'high' density ($N_e \sim 3 \times 10^{14} cm^{-3}$) observation. The next stage will be to tailor the code to be more specific to the JET divertor setup, for example taking into account all of the emission from the line of sight, not just those from the divertor, and diagnosing the impurity content

for the JET pulses that were analysed.

This work is planned for the immediate future, the aim being to have a code that can perform an optimised fit to the JET high series Balmer observations from the divertor region and return diagnostic information on the local plasma electron temperature and electron density. This will be incorporated into the existing JET data analysis software. The proposed code will perform a least squares fit, and will cycle through multiple spectra once the initial fitting parameters have been set. In developing this code, advantage will be taken of the structure of the existing ADAS fitting routines.

Chapter 6

General conclusions and future work

6.1 General conclusions and summary

This thesis has presented a general investigation into spectral series emission and population modelling valid for both astrophysical and laboratory fusion plasmas. Starting with an overview of basic escape factor techniques, their usefulness in modelling opacity effects on population structure and emergent flux was shown within the context of four sets of observations. A branching line ratio study of the solar atmosphere demonstrated the use of escape probabilities as an optical depth diagnostic. Observations of the L_β/H_α ratio from the divertor region of the ASDEX upgrade showed the use of absorption factors in calculating optically thick population densities. Series limit observations of solar prominences and the JET divertor highlighted the possibility of developing a spectral feature code as an electron density, temperature and plasma recombination state diagnostic.

A thorough treatment of low series member opacity was then developed in association with the conversion of the code of Behringer into ADAS 214. The use of the new code in the CDS line identification work was presented and an extension of the model to include a background radiation field given. The modified adf04 files produced by this code are immediately applicable in existing ADAS collisional-radiative routines, and

can be used to investigate the effects of moderate opacity on excited state populations. The need to model series limit spectra led to the proofs of analytic continuity contained in chapter 3. This allows opacity adjustments to the flux and populations to be dealt with smoothly across the ionisation threshold. The treatment of the series limit taken in this thesis is contrasted with the usual technique of assuming that a statistical microfield 'dissolves' bound excited states into the continuum.

This led to the population work of chapter 4 where a high quantum shell collisional-radiative model and code were developed. The model forms part of a larger plan to model the populations of heavy species, with the code developed in this chapter providing a natural module which will be added to a low level code of similar type to ADAS 208. An outline of the heavy species model was given, with a description of the approach to be taken in the assembly of each collisional-radiative module. As part of this plan, new Gaunt factors were developed. A scheme to automatically detect the critical n-shells between bundling regimes was also shown. The high quantum shell code of this chapter evaluates the $(\gamma_p \pi_p J_p)n$ and $(\gamma_p \pi_p J_p)nl$ block primitives of the new scheme. A test module for the $(\gamma_p \pi_p J_p)nlj$ component was developed and can be extended to evaluate a complete nlj block primitive. The code of chapter 4 is immediately applicable to the hydrogen series limit spectral feature work of chapter 5.

The assembly of such spectral features was then described, bringing together the continuity, opacity and population work of the previous chapters as well as including expected contribution of impurity species to the background continuum. A description of a code designed as a diagnostic tool for the JET divertor is then given. It was shown that the code can fit both high and low density observations and return local plasma parameters.

6.2 Areas for future work

The studies in this thesis indicate some areas in which the usefulness of existing ADAS procedures handling opacity can be improved. The principal of these is to introduce some special capacity in ADAS 214 for a radiation field consistent with the population

structure, more details are given in section 6.2.1. There are two major conceptual issues from this thesis which are expected to influence substantially our research in the immediate future. These planned developments are outlined in sections 6.2.2 and 6.2.3.

6.2.1 Extensions to ADAS 214

At the moment ADAS 214 starts with a modified Boltzmann population distribution, evaluates the resultant radiation field and uses this to calculate absorption factors and hence a thick population structure. If these populations are used as the starting point of further iterations, a population structure which is consistent with the plasma radiation field may be achieved, the system being iterated until the population converged.

6.2.2 Future work for the series limit code

The future series limit work divides into two approaches. Firstly one can construct spectral feature fitting procedures which use plasma information from other diagnostics or plasma codes to constrain certain fitting parameters. An optimised fit of the observed series limit is then done as in the existing ADAS fitting codes. This technique can be immediately pursued and a further member of the ADAS series 6 will be provided.

The second approach is more long term. The fitting code can be made part of a global optimisation procedure. Thus, instead of performing a fit based upon external bounding data from other codes and diagnostics, the fitting code is one part of an integrated fit to the complete set of tokamak parameters. This has particular application to fusion, where the series limit code can be integrated with existing plasma transport codes. In this approach the whole set of codes forms the fitting procedure, and consistency amongst all fitted parameters must be achieved for a valid fit. This presents a significant task, both in the assembly of the set of codes and in the computational optimising of the fit.

Both approaches require development of series limit procedures which are robust, efficient and tailored to the specific experimental setup of the plasma under investigation. Initially there are two types of experimental spectra which will be modelled.

Hydrogen series limit code

With minor modifications the divertor series limit code of chapter 5 can be integrated into the JET divertor diagnostic software. Constraints must be put on the initial fitting parameters, based upon information from other plasma diagnostics. In particular, more detailed knowledge of the core impurity contribution to the spectrum can be measured using the KS4 spectrometer. The code of chapter 5 will be called as part of a least squared fitting procedure, in the same manner as the existing ADAS fitting codes. A useful capability of these codes are that they allow impurity lines as well as the generated spectral feature to be incorporated in the fit (the presence of impurity lines in the JET data can be seen from figure 1.15). It is hoped that such a fitting code will resolve the discrepancy found when the FWHM analysis is used to diagnose electron densities from various series limit lines where agreement was found using the 11-2 and 8-3 lines but not using the 7-3 line (Meigs et al., 2000). This work is planned for the immediate future.

Helium series limit code

The principles of continuity and feature generation can be extended to model helium series limits. Here of course both singlet and triplet series limits will be produced. There have been two recent observations of the helium Lyman series limit. The first was in a high density laboratory plasma and analysed using a collisional-radiative model (Namba et al., 2000) which included an escape probability to account for opacity. This allowed the observed plasmas to be classified into ionising and recombining type. The Lyman series limit was also observed in the DIII-D tokamak (Whyte et al., 2000) and the recombination spectrum used to diagnose the plasma electron temperature and effective ionic charge during plasma disruption.

While the Lyman series is of interest, the main opportunity for future research lies

in modelling the triplet series. For higher quantum shells L-S coupling breaks down, and the excited electrons can be thought of as a mixture of singlet and triplet states. Thus electron on the triplet side effectively spend some time in a singlet state and are no longer mainly confined to decaying down to the $1s2s\,^3S$ shell. Thus one would expect that the resulting triplet spectrum would consist of discrete lower series lines and that as one progresses up the series a partial quenching of the spectrum would be observed at the point where the spin system breakdown allows triplet electrons to decay down to the ground on the singlet side. Such a quenching has been observed (Ohno et al., 1998), though it was interpreted as evidence of molecular activated recombination.

Collisional redistribution is an essential ingredient for such quenching to take place. The collisional-radiative modelling of the highly excited states of helium is an area requiring attention, and a technique which allows the nature of the spin system breakdown to be investigated would be useful. Improvements in the collisional-radiative model would then reap further benefits in all helium based diagnostics. It should also be noted that the new scheme proposed for the heavy species work does not use the conventional L-S coupling for the excited states and so will be able to track the behaviour of these excited states, and the expected series quenching. The density sensitivity of the spin system breakdown could also be used as a diagnostic tool.

In a recent experiment at JET some preliminary observations were taken to evaluate whether any helium triplet series could be observed (Meigs, 2001). In the region 3640 Å $\rightarrow$ 3520 Å members of the triplet series (to $1s\,2p\,^3P$) were observed, and quenching effects detected. Thus it appears that further work into series limit modelling for helium triplet series is justified.

6.2.3 Population extension for heavy species

The extension of the population work of chapter 4 to deal consistently with heavy species populations provides a variety of future applications. The primary motivation for this work at the present time is the need to be able to detect heavy species at typical ITER temperatures and densities. It has been proposed that heavy species

be embedded at different depths in certain of the carbon fiber composite wall tiles of ITER as erosion markers. As the tiles are eroded the heavy species layer is ejected into the plasma core and its spectral signature detected. It will also be necessary for ITER to take advantage of the good thermal resistance of heavy species in the tokamak design. Consider the spectrum from a species such as tungsten. One observes a complex grass-like spectrum arising from a combination of the many ionisation stages of the species and the complex set of energy levels present. The grass-like spectrum does however have a recognisable 'spectral envelope' arising from imperfectly resolved 'transition arrays'. This envelope shows a strong temperature dependence. The marching of transition arrays as one progresses iso-nuclearly and iso-electronically has been shown theoretically (O'Mullane & Summers, 1999). This will allow even adjacent heavy species to be resolved. The higher levels become hydrogenic in behaviour and their series limit spectra merge with the general continuum-like appearance of the spectral envelopes.

Pixel sums over specified wavelength intervals will be performed on the observed envelopes using 'computational filters'. This will be used to extract a set of numbers ('signature numbers') to be used as the parameters to be matched in a high throughput fitting procedure. Both neural networks and genetic algorithms will be investigated as potential pattern recognition methods. It will be possible to generate training data to test the fitting procedures. At present experimental spectra for the heavy species at expected ITER conditions cannot be generated, and as the transition array are markedy temperature sensitive, lower temperature data will not be sufficient. Thus computational modelling will be relied upon to generate synthetic signature numbers and provide the necessary training datasets. To test the robustness of the fitting procedures the synthetic envelopes will be combined with actual noise from an experimental device such as JET. This will produce test datasets of 'noisy' signature numbers to be fitted by the code.

The work required for the completion of the heavy species collisional-radiative model is significant, but achievable. The new coupling scheme has been outlined in chapter 4. The $(J_p)nl$ and $(J_p)n$ resolved block primitives can be evaluated at present. The single n-shell test code for the $(J_p)nlj$ resolution will be extended to encorporate

an entire block primitive. This will then be used to test condensation schemes, the effects of the redistributive rates and methods of population solution. An $(J_p)nlj$ block primitive code will then be written.

The initial baseline data for the low level blocks will be generated using ADAS 801, and will be produced in adf04 format. The data will be complete for the species under investigation, but of fairly low quality. The low level data will then be supplemented with higher quality data from codes such as HULLAC and R-matrix. The low level rates will be assembled in the ADAS 208 approach. The influence of the higher populations can then be projected onto these low lying results and a population solution obtained.

The modularisation of the code outlined here allows advantage to be taken of modern high performance parallel computers. Each block primitive can be calculated independently on a different processing node. The block primitives can then be assembled into the blocks and the final superblock matrix. Such parallel techniques are likely to be required for the assembly and solution of the large matrices needed for heavy species modelling.

The collisional-radiative code will be combined with an ionisation balance calculation to predict a synthetic feature. The feature will then be isolated into components and fitted to the observed filtered envelope segments. The final model will be linked to a plasma transport code and used in a global optimisation routine wherein theoretical spectral features, elemental concentrations, densities and spatial distributions are simultaneously fitted to observed plasma parameters.

Appendix A

Gaunt factor evaluation

This appendix derives equations (4.7) and (4.9), for use in the calculation of the Gaunt factors for the new coupling scheme. Coupling of the angular momentum of a valence electron to the core configuration can be conveniently expressed with the introduction of 'Clebsch-Gordan' coefficients (sometimes referred to as 'vector coupling' coefficients and equivalently expressed as 'Wigner 3-j' coefficients). Consider the wavefunction $\Psi(j_1 j_2 j m)$ such that j is the resultant angular momentum due to j_1 and j_2, with corresponding magnetic quantum number m. The Clebsch-Gordan coefficient ($C^{j_1 j_2 j}_{m_1 m_2 m}$) can be used to uncouple $\Psi(j_1 j_2 j m)$ into the constituent wavefunctions for j_1 and j_2. $C^{j_1 j_2 j}_{m_1 m_2 m}$ and is defined such that

$$\Psi(j_1 j_2 j m) = \sum_{m_1 m_2} C^{j_1 j_2 j}_{m_1 m_2 m} \Phi(j_1 j_2 m_1 m_2) \tag{A.1}$$

where $\Phi(j_1 j_2 m_1 m_2) = \Psi(j_1 m_1)\Psi(j_2 m_2)$. Angular momentum problems reduce to a set of these Clebsch-Gordan coefficients which can be further reduced to a set of 'Wigner 6-j' and higher coefficients using various transformations and symmetry properties. There exists an elegant technique, first introduced by Levinson (1955) for the manipulation of angular momentum coefficients, whereby one converts the coefficients into graphical form and manipulates the resultant diagrams. The various mathematical transformations of the Clebsch-Gordan coefficients all have corresponding geometric transformations on the diagram. The graphical method is described in standard quantum angular momentum text books such as Rose (1986), Edmonds

(1974), with the most complete description being found in chapter 7 of Brink and Satchler (1968). For completeness, the key details are reproduced here in appendix A.1. The new Gaunt factors are then derived using these rules in appendix A.2.

A.1 Basic rules for graphical expression and manipulation of Clebsch-Gordan coefficients

The Clebsch-Gordan coefficients can be transformed into Wigner 3-j coefficients as shown in equation A.2.

$$C^{abc}_{\alpha\beta\gamma} = (-1)^{a-b-\gamma}(2c+1)^{1/2} \begin{pmatrix} a & b & c \\ \alpha & \beta & \gamma \end{pmatrix} \tag{A.2}$$

where $\begin{pmatrix} a & b & c \\ \alpha & \beta & \gamma \end{pmatrix}$ is the wigner 3-j coefficient. This is expressed graphically by associating a straight line with each of the angular momentum vectors a, b and c and joining the lines at a single point or 'node'. The Clebsch-Gordan symbol is drawn as in figure A.1 and the Wigner 6-j as in figure A.2. - note that each node has a sign attached to it. By convention the magnetic quantum number associated with each angular momentum vector is omitted from the diagram. Also note that some vectors have directional arrows attached to them.

The rules for graphical manipulation of Clebsch-Gordan coefficients are as follows:

1. Any geometric deformation that preserves the order of the arrows and signs on each node is allowed. If the cyclic order at any node is changed there must be a corresponding change in the sign of the node.

2. A change in the cyclic order of the 3-j symbol results in a change in the sign of the node as shown in figure A.3.

3. Two lines representing the same total angular momentum can be joined together as in figure A.4

4. A line with two oppositely directed arrows is equivalent to a line with no arrows

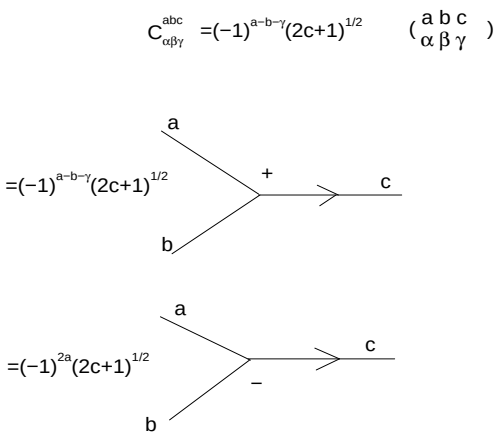

Figure A.1: Graphical representation of the Clebsch-Gordan coefficient

5. A line corresponding to an angular momentum a with two arrows in the same direction is equivalent to a line with no arrows times a factor $(-1)^{2a}$.

6. If an arrow on a line with angular momentum a is reversed, the graph must be multiplied by a factor $(-1)^{2a}$.

7. Three arrows may be added to a node, one to each line, without changing the value of the graph. The arrows must all be directed either into or out from the node.

The 'Wigner-Eckart' theorem can be used to reduce the matrix $< jm|T_{\lambda\mu}|j'm' >$, where $T_{\lambda\mu}$ is an irreducible tensor operator (such as a spherical harmonic), to extract the dependence on the magnetic quantum numbers. The theorem states that

$$< jm|T_{\lambda\mu}|j'm' >= \frac{< j||T_\mu||j' >}{\sqrt{2j+1}} C^{j'\lambda j}_{m'\mu m} \tag{A.3}$$

Note that the magnetic quantum number is now contained in a Clebsch-Gordan coefficient.

$$\begin{Bmatrix} a & b & e \\ d & c & f \end{Bmatrix} \equiv \sum (-1)^{a+e+c-\alpha-\varepsilon-\gamma} \begin{pmatrix} a & f & c \\ \alpha & \phi & -\gamma \end{pmatrix} \begin{pmatrix} c & d & e \\ \gamma & \delta & -\varepsilon \end{pmatrix} \begin{pmatrix} e & b & a \\ \varepsilon & \beta & -\alpha \end{pmatrix} \begin{pmatrix} b & d & f \\ \beta & \delta & \phi \end{pmatrix}$$

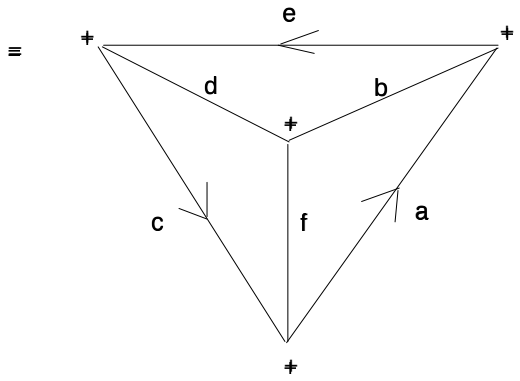

Figure A.2: Graphical representation of the Wigner 6-j coefficient. The summation is over all magnetic quantum numbers.

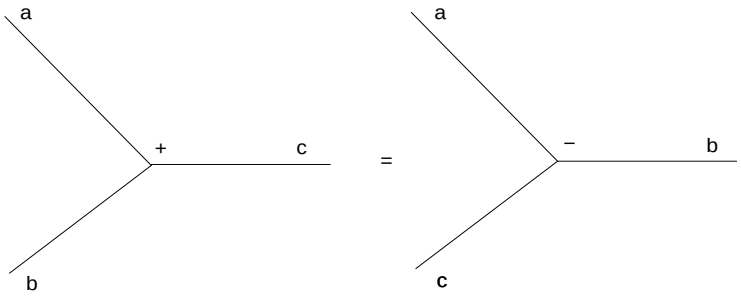

Figure A.3: Change in cyclic order of Wigner 3-j symbol

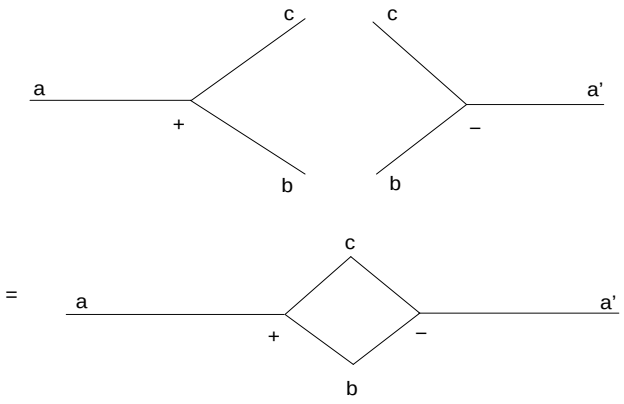

Figure A.4: Combining Wigner 3-j symbols

A.2 Application of the graphical manipulation method for Clebsch-Gordan coefficients

The evaluation of Gaunt factors, such as the bound-bound expression

$$g^I_{i,i'}(\nu,\nu') = \frac{\sqrt{3}}{\pi 2^4}\left(\frac{E-E'}{z_1^2 I_H}\right)^4 \frac{1}{\omega_\gamma} Q_{i,i'} R^I_{i,i'}(\nu,\nu') \tag{A.4}$$

reduces to a need to evaluate Q and R, where R is the radial integral component and Q contains the angular factors. In the case of a highly excited level built on a parent level, Q and R can be rewritten

$$Q_{i,i'} R^I_{i,i'}(\nu,\nu') = < (S_P L_P J_P M_P) nljmJM|\underline{r}|(S'_P L'_P J'_P M'_P) n'l'j'm'J'M' > \tag{A.5}$$

At this point the RHS is simplified using Clebsch-Gordan coefficients.

A.2.1 Gaunt factors for j-j coupled initial and final states

Consider a transition between two fully J-resolved levels, we evaluate the $Q_{i,i'} R^I_{i,i'}(\nu,\nu')$ component of the Gaunt factor and split the position vector $\underline{r}$ into its radial and spherical harmonic components. The expression that must be evaluated becomes

$$\begin{aligned} \langle (S_p L_p J_p) nljJM|\underline{r}|(S'_p L'_p J'_p) n'l'j'J'M'\rangle &= \\ \langle (S_p L_p J_p) nljJM|rY_{1\mu}|(S'_p L'_p J'_p) n'l'j'J'M'\rangle & \end{aligned} \tag{A.6}$$

Using the Wigner-Eckart thereom (equation (A.3)) to extract the dependence of the matrix on M and M'.

$$\begin{aligned} & \langle (S_p L_p J_p) nljJM|rY_{1\mu}|(S'_P L'_P J'_P) n'l'j'J'M'\rangle \\ = \; & \frac{C^{J'1J}_{M'\mu M}}{\sqrt{2J+1}} \langle (S_p L_p J_p) nljJ||rY_1||(S'_P L'_P J'_P) n'l'j'J'\rangle \end{aligned} \tag{A.7}$$

Multiply both sides by $\sum_{M'\mu} C^{J'1J'}_{M'\mu M}$ and use

$$\sum_{M'\mu} C^{J'1J}_{M'\mu M} C^{J'1J'}_{M'\mu M'} = \delta_{JJ'}\delta_{MM'} \tag{A.8}$$

to get

$$\begin{aligned} & \sum_{M'\mu} \langle (S_p L_p J_p) nljJM | rY_{1\mu} | (S'_p L'_p J'_p) n'l'j'J'M' \rangle C^{J'1J}_{M'\mu M} (2J+1)^{1/2} \\ = \; & \delta_{JJ'}\delta_{MM'} \langle (S_P L_P J_P) nljJ || rY_1 || (S'_P L'_P J'_P) n'l'j'J' \rangle \end{aligned} \tag{A.9}$$

Now sum both sides over M, note that the RHS in the above equation has no M dependence, and thus the sum over M introduces a factor $(2J+1)$ on the RHS.

$$\begin{aligned} & \langle (S_P L_P J_P) nljJ || rY_1 || (S'_P L'_P J'_P) n'l'j'J' \rangle \\ = \; & (2J+1)^{-1/2} \sum_{M'M\mu} C^{J'1J}_{M'\mu M} \langle (S_p L_p J_p) nljJM | rY_{1\mu} | (S'_p L'_p J'_p) n'l'j'J'M' \rangle \end{aligned} \tag{A.10}$$

Then use the Clebsch-Gordan coefficients (equation (A.1)) to reduce the matrix dependence to j, m, j' and m'.

$$\begin{aligned} LHS \; = \; & (2J+1)^{-1/2} \sum_{\substack{M'\mu \\ M_P m \\ M'_P m'}} C^{J'1J}_{M'\mu M} C^{J_p jJ}_{M_p m M} C^{J'_P j'J'}_{M'_P m'M'} \\ & \times \langle (S_p L_p J_p M_p) nljm | rY_{1\mu} | (S'_p L'_p J'_p M'_p) n'l'j'm' \rangle \end{aligned} \tag{A.11}$$

Since there is no change in the parent configuration this can be expressed as.

$$\begin{aligned} LHS \; = \; & (2J+1)^{-1/2} \delta(S_P L_P J_P M_P, S'_p L'_p J'_p M'_p) \sum_{\substack{M'\mu \\ M_P m \\ M'_P m'}} C^{J'1J}_{M'\mu M} C^{J_P jJ}_{M_p m M} C^{J_P j'J}_{M_p m'M'} \\ & \times \langle nljm | rY_{1\mu} | n'l'j'm' \rangle \\ = \; & (2J+1)^{-\frac{1}{2}} \delta(S_p L_p J_p, S'_p L'_p J'_p) \sum_{\substack{M'\mu \\ M_P m \\ m'}} C^{J'1J}_{M'\mu M} C^{J_p jJ}_{M_p m M} C^{J_p j'J'}_{M_p m'M'} \\ & \times < nl|r|n'l' >< ljm|Y_{1\mu}|l'j'm' > \end{aligned} \tag{A.12}$$

Then use equation (A.1) to uncouple j, m and j', m' into l, m_l, s, m_s and l', m'_l, s', m'_s.

$$\begin{aligned} LHS &= (2J+1)^{-\frac{1}{2}}\delta(S_pL_pJ_p, S'_pL'_pJ'_p) \sum_{\substack{M'\mu M_p \\ mm'm_l \\ m_sm'_lm'_s}} C^{J'1J}_{M'\mu M}C^{J_pjJ}_{M_pmM}C^{J_pj'J'}_{M_pm'M'}C^{l\frac{1}{2}j}_{m_lm_sm} \\ &\quad \times C^{l'\frac{1}{2}j'}_{m'_lm'_sm'} < nl|r|n'l' >< lm_lm_s|Y_{1\mu}|l'm'_lm'_s > \end{aligned} \tag{A.13}$$

m_s must equal m'_s so

$$\begin{aligned} LHS &= (2J+1)^{-\frac{1}{2}}\delta(S_pL_pJ_pm_s, S'_pL'_pJ'_pm'_s) \sum_{\substack{M'\mu M_p \\ mm'm_l \\ m_sm'_lm'_s}} C^{J'1J}_{M'\mu M}C^{J_pjJ}_{M_pmM}C^{J_pj'J'}_{M_pm'M'} \\ &\quad \times C^{l\frac{1}{2}j}_{m_lm_sm}C^{l'\frac{1}{2}j'}_{m'_lm'_sm'} < nl|r|n'l' >< lm_lm_s|Y_{1\mu}|l'm'_lm'_s > \end{aligned} \tag{A.14}$$

Using the Wigner-Eckart theorem once again we get

$$\begin{aligned} LHS &= (2J+1)^{-\frac{1}{2}}\delta(S_pL_pJ_p, S'_pL'_pJ'_p) \sum_{\substack{M'\mu M_p \\ mm'm_l \\ m_sm'_l}} C^{J'1J}_{M'\mu M}C^{J_pjJ}_{M_pmM}C^{J_pj'J'}_{M_pm'M'} \\ &\quad \times C^{l\frac{1}{2}j}_{m_lm_sm}C^{l'\frac{1}{2}j'}_{m'_lm_sm'}\frac{C^{l'1l}_{m'_l\mu m_l}}{(2l+1)^{\frac{1}{2}}} < nl|r|n'l' >< l||Y_1||l' > \\ &= \frac{(2J+1)^{-\frac{1}{2}}}{(2l+1)^{\frac{1}{2}}}\delta(S_pL_pJ_p, S'_pL'_pJ'_p) < nl|r|n'l' >< l||Y_1||l' > \\ &\quad \times \sum_{\substack{M'\mu M_p \\ mm'm_l \\ m_sm'_l}} C^{J'1J}_{M'\mu M}C^{J_pjJ}_{M_pmM}C^{J_pj'J'}_{M_pm'M'}C^{l\frac{1}{2}j}_{m_lm_sm}C^{l'\frac{1}{2}j'}_{m'_lm_sm'}C^{l'1l}_{m'_l\mu m_l} \end{aligned} \tag{A.15}$$

The Clebsch-Gordan coefficients are then represented graphically and equation (A.15) reduced to Wigner 6-j symbols as follows

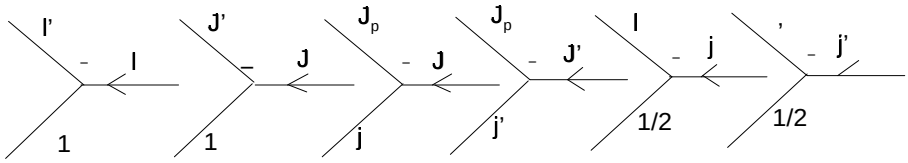

$(-1)^{2l'}(2l+1)^{1/2}$ $(-1)^{2J'}(2J+1)^{1/2}$ $(-1)^{2J_p}(2J+1)^{1/2}$ $(-1)^{2J_p}(2J'+1)^{1/2}$ $(-1)^{2l}(2j+1)^{1/2}$ $(-1)^{2l'}(2j'+1)^{1/2}$

=

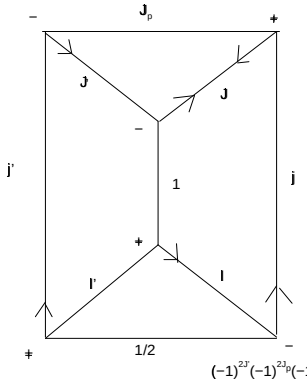

$(-1)^{2J'}(-1)^{2J_p}(-1)^{2J_p}(-1)^{2l}(-1)^{2l'}(-1)^{2l'}(2J+)^{1/2}(2J+1)^{1/2}(2J'+1)^{1/2}(2j+1)^{1/2}(2j'+1)^{1/2}(2l+1)^{1/2}$

=

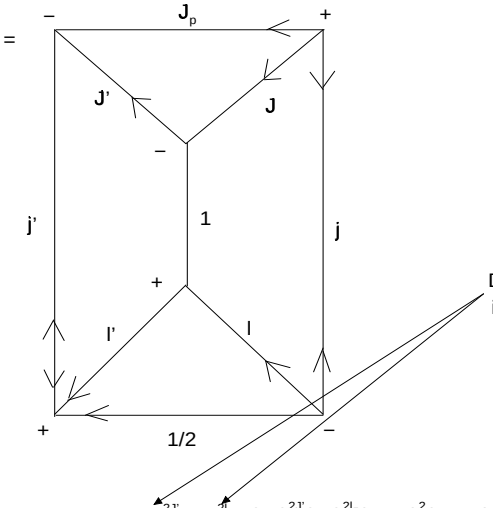

Due to reversal of arrow in diagram

$(-1)^{2J'}(-1)^{2l}$ $(-1)^{2J'}(-1)^{2l}[(2J+1)^2(2J'+1)(2j+1)(2j'+1)(2l+1)]^{1/2}$

=

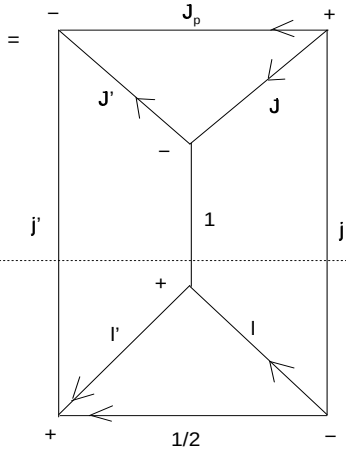

$[(2J+1)^2(2J'+1)(2l+1)(2j+1)(2j'+1)]^{1/2}$

Cut−off

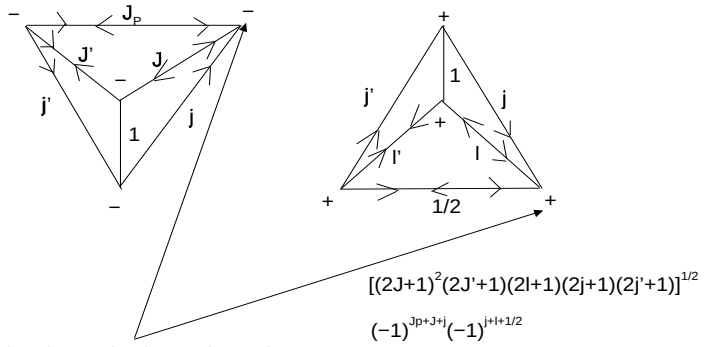

$[(2J+1)^2(2J'+1)(2l+1)(2j+1)(2j'+1)]^{1/2}$

$(-1)^{Jp+J+j}(-1)^{j+l+1/2}$

Note the change in sign at the node

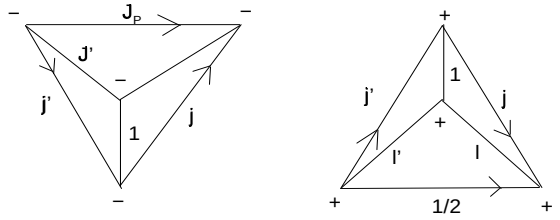

$(-1)^{Jp+J+j}(-1)^{j+l+1/2}$ $[(2J+1)^2(2J'+1)(2l+1)(2j+1)(2j'+1)]^{1/2}$

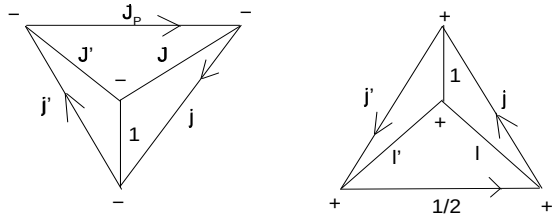

$(-1)^{2j'}(-1)^{2Jp}(-1)^{Jp+J+j}(-1)^{2j'}(-1)^{2j}(-1)^{j+l+1/2}$

$[(2J+1)^2(2J'+1)(2l+1)(2j+1)(2j'+1)]^{1/2}$

$$= \begin{Bmatrix} j & J & J_P \\ J' & j' & 1 \end{Bmatrix} \begin{Bmatrix} j' & l' & 1/2 \\ l & j & 1 \end{Bmatrix} (-1)^{2J_P}(-1)^{J_P+J}(-1)^{l+1/2}$$
$$\times[(2J+1)^2(2J'+1)(2j+1)(2j'+1)(2l+1)]^{1/2} \quad \text{(A.16)}$$

Thus we have

$$LHS = \frac{(2J+1)^{-1/2}}{(2l+1)^{1/2}}\delta(S_PL_PJ_P; S'_PL'_PJ'_P) < nl|r|n'l' > |^2| < l||Y_1||l' > |^2$$
$$\times(-1)^{3J_P+J+l+1/2} \begin{Bmatrix} j & J & J_P \\ J' & j' & 1 \end{Bmatrix} \begin{Bmatrix} j' & l' & 1/2 \\ l & j & 1 \end{Bmatrix}$$
$$\times[(2J+1)^2(2J'+1)(2j+1)(2j'+1)(2l+1)]^{1/2} \quad \text{(A.17)}$$

leading to the final result

$$|\langle (S_PL_PJ_P)nljJ||rY_1||(S'_PL'_PJ'_P)n'l'j'J'\rangle|^2$$
$$= (2J+1)(2j+1)(2j'+1)(2J'+1)\delta(S_PL_PJ_P; S'_PL'_PJ'_P)$$
$$\times| < nl|r|n'l' > |^2| < l||Y_1||l' > |^2 \begin{Bmatrix} j & J & J_P \\ J' & j' & 1 \end{Bmatrix}^2 \begin{Bmatrix} j' & l' & 1/2 \\ l & j & 1 \end{Bmatrix}^2 \quad \text{(A.18)}$$

It is now possible to sum equation A.18 to account for all possible degrees of resolution in the transitions for the new coupling scheme. The results are shown in table A.1.

	$(S_P L_P J_P)n'l'j'J'$	$(S_P L_P J_P)n'l'j'$	$(S_P L_P J_P)n'l'$	$(S_P L_P J_P)n'$
$(S_p L_p J_p)nljJ$	$(2J+1)(2J'+1)(2j+1)(2j'+1)$ $\left\{ \begin{array}{ccc} j & J & J_P \\ J' & j' & 1 \end{array} \right\}^2$ $\left\{ \begin{array}{ccc} j' & l' & 1/2 \\ l & j & 1 \end{array} \right\}^2$ $\mid < l \mid\mid Y_1 \mid\mid l' > \mid^2 \mid < nl \mid r \mid n'l' > \mid^2$	$(2J+1)(2j'+1)$ $\left\{ \begin{array}{ccc} j' & l' & 1/2 \\ l & j & 1 \end{array} \right\}^2$ $\mid < l \mid\mid Y_1 \mid\mid l' > \mid^2 \mid < nl \mid r \mid n'l' > \mid^2$	$\frac{(2J+1)}{(2l+1)}$ $\mid < l \mid\mid Y_1 \mid\mid l' > \mid^2 \mid < nl \mid r \mid n'l' > \mid^2$	$\frac{(2J+1)}{(2l+1)}$ $\sum_{l'} \mid < l \mid\mid Y_1 \mid\mid l' > \mid^2 \mid < nl \mid r \mid n'l' > \mid^2$
$(S_p L_p J_p)nlj$	$(2J'+1)(2j+1)$ $\left\{ \begin{array}{ccc} j' & l' & 1/2 \\ l & j & 1 \end{array} \right\}^2$ $\mid < l \mid\mid Y_1 \mid\mid l' > \mid^2 \mid < nl \mid r \mid n'l' > \mid^2$	$(2j'+1)(2J_P+1)(2j+1)$ $\left\{ \begin{array}{ccc} j' & l' & 1/2 \\ l & j & 1 \end{array} \right\}^2$ $\mid < l \mid\mid Y_1 \mid\mid l' > \mid^2 \mid < nl \mid r \mid n'l' > \mid^2$	$\frac{(2J_P+1)(2j+1)}{(2l+1)}$ $\mid < l \mid\mid Y_1 \mid\mid l' > \mid^2 \mid < nl \mid r \mid n'l' > \mid^2$	$\frac{(2J_P+1)(2j+1)}{(2l+1)}$ $\sum_{l'} \mid < l \mid\mid Y_1 \mid\mid l' > \mid^2 \mid < nl \mid r \mid n'l' > \mid^2$
$(S_p L_p J_p)nl$	$\frac{(2J'+1)}{(2l'+1)}$ $\mid < l \mid\mid Y_1 \mid\mid l' > \mid^2 \mid < nl \mid r \mid n'l' > \mid^2$	$\frac{(2j'+1)(2J_P+1)}{(2l'+1)}$ $\mid < l \mid\mid Y_1 \mid\mid l' > \mid^2 \mid < nl \mid r \mid n'l' > \mid^2$	$2(2J_P+1)$ $\mid < l \mid\mid Y_1 \mid\mid l' > \mid^2 \mid < nl \mid r \mid n'l' > \mid^2$	$2(2J_P+1)$ $\sum_{l'} \mid < l \mid\mid Y_1 \mid\mid l' > \mid^2 \mid < nl \mid r \mid n'l' > \mid^2$
$(S_p L_p J_p)n$	$\frac{(2J'+1)}{(2l'+1)}$ $\sum_l \mid < l \mid\mid Y_1 \mid\mid l' > \mid^2 \mid < nl \mid r \mid n'l' > \mid^2$	$\frac{(2j'+1)(2J_P+1)}{(2l'+1)}$ $\sum_l \mid < l \mid\mid Y_1 \mid\mid l' > \mid^2 \mid < nl \mid r \mid n'l' > \mid^2$	$(2J_P+1)$ $\sum_l \mid < l \mid\mid Y_1 \mid\mid l' > \mid^2 \mid < nl \mid r \mid n'l' > \mid^2$	$(2J_P+1)$ $\sum_{ll'} \mid < l \mid\mid Y_1 \mid\mid l' > \mid^2 \mid < nl \mid r \mid n'l' > \mid^2$

Table A.1: $(j-j)$ coupling to $(j'-j')$ coupling Q and R values evaluated for various levels of resolution.

A.2.2 Gaunt factors for cross-coupling

The angular algebra solution for the cross-coupling Gaunt factor proceeds as follow:

$$
\begin{aligned}
& < (S_P L_P) n l S L J || r Y_1 || (S'_P L'_P J'_P) n' l' j' J' > \\
= \; & (2J+1)^{1/2} \sum_{M'\mu} C^{J'1J}_{M'\mu M} < (S_P L_P) n l S L J M | r Y_{1\mu} | (S'_P L'_P J'_P) n' l' j' J' M' > \\
= \; & (2J+1)^{-1/2} \sum_{\substack{M'\mu M \\ M_S M_L M'_P \\ m'}} C^{J'1J}_{M'\mu M} C^{SLJ}_{M_S M_L M} C^{J'_P j' J'}_{M'_P m' M'} \\
& \times < (S_P L_P) n l S L M_L M_S | r Y_{1\mu} | (S'_P L'_P J'_P M'_P) n' l' j' m' >
\end{aligned}
$$

Note that in this last line the LHS is indepentent of M and therefore summing both sides over M introduces a $\frac{1}{(2J+1)}$ on the RHS, hence the change in sign of the $(2J+1)$ term.

$$
\begin{aligned}
LHS \; = \; & (2J+1)^{-1/2} \sum_{\substack{M'\mu M_S \\ M_L \\ M'_P m' \\ M_{S_P} m_s M_{L_P} \\ m_l m'_l m'_s \\ M'_{L_P} M'_{S_P}}} C^{J'1J}_{M'\mu M} C^{SLJ}_{M_S M_L M} C^{J'_P j' J'}_{M'_P m' M'} C^{S_P \frac{1}{2} S}_{M_{S_P} m_s M_S} C^{L_P l L}_{M_{L_P} m_l M_L} C^{l' \frac{1}{2} j'}_{m'_l m'_s m'} \\
& \times C^{L'_P S'_P J'_P}_{M_{L'_P} M_{S'_P} M_{P'}} < (S_P L_P M_{L_P} M_{S_P}) n l m_l m_s | r Y_{1\mu} | (S'_P L'_P M_{L'_P} M_{S'_P}) n' l' m'_l m'_s > \\
= \; & (2J+1)^{-1/2} \delta(S_p L_p M_{L_P} M_{S_P} m_s; S'_p L'_p M'_{L_P} M'_{S_P} m'_s) < n l m_l | r Y_{1\mu} | n' l' m'_s > \\
& \times \sum_{\substack{M'\mu M_S \\ M_L M'_P m' \\ M_{S_P} m_s M_{L_P} \\ m_l m'_l m'_s \\ M'_{L_P} M'_{S_P}}} C^{J'1J}_{M'\mu M} C^{SLJ}_{M_S M_L M} C^{J'_P j' J'}_{M'_P m' M'} \\
& \times C^{S_P \frac{1}{2} S}_{M_{S_P} m_s M_S} C^{L_P l L}_{M_{L_P} m_l M_L} C^{l' \frac{1}{2} j'}_{m'_l m'_s m'} C^{L'_P S'_P J'_P}_{M_{L'_P} M_{S'_P} M_{P'}}
\end{aligned}
$$

$$= \frac{(2J+1)^{-1/2}}{(2l+1)^{1/2}} \sum_{\substack{M'\mu M_S \\ M_L M'_P m' \\ M'_{S_P} m_s M_{L_P} \\ m_l m'_l}} C^{J'1J}_{M'\mu M} C^{SLJ}_{M_S M_L M} C^{J'_P j' J'}_{M'_P m' M'}$$

$$\times C^{S_P \frac{1}{2} S}_{M_{S_P} m_s M_S} C^{L_P l L}_{M_{L_P} m_l M_L} C^{l' \frac{1}{2} j'}_{m'_l m_s m'} C^{L_P S_P J'_P}_{M_{L_P} M_{S_P} M_{P'}} C^{l'1l}_{M_{l'} \mu M_l}$$

$$\times < nl|r|n'l' >< l||Y_1||l' > \tag{A.19}$$

One can then use the graphical methods as before to simplify the Clebsch-Gordan coefficients.

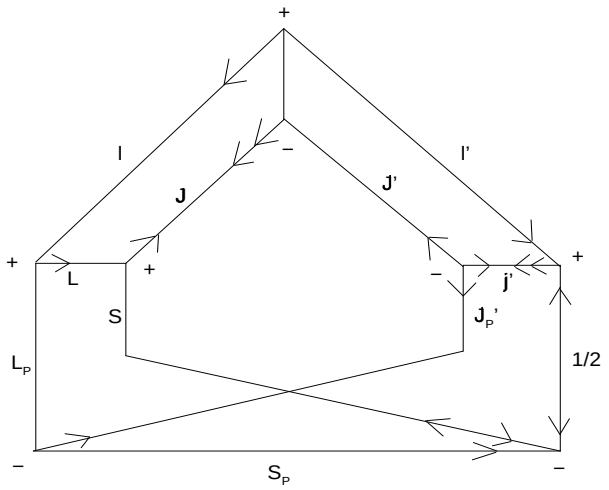

$$(2J+1)^{-1/2}(2l+1)^{1/2}(-1)^{2J'}(2J+1)^{1/2}(-1)^{2S}(2J+1)^{1/2}(-1)^{2Jp'}(2J'+1)^{1/2}$$

$$(-1)^{2Sp}(2S+1)^{1/2}(-1)^{2Lp}(2L+1)^{1/2}(-1)^{2l'}(2j'+1)^{1/2}(-2)^{2Lp}(2J_p'+1)^{1/2}(-1)^{2l'}(2l+1)^{1/2}$$

=

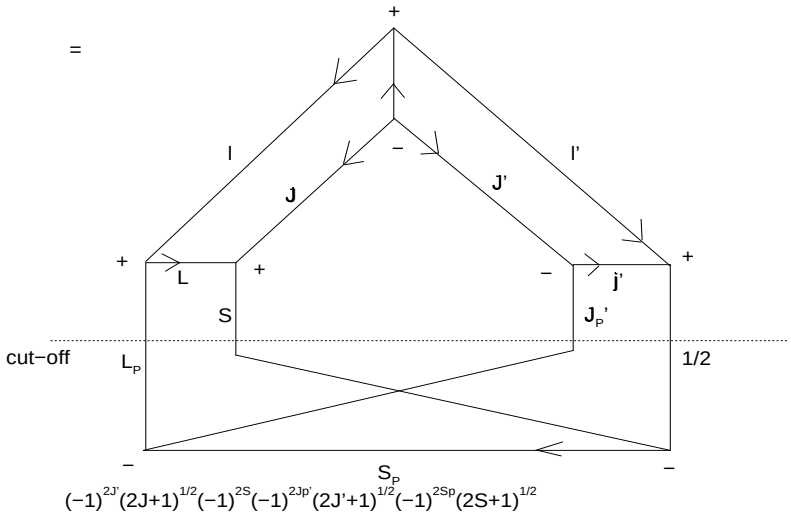

$$(-1)^{2J'}(2J+1)^{1/2}(-1)^{2S}(-1)^{2Jp'}(2J'+1)^{1/2}(-1)^{2Sp}(2S+1)^{1/2}$$

$$(2L+1)^{1/2}(2j'+1)^{1/2}(2J_p'+1)^{1/2}(-1)^{2J'}(-1)^{2Sp}$$

=

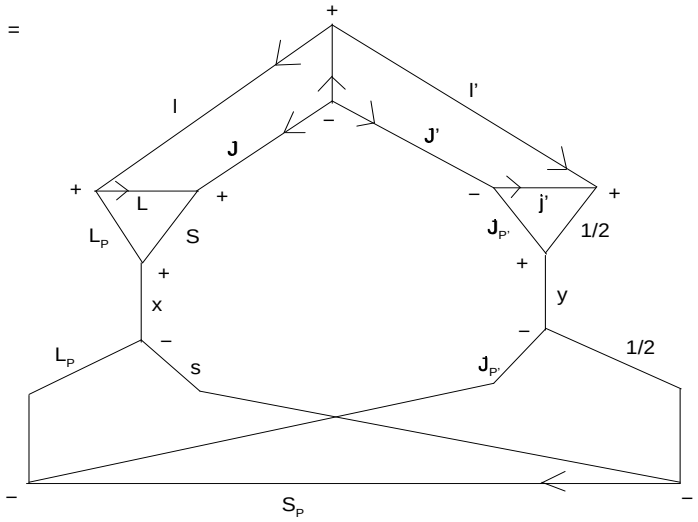

$$\Sigma(2x+1)(2y+1)$$

$$(-1)^{2S}(-1)^{2Jp'}(2J+1)^{1/2}(2J'+1)^{1/2}(2S+1)^{1/2}(2L+1)^{1/2}(2j'+1)^{1/2}(2J_{P'}+1)^{1/2}$$

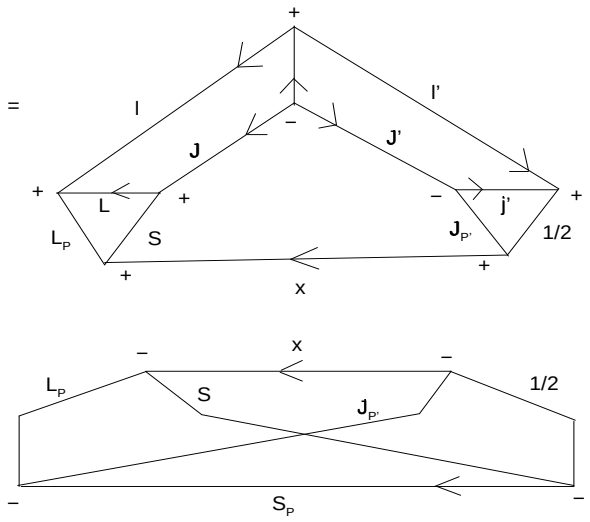

$$\Sigma(2x+1)\quad (-1)^{2S}(-1)^{2Jp'}[(2J+1)(2J'+1)(2S+1)(2L+1)(2j'+1)(2J_{P'}+1)]^{1/2}$$

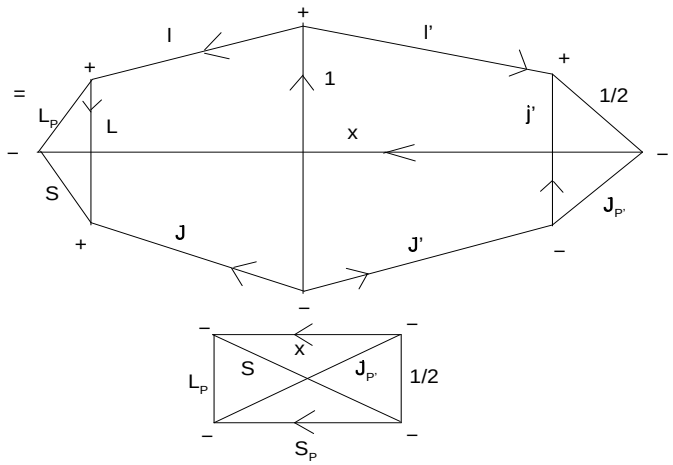

$$\Sigma(2x+1)(-1)^{2S}(-1)^{2Jp'}[(2J+1)(2J'+1)(2S+1)(2L+1)(2j'+1)(2J_{P'}+1)]^{1/2}$$

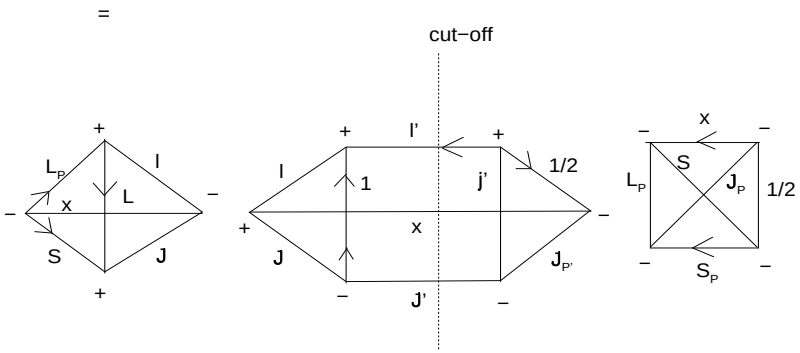

$$\Sigma(2x+1)\quad (-1)^{2S}(-1)^{2Jp'}[(2J+1)(2J'+1)(2S+1)(2L+1)(2j'+1)(2J'_P+1)]^{1/2}$$

≡Σ(2x+1)

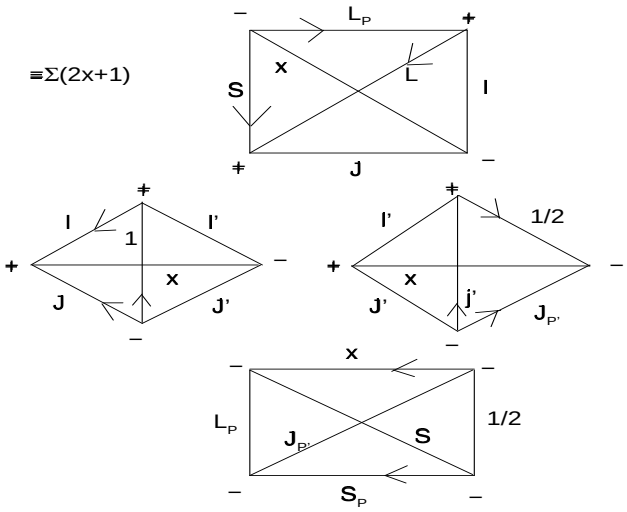

$(-1)^{2S}(-1)^{2Jp'}[(2J+1)(2J'+1)(2S+1)(2L+1)(2j'+1)(2J_{P'}+1)]^{1/2}$

≡Σ(2x+1)

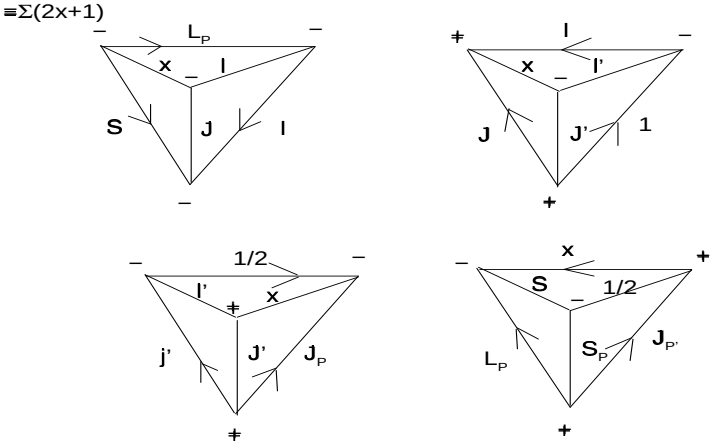

$(-1)^{2S}(-1)^{2Jp'}[(2J+1)(2J'+1)(2S+1)(2L+1)(2j'+1)(2J_{p'}+1)]^{1/2}$

≡Σ(2x+1)

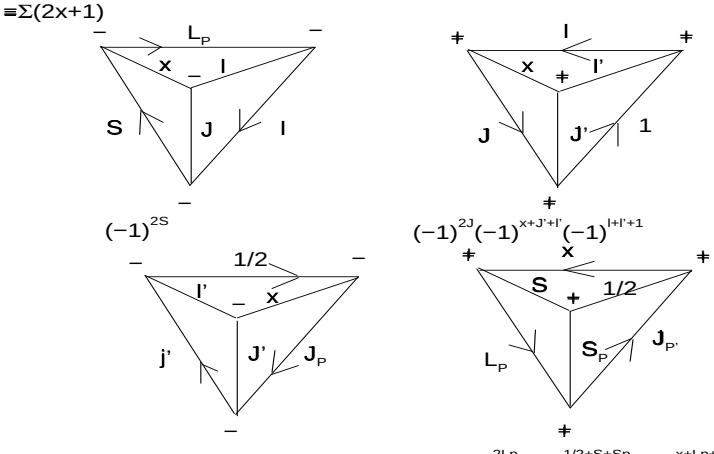

$(-1)^{2S}$

$(-1)^{2J}(-1)^{x+J'+l'}(-1)^{l+l'+1}$

$(-1)^{2Jp'}(-1)^{l'+J'+x}(-1)^{j'+J'+Jp'}$

$(-1)^{2Lp}(-1)^{1/2+S+Sp}(-1)^{x+Lp+S}$

$(-1)^{2S}(-1)^{2Jp'}[(2J+1)(2J'+1)(2S+1)(2L+1)(2j'+1)(2J_{p'}+1)]^{1/2}$

$$
\begin{aligned}
= \quad & \Sigma(2x+1) \left\{ \begin{array}{ccc} L & l & L_P \\ x & S & J \end{array} \right\} \left\{ \begin{array}{ccc} 1 & l' & l \\ x & J & J' \end{array} \right\} \left\{ \begin{array}{ccc} J'_P & x & 1/2 \\ l' & j' & J' \end{array} \right\} \left\{ \begin{array}{ccc} J'_P & 1/2 & x \\ S & L_P & S_P \end{array} \right\} \\
& \times (-1)^{2J} (-1)^{3x} (-1)^{3J'} (-1)^{3l'} (-1)^{l} (-1)^{\frac{3}{2}} (-1)^{j'} (-1)^{J'_P} (-1)^{3L_P} (-1)^{2S} (-1)^{S_P} \\
& \times [(2J+1)(2J'+1)(2S+1)(2L+1)(2j'+1)(2J_{P'}+1)]^{\frac{1}{2}}
\end{aligned}
$$

$$
\begin{aligned}
= \quad & (-1)^{2J+3J'+3l'+l+3/2+j'+J'_P+3L_P+2S+S_P} \\
& \times (2J+1)^{1/2} (2J'+1)^{1/2} (2S+1)^{1/2} (2L+1)^{1/2} (2j'+1) (2J'_P+1)^{1/2} \\
& \times \Sigma_x (2x+1) (-1)^{3x} \left\{ \begin{array}{ccc} L & l & L_P \\ x & S & J \end{array} \right\} \left\{ \begin{array}{ccc} 1 & l' & l \\ x & J & J' \end{array} \right\} \\
& \times \left\{ \begin{array}{ccc} J'_P & x & 1/2 \\ l' & j' & J' \end{array} \right\} \left\{ \begin{array}{ccc} J'_P & 1/2 & x \\ S & L_P & S_P \end{array} \right\}
\end{aligned} \tag{A.20}
$$

The results for the various levels of resolution can then be evaluated as before.

Bibliography

1. Alder, K., Huus, T., Mottleson, B., Winter, A.,1956, Reviews of Modern Physics **28** : 432.

2. Allen, C.W., 1991, 'Astrophysical quantities', Athlone

3. N. R. Badnell, 1986, Journal of Physics B, **19** : 3827

4. Bates, D.R., Kingston, A.E., McWhirter, R.W.P., 1962, Proc. Royal Soc. London, **267** : 297

5. Bates, D. R. (ed.), 1964, 'Atomic and molecular processes', Academic Press

6. Behringer, K., 1997, 'The Influence of Opacity on Hydrogen Line Emission and Ionisation Balance in High Density Divertor Plasmas', Max-Planck-Institute for Plasma Physics Report, IPP 10/5

7. Behringer, K., 1998, 'Escape Factors for Line Emission and Population Calculations', IPP-Report, Max Planck Institut fur Plasmaphysik, **90** : 439

8. Bergeron, P., Wesemael, F., Fontaine, G., 1991., Astrophysical Journal, **367** : 253

9. Bethe, H.A. & Salpeter, E.E., 1977, 'Quantum Mechanics of One- and Two-Electron Atoms', Plenum Pub. Co., New York

10. Bhatia, A. K. & Kastner, S. O., 1992, Astrophysical Journal Supplement Series, **79** : 139

11. Breger, P., 1998, Private Communication

12. Brink, D.M.S. & Satchler, G.R., 1968, 'Angular momentum', Oxford University Press

13. Brooks, D.H. et al., 1999, Astronomy and Astrophysics, **347** : 277

14. Brooks, D.H. et al., 2000, Astronomy and Astrophysics, **357** : 697

15. Burgess, A. & Summers, H.P., 1976, Mon. Not. R. Astr. Soc., **174** : 345

16. Burgess, A. & Summers, H.P., 1987, Mon. Not. R. Astr. Soc., **226** : 257

17. Carlsson, M., 1986, 'A Computer Program for Solving Multi-level Non-LTE Radiative Transfer Problems in Moving or Static Atmospheres', Uppsala Report N^o33, Uppsala Astronomical Observatory

18. Condon, E.U. & Shortley, G.H., 1935, 'The theory of atomic spectra', Cambridge University Press

19. Cowan, R.D., 1981, 'The theory of atomic structure and spectra', University of California Press, Berkley

20. Dappen, W., Anderson, L., Mihalas, D., 1987, Astrophysical Journal, **319** : 195

21. Drake, G.W.F. & Dalgarno, A., 1969, Astrophysical Journal, **157** : 459

22. Drawin, H.W., 1970, J. Quant. Spectrosc. Radiat. Transfer, **10** : 33

23. Doyle J.G. & McWhirter, R.W.P. 1980, Mon. Not. R. Astr. Soc., **193** : 947

24. Edmonds, A. R., 1975, 'Angular momentum in quantum mechanics', Princeton University Press

25. Eissner, W., Jones, M., Nussbaumer, H., 1974, Computer Physics Communications paper CPC8, 270

26. Fenstermacher, M. E. et al., 1999, Plasma Phys. Control. Fusion, 1999, **41** : A345

27. Fischbacher, G.A., Loch S.D. & Summers H.P., 2000, Astronomy and Astrophysics, **357** : 767

28. Fischbacher, G.A., 2001, 'Diagnosis and modelling of optically thick structures in the lower solar atmosphere', PhD thesis, University of Strathclyde

29. Gouttebroze, P., Heinzel, P. & Vial J.-C., 1993, Astronomy and Astrophysics Sup. Ser., **99** : 513

30. Griem, H. R., 1960, Astrophysical Journal, **132** : 883

31. Griem, H. R., 1964, 'Plasma Spectroscopy', McGraw -Hill

32. Griem, H. R. , 1974, 'Spectral Line Broadening by Plasmas', Academic Press

33. Griem, H. R. , 1997, 'Principles of Plasma Spectroscopy', Cambridge University Press

34. Gurovich, V. T. & Engel'sht, V. S., 1977, Sov. Phys. JETP, **45** : 232

35. Heasley, J.N. & Mihalas, D., 1976, Astrophysical Journal, **205** : 273

36. Hirayama, T., 1963, Proceedings of the Astronomical Society of Japan, **15** : 122

37. Hirayama, T., 1985, Solar Physics, **100** : 415

38. Holtsmark, J., 1919, Ann. Phys. (Leipzig), **58** : 577

39. Hooper, C.F., 1966, Physical Review, **149** : 77

40. Hooper, C.F., 1968, Physical Review, **165** : 215

41. Horton, L., 2001, Private communication

42. Hubney, I., Hummer, D.G., Lanz, T., 1994, Astronomy and Astrophysics, **282** : 151

43. Hummer, D.G, & Mihalas, D., 1988, Astrophysical Journal, **331** : 794

44. Iglesias, C.A., Lebowitz, J. & McGowan, D., 1983, Phys. Rev. A, **28** : 1667

45. Inglis, D.R. & Teller, E., 1939, Astrophysical Journal, **90** : 439

46. Irons, F.E. , 1979, J. Quant. Spectrosc. Radiat. Transfer, **22** : 1

47. Jordan C., 1967, Solar Physics, **2**: 441

48. H. Jentschke, Spektroskopische Untersuchung eines luftahnlichen Plasmafreistrahls, Thesis, Institut fur Plasmaforschung, Universitat Stuttgart, 1995

49. Kastner, S. O.& Bhatia, A. K., 1992, Astrophysical Journal, **401** : 416

50. Kastner, S. O. & Bhatia, A. K., 1998, Mon. Not. R. Astr. Soc., **298** : 763

51. Kastner S.O., 1999, Physica Scripta, **60** : 381

52. Keenan R.P. & Kingston A.B., 1986, Mon. Not. R. Astr. Soc., **220** : 493

53. Krasheninnikov et al., 1997, Phys. Plasmas, **4** : 1638

54. Lachin, T., 1997, 'The investigation of opacity in the JET tokamak divertor region', PhD thesis, University College London

55. Lang J., Mason H.E. & McWhirter R.W.P., 1990, Solar Physics, **129** : 31

56. Levinson, C. & Ford, K.W., 1955, Phys. Rev., **99** : 792

57. Loch, S.D. & Summers, H.P., 1999, Proc. from the 8th SOHO workshop, Paris, p447

58. Lorentz H. A., Proc. R. Acad. Sci. (Amsterdam), **8** : 591

59. McCracken, G.M. et al., 1998, JET-P(98)21

60. Meigs, A. et al., 1998, JET-CP(98)28

61. Meigs, A., Fundamenski, W., Jupen, C, Larsen, A., Loch, S., O'Mullane, M., Summers, H. , 2000 , 27th EPS conference on controlled fusion and plasma physics, Budapest, 12-16th June 2000

62. Meigs, A., 2001, Private communication

63. Menzel, D.H., 1937, Astrophysical Journal, **85** : 330

64. Menzel, D.H. & Baker, J.G., 1937, Astrophysical Journal, **86** : 70

65. Menzel, D.H. & Pekeris, C.L., 1935, Mon. Not. R. Astr. Soc., **96** : 77

66. Mitchell, A.C.G. & Zemansky, M.W., 1961, 'Resonance Radiation and Excited Atoms',Cambridge University Press

67. Namba, S., Goto, M., Tsuboi, H., Oda, T. & Sato, K., 2000, Journal of applied physics, **88** : 3182

68. O'Mullane, M.G. & Summers, H.P., 1999, 'PFC doping with trace impurities - spectroscopic studies of sensitivities of survey instruments', UKAEA Fusion /EU Task No. DV7A-T438 Report

69. Ohno, N., Ezumi, N., Krasheninnikov, S.I., & Pigarov, A. Yu., 1998, Physical Review Letters, **81** : 818

70. Pengelly, R.M. & Seaton, M.J., 1964, Mon. Not. R. Astr. Soc., **127** : 165

71. Pigarov, A. Yu. et al., 1998, Plasmas Physics and Controlled Fusion , **40** : 2055

72. Poland, A. & Anzer, U., 1971, Solar physics, **19** : 401

73. Preist, E.R., 1989, 'Dynamics and structure of Quiescent Solar Prominences', Kluwer Acad. Publ., Dordrecht

74. Rose, M. E., 1957 ,'Elementary Theory of Angular Momentum', New York: Wiley London: Chapman and Hall

75. Scharmer, G.B., & Carlsson, M., 1985, J. Comput. Phys., **59** : 56

76. Schmieder, B., Heinzel, P., Kucera, T. & Vial, J.C., 1998, Solar Physics, **181** : 309

77. Schmieder, B., Heinzel, P., Vial, J.C. & Rudawy, P., 1999, Solar Physics, **189** : 109

78. Schmieder, B., Kucera, T.A., Heinzel, P., Vial, J.C., Poland, A., 1999b, Proc. from the 8th SOHO workshop, Paris, p605

79. Schmieder, B., Delanee, C., Yong, D. Y., Vial, J.C. & Madjarska, M., 2000, Astronomy and Astrophysics, **358** : 728

80. Seaton, M.J., 1990, J. Phys. B: At. Mol. Opt. Phys., **23** : 3255

81. Sobelman, I.I., Vainshtein, L.A. and Yukov, E.A., 1981, 'Excitation of Atoms and Broadening of Spectral Lines', Springer-Verlag

82. Spadaro, D. et al., 2000, Astronomy and Astrophysics, **359** : 716

83. Stamm, R. el al., 23-27th March 1998, Proceedings of the American Physical Society: Atomic Processes in Plasmas, Auburn ,USA

84. Stellmacher, G. & Wiehr, E., Astronomy and Astrophysics, **290** : 655

85. Summers, H.P., 1977, Mon. Not. R. Asrt. Soc., **178** : 101

86. Summers, H.P., 1994, JET Joint Undertaking internal report, JET-IR(94)06

87. Summers, H.P., 2001, The ADAS User Manual, version 2.2, http://adas.phys.strath.ac.uk/adas/.

88. Summers, H.P. & Hooper, M.B., 1983, Plasma Phys. Control. Fusion., **25** : 1311

89. Tandberg-Hanssen, E., 1995, 'The Nature of Solar Prominences', Kluwer Acad. Publ., Dordrecht

90. Talin, B. et al., 1995, Phys. Rev. A, **51** : 1918

91. Talin, B. et al., 1997, J. Quant. Spectrosc. Radiat. Transfer, **58** : 953

92. Vernazza, J.E., Avret, E.H., Loeser, R., 1981, Astrophysical Journal Supplement series, **45** : 635

93. Wan, A.S. et al., 1995, J. Nucl. Mater., **1102** : 220

94. Wenzel, U. et al. , 1999, Plasma Phys. Control. Fusion, **162** : 189

95. Whyte, D.G., Humphreys, D.A. & Taylor, P.L., 2000, Physics of plamsas, **7** : 4052

96. Wilhelm, K. et al. , 1995, Solar Physics, **41** : 801

97. Zarro, D.M. & Zirin, H., 1985, Astronomy and Astrophysics, **148** : 240

98. Zirker, J.B., 1988, Solar Physics, **119** : 341